Justus-Liebig-Universität Gießen
Fachbereich 07 - Mathematik und Informatik, Physik, Geographie

JUSTUS-LIEBIG-
UNIVERSITÄT
GIESSEN

Inaugural-Dissertation zur Erlangung des Doktorgrades der Naturwissenschaften

Developments for Multiple-Reflection Time-of-Flight Mass Spectrometers and their Application to High-Resolution Accurate Mass Measurements of Short-Lived Exotic Nuclei

vorgelegt von
Samuel Ayet San Andrés
aus Valencia, Spanien
28.05.2018

- Erstgutachter: Prof. Dr. Christoph Scheidenberger
- Zweitgutachter: Prof. Dr. Dr. h.c. Hans Geissel

Selbstständigkeitserklärung

Hiermit versichere ich, die vorgelegte Thesis selbstständig und ohne unerlaubte fremde Hilfe und nur mit den Hilfen angefertigt zu haben, die ich in der Thesis angegeben habe. Alle Textstellen, die wörtlich oder sinngemäß aus veröffentlichten Schriften entnommen sind, und alle Angaben die auf mündlichen Auskünften beruhen, sind als solche kenntlich gemacht. Bei den von mir durchgeführten und in der Thesis erwähnten Untersuchungen habe ich die Grundsätze guter wissenschaftlicher Praxis, wie sie in der ‚Satzung der Justus-Liebig-Universität zur Sicherung guter wissenschaftlicher Praxis' niedergelegt sind, eingehalten. Gemäß § 25 Abs. 6 der Allgemeinen Bestimmungen für modularisierte Studiengänge dulde ich eine Überprüfung der Thesis mittels Anti-Plagiatssoftware.

Datum Unterschrift

Contents

Zusammenfassung

Im Rahmen dieser Arbeit wurden Verbesserungen und Entwicklungen für Multireflexions Flugzeit-Massenspektrometer (MR-TOF-MS) entwickelt und für Massenmessungen von exotischen und kurzlebigen Kernen mit höchster und bisher unerreichter Genauigkeit benutzt. Die kinetische Energie der Ionen und die Wiederholungsrate des Spektrometers wurden erhöht. Eine Auflösung von mehr als 600000 in weniger als 20 ms Messzeit und Wiederholungsrate über 1000 Hz wurden erreicht. Darüber hinaus wurde die Zuverlässigkeit und Stabilität des Systems verbessert, was sich durch eine Reduktion des Temperaturkoeffizienten des Spektrometer auf 8 ppm/°C zeigt. Das System ist universell und kann Massen von Elementen unabhängig von ihren chemischen Eigenschaften messen, was durch die durchgeführte Messung von Edelgasen und sehr reaktiven Elementen am Beispiel von Uran gezeigt wurde. Außerdem wurde die Datenauswertemethode zur Bestimmung der Masse und ihrer Genauigkeit weiter verbessert.

In drei Experimenten an der GSI Helmholtzzentrum für Schwerionenforschung GmbH in Deutschland wurden in den Jahren 2014 und 2016 Massen von themalisierten Spaltfragmenten von ^{238}U sowie themalisierten Projektilfragmenten von ^{238}U und ^{124}Xe erzeugt und getrennt im Fragment Separator (FRS), mit dem MR-TOF-MS des FRS-Ion Catcher mit Auflösungen bis 450000 gemessen. Mit der verbesserten Datenauswertemethode wurden Isotope von acht verschiedenen Elementen mit Halbwertszeiten von weniger als 300 ms gemessen, insgesamt 25 Massen kurzlebiger Kerne, darunter sieben in isomeren Zuständen mit Anregungsenergien bis zu 280 keV. Die in dieser Arbeit mit den FRS-Ion Catcher erhaltenen Massen haben eine relative Genauigkeit von bis zu $1.1 \cdot 10^{-7}$, was einem absoluten Wert von 13 keV entspricht. Die niedrigste bisher mit den FRS-Ion Catcher erreichte relative Genauigkeit beträgt $6 \cdot 10^{-8}$. Die durchschnittliche Abweichung aller im FRS-Ion Catcher gemessenen Massen im vergleich mit Literaturwerten beträgt 4.3 ± 2.5 keV und zeigt keine systematische Abweichung. Die Breitbandfähigkeiten des Systems in Kombination mit einem hohen Auflösungsvermögen wurden für die Identifizierung von Uranionen und Molekülen in verschiedenen Ladungszuständen durch Massenmessungen verwendet. Der FRS-Ion Catcher ist damit voll funktionsfähig und bietet eine hervorragende Kombination von Leistungsmerkmalen für Messungen mit exotischen Kernen in unbekanntem Gebiet.

In einem Experiment am Canada's National Laboratory for Particle and Nuclear Physics (TRIUMF) in Kanada wurden im Jahr 2017 mit dem neu installierten MR-TOF-MS von TRIUMF′S Ion Trap for Atomic and Nuclear Science (TITAN), das an der Justus-Liebig Universität Gießen entwickelt, gebaut und in Betrieb genommen wurde, Massenmessungen von neutronenreichen Galliumisotopen von A = 80 bis A = 85 mit einer relativen Genauigkeit von bis zu $3.3 \cdot 10^{-7}$ durchgeführt. Die Elektronik wurde in gleicher Weise verbessert wie für das MR-TOF-MS beim FRS an der GSI. Die Massen von ^{84}Ga und ^{85}Ga mit Halbwertszeiten von 85 ms bzw. 92 ms wurden im Rahmen dieser Arbeit erstmals gemessen. Der Einfluss beider Massen auf die Nukleosynthese im schwacher r-Prozess wurde untersucht.

Abreviations

CSC	Cryogenic Stopping Cell
CPET	Cooling Penning Trap
DU	Diagnostic Unit
EBIT	Electron Beam Ion Trap
FAIR	Facility for Antriprotons and Ions Research
FRS	Fragment Separator
FRS-IC	Fragment Separator - Ion Catcher
FWHM	Full Width at Half Maximum
GSI	GSI Helmholtzzentrum für Schwerionenforschung GmbH
IMS	Isochronous Mass Spectromety
IP	Ionization Potential
ISAC	Isotope Separator And Accelerator
ISOL	Isotope Separation On-Line
LEB	Low Energy Branch
MPET	Measurement Penning Trap
MRP	Mass Resolving Power
MR-TOF-MS	Multiple-Reflection Time-of-Flight Mass Spectrometer
RFQ	Radio Frequency Quadrupole
RIB	Rare Isotope Beam
r-PROCESS	Rapid Neutron Capture Process
SMS	Schottky Mass Spectrometry
Super-FRS	Superconducting Fragment Separator
TOF	Time-of-Flight
TRIUMF	Canada's National Laboratory for Particle and Nuclear Physics
TITAN	TRIUMF'S Ion Trap for Atomic and Nuclear Science
UNILAC	Universal Linear Accelerator

Motivation and Goals

The Multiple-Reflection Time-of-Flight Mass-Spectrometry (MR-TOF-MS) is a relatively new mass measurement technique, which relies on extending the flight path of ions by trapping them between two electrostatic mirrors for a certain time [Wollnik and Przewloka, 1990]. It was introduced to the field of nuclear science with three main goals: **1)** perform high accuracy mass measurements of exotic nuclei with low production yields and short half-lives, obtaining key information for nuclear structure and nuclear astrophysics [Scheidenberger et al., 2001], **2)** purify radioactive beams, helping to suppress undesired isobar contaminants, delivering an isobarically clean beam to other experiments [Plaß et al., 2008] and **3)** to be used as a broadband mass spectrometer for diagnostic purposes. These challenges are accomplished by the unique combination of characteristics presented by the MR-TOF-MS, which are: broadband, fast and non-scanning measurements, high sensitivity and high resolving power. The motivation of this work is to improve the performance of the MR-TOF-MS technique to study the nuclear structure and nuclear astrophysics via high precision mass measurements of exotic nuclei, in particular in an accelerator environment and under online conditions, to establish the MR-TOF-MS as a standard and competitive mass measurement technique in the field of nuclear physics.

The main goal of this work is to perform mass measurements of exotic nuclei by enhancing and exploiting the strengths of the MR-TOF-MS. To achieve it, a three step approach is followed. **1)** Firstly is to evolve the technique from its current state to achieve a technically upgraded MR-TOF-MS by: increasing the kinetic energy of the ions (for higher resolving power) and the repetition rate (for higher rate capability and the measurement of very short-lived nuclei), increasing the stability and reliability (for high precision and stable long-term measurements with lowest rates) and obtaining a universal system where undesired chemical reactions and losses are minimized (improved cleanliness of the system). **2)** The second step, is to develop an improved data evaluation procedure able to analyze overlapping peaks from isobars or low-lying isomeric states, where special attention to the individual contributions to the total mass uncertainty is given. **3)** In the third step, these improvements have been implemented in two different MR-TOF-MS developed, built and commissioned at the Justus-Liebig University: one at GSI Helmholtzzentrum für Schwerionenforschung GmbH (GSI),

Germany and its sister device at Canada's National Laboratory for Particle and Nuclear Physics (TRIUMF), Canada, and Mass measurements of exotic nuclei have been performed with both systems.

1 Mass Measurements of Exotic Nuclei

1.1 Physics Motivation

The mass of the atom is an important information for various research areas, covering different applications and branches. The required relative uncertainty of the mass measurements for extracting different knowledge and conclusions, depends on the field of application. The relative uncertainty needed spans between $\sim 10^{-4}$ to $\sim 10^{-11}$. Different research areas with the needed relative mass uncertainty for some applications or research branches is shown in Tab. 1.1.

Research Area	**Application**	**Relative Uncertainty (δm/m)**	**Absolute Uncertainty at 100u (δm)**
Chemistry	Ion / Molecule ID	10^{-4} - 10^{-9}	10 MeV/c^2 to 100 eV/c^2
Nuclear Physics	Structure and Models	10^{-6} - 10^{-7}	100 keV/c^2 to 10 keV/c^2
Astrophysics	Nucleosynthesis	10^{-6} - 10^{-7}	100 keV/c^2 to 10 keV/c^2
Metrology	Fundamental Constants	$< 10^{-9}$	$<$ 100 eV/c^2
Atomic Physics	Atomic Binding Energy	$< 10^{-10}$	$<$ 10 eV/c^2
Particle Physics	CPT Invariance Test	$< 10^{-11}$	$<$ 1 eV/c^2

Table 1.1: Relative mass uncertainty needed for different research areas, including the example of absolute uncertainty for a mass of 100 u. Data based on [Blaum, 2006, Atasanov, 2016].

For nuclear physics and nuclear astrophysics a relative uncertainty as low as 10^{-7} is desired, which is achieved by the improved spectrometer presented in this work.

1.1.1 Nuclear Physics

Nuclear mass measurements are of high interest in nuclear physics due to the main information that is carried within, the binding energy of the nucleus. The mass of an atom can be described as Eq. 1.1. Note that the last term corresponds to the binding energy of the electrons to the nuclei (Atomic Physics). As can be seen in Tab. 1.1, the effect of this term can be neglected in mass measurements of low charge-state

ions when a relative uncertainty level suitable for nuclear physics or astrophysics is desired.

$$m(A,Z) = Z \cdot m_p + (A-Z) \cdot m_n - \frac{BE_{NUCLEONS}}{c^2} + Z \cdot m_e - \frac{BE_{ELECTRONS}}{c^2} \quad (1.1)$$

Where Z is the atomic number, A is the mass number, m_p is the mass of the proton, m_n is the mass of the neutron, m_e is the mass of the electron, $BE_{NUCLEONS}$ is the binding energy of the nucleons and $BE_{ELECTRONS}$ is the binding energy of the electrons. The binding energy of the nucleus is a direct footprint of all effects and interactions on the nuclear level. Therefore, systematic mass measurement of different combination of bound protons and neutrons can reveal information about the evolution of the nuclear structure, adding the understanding of the elemental forces acting in the nuclei.

The early measurements of nuclear masses started by Aston [Aston, 1920, Aston, 1927], led to the first semi-empirical model of the nucleus, with the aim of modeling and describing the interactions between bound nucleons through the binding energy, the Liquid Drop Model [Weizsäcker, 1935]. When the landscape of binding energies for different combinations of bound protons and neutrons got richer in quantity and in quality, thanks to the developments of new mass measurement techniques, deviations from the Liquid Drop Model were observed in the measured binding energies, emphasized specially in some given numbers of protons and neutrons. That was the hint needed by the theoretical physicists developing the mass models to consider the shell structure of the nucleus, where with a closed shell, special properties arise, as for example sudden increase in binding energy or longer half-life. The study of the nuclear structure far from stability is a current endeavour. Structures that are not existing close to stability appear in exotic nuclei, such as halos and skins, and structures present close to stability fade out towards exotic nuclei.

1.1.2 Nuclear Astrophysics

The nuclear masses are also of interest when trying to find out the nature or evolution of the astronomical objects. The particular question of how stars are powered was tried to be answered by many physicists. After Aston discovered with his experiments that some mass was missing when forming a helium atom out of 4 hydrogen atoms, meaning that the mass of the nucleons is heavier separated compared to when they are bound forming the nuclei, led Eddington to think that this transmutation reaction would convert the missing mass into energy to power the stars [Eddington, 1920].

Other questions are still open and represent a challenge to physicists due to the vast amount of information needed to address them, like, how and under which conditions nature is able to synthesize the elements heavier than iron. This nucleosynthesis mechanism involves thousands of nuclei and will define the abundances of the elements found in our universe. For the solar system, the relative abundance of the elements can be seen in Fig. 1.1.

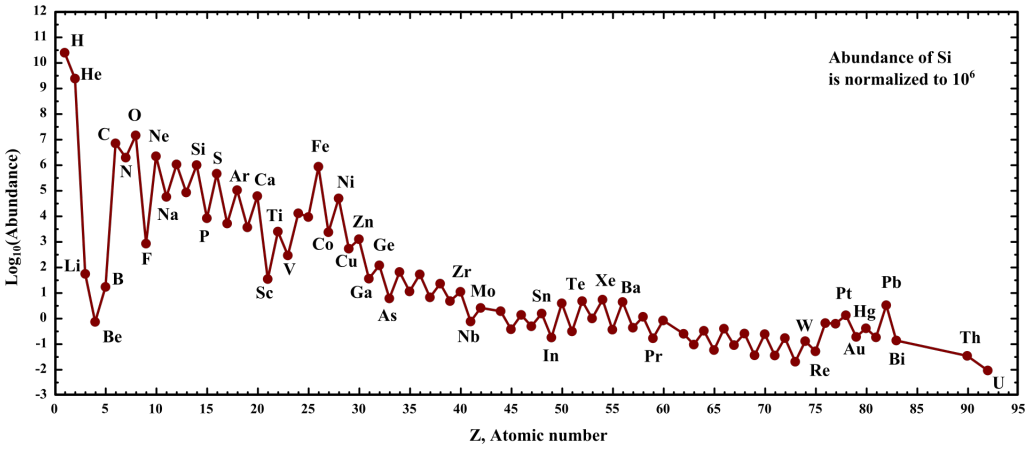

Figure 1.1: Relative abundance of the elements in the solar system versus the atomic number. The abundances are normalized with a silicon abundance of 10^6. The different peaks observed in the abundances (for example $Z \approx 54$, $Z \approx 78$ or $Z \approx 82$) are a sign of the different stellar nucleosynthesis processes and the intrinsic nuclear properties. Data extracted from [Lodders, 2003].

The element abundances contain signs of the different mechanisms that nature used to synthesize the heavy elements. Three main processes are thought to produce the elements heavier than iron: the p-process (proton-capture), s-process (slow neutron-capture) and r-process (rapid neutron-capture), which give their characteristic footprint, such as the peak abundance around Z = 54 or Z = 78 for the r-process or the high abundance of lead for the s-process [Burbidge et al., 1957]. From the three processes, the last two are thought to synthesize almost all (about half and half) the elements heavier than iron, letting to the p-process the responsibility of some less abundant stable nuclides heavier than iron (called p-nuclei). Each process, will occur in different astrophysical conditions and will run over the nuclide chart through different paths as depicted in Fig. 1.2.

Where the synthesis path runs in the different stellar nucleosyntheses processes, will be governed by first, the astrophysical environment, defined by neutron flux, proton flux, temperatures, etc. and second, the intrinsic characteristics of the nuclei, such as mass, decay half-life, capture cross section, fission barrier, etc. In the r-process, the sudden drop of the neutron separation energy in closed neutron shells leds to the accumulation of matter in these isotones. After the freezout and decay phase, gov-

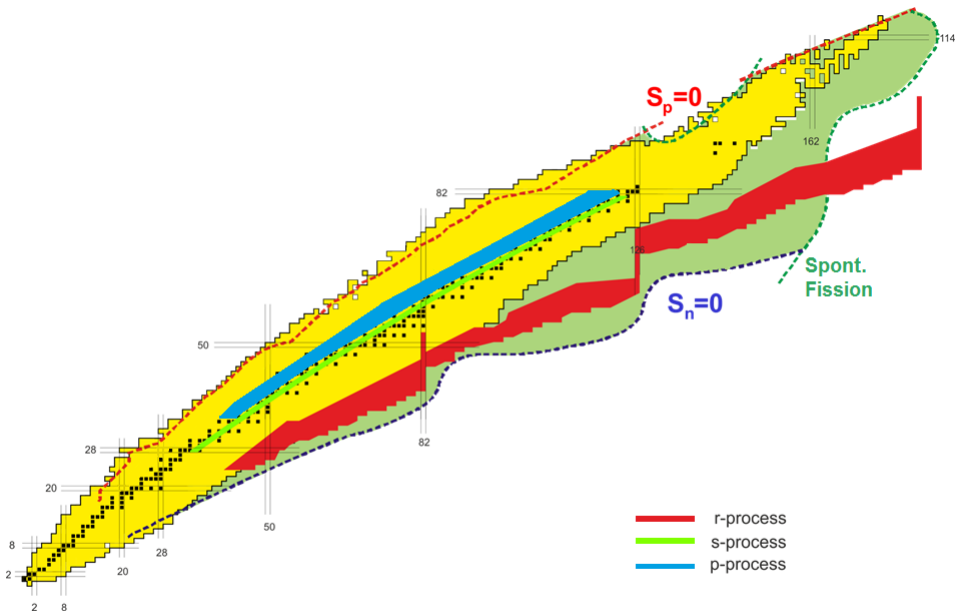

Figure 1.2: Nuclear chart with the main nucleosynthesis processes [Stock, 2013]. In yellow nuclei with known mass and in green nuclei with extrapolated mass are shown. In dashed red line, the limit nuclei with zero proton separation energy, in dashed dark-blue line, the limit nuclei with zero neutron separation energy and in dashed green line the limit nuclei with spontaneous fission are marked.

erned by β-delayed neutron emission probabilities, the accumulated matter will leave the characteristic sign of the r-process on the stable element abundances, remarkably at the peaks with A $\approx$ 130 and A $\approx$ 195, reflecting the accumulation of matter at the isotones with N = 82 and N = 126 respectively [Cameron, 1957]. The r-process runs along neutron-rich nuclei and has to rely often in mass models and half-lives predictions for the computation of the element abundances obtained after the nucleosynthesis process. The different properties, such as masses and half-lives, obtained by models and approximations for the neutron-rich nuclei have high uncertainties, and the more exotic, the higher the uncertainty. These uncertainties are the limiting factor for the predictive capabilities for calculations of element abundances, specially for the r-process due to the lack of information of neutron-rich nuclei of medium to heavy masses. Sensitivity studies of the r-process are performed by running several simulations where the nuclear properties of the nuclei, obtained by models or approximations (masses, lifetimes, capture rates, etc), are systematically changed, resulting in different element abundances. With these sensitivity studies, which property or properties of the different nuclei involved in the simulations will have a strong impact in the final element abundance for a given astrophysical condition can be distinguished, giving a hint and a motivation to the experimentalist about the priorities for future measurements [Aprahamian et al., 2014, Mumpower et al., 2016]. In Fig. 1.3, results of a sensitivity

study for nuclear mass is depicted [Aprahamian et al., 2014]. Here, the neutron-rich gallium isotopes measured for the first time in the context of this work are defined as high priority (green frame).

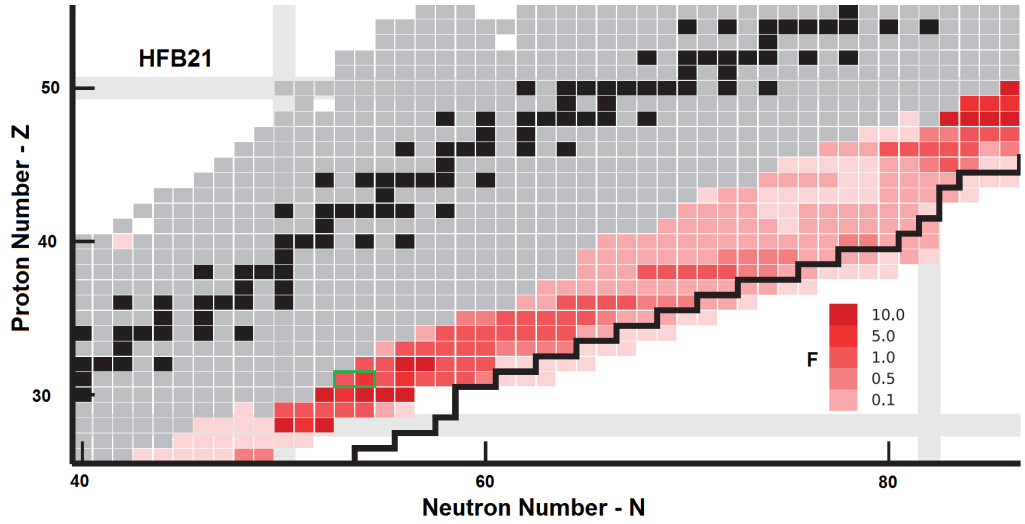

Figure 1.3: Results from the sensitivity studies of nuclear masses for the main r-process [Aprahamian et al., 2014]. In red, the sensitivity factor (F) calculated for the extrapolated masses obtained by the HFB-21 mass model. In a green box the nuclei ^{84}Ga and ^{85}Ga, whose mass was directly measured for the first time in the context of this thesis, are highlighted.

1.2 Production and Separation of Exotic Nuclei

Not only the stable nuclei found in nature are of interest, but also, due to the reasons mentioned in the previous points, exotic nuclei with proton and neutron combinations which are not found in nature due to their short half-life. For the mass measurement of an exotic nucleus, the first goal to be achieved is its production. These nuclei are produced by means of different nuclear reactions, mainly: spallation, fragmentation and fission. The main techniques of production and separation of exotic nuclei will be reviewed in the following.

1.2.1 Isotope Separator On-Line

The Isotope Separator On-Line (ISOL) method produces exotic nuclei mainly by the spallation of a target by energetic protons. The block diagram of the different stages of the ISOL production method can be seen in Fig. 1.4.

The energetic beam of protons (hundreds of MeV up to the GeV range) impinges on the target, composed of several thin foils with a total areal density of several tens of g/cm^2.

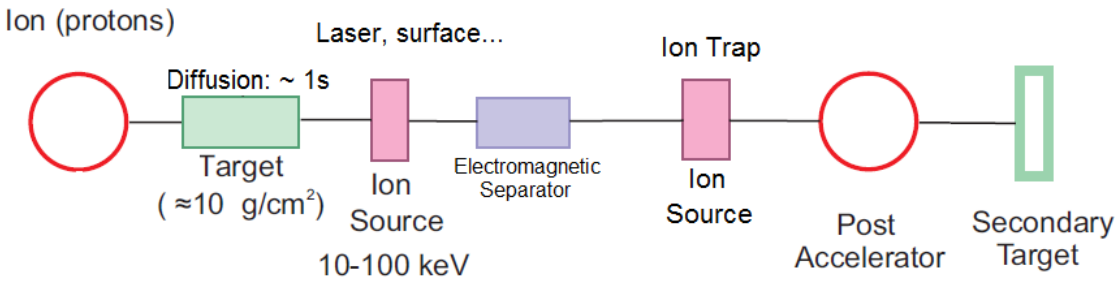

Figure 1.4: ISOL-type production facility block diagram [Geissel et al., 2014, Geissel et al., 1995]. Red: accelerator infrastructure, green: targets, violet: electromagnetic separator and pink: ion sources and traps for experiments.

This causes spallation of the target nuclei, usually composed of heavy stable elements such as uranium, tantalum, etc. generating elements lighter than the target, which are then released at low energies by the diffusion and effusion mechanisms. After the generation of the fragments and the effusion out of the target, the ions are selectively ionized by means of laser ionization, surface ionization or other techniques and are accelerated to energies of about 10 - 100 keV/q, with q the charge state. This energy is used to separate them in a low energy electromagnetic separator. After this mass separator, the ions can be used by the experiments (for example mass measurement) or get accelerated over the Coulomb barrier to perform reactions in a secondary target. The isobaric contamination can not be suppressed by the mass separator and techniques such as resonant laser ionization have to be used to enhance the rate of certain element. Other limitations of the method are: long times between production of the exotic nuclei and extraction from the target, limiting nuclei with minimum half-life to be observed. Also, the extraction efficiency from the target is element dependent due to chemistry reactions of the produced fragments. A strong point, is the possibility to generate very high rates of fragments for some elements. Also, in some cases, the low energy of the delivered beam can be seen as an advantage. In the results chapter, an introduction to the TITAN (TRIUMF's Ion Trap for Atomic and Nuclear Science) facility will be given, where mass measurements of exotic nuclei produced by ISOL method were performed.

1.2.2 In-Flight Separation

In the in-flight production mechanism, a high energetic beam of heavy elements penetrates through a thick target (few g/cm^2) undergoing nuclear reactions and producing exotic nuclei. The main nuclear reactions undergone in the target are projectile fission, produced via Coulomb-fission or abrasion-fission and projectile fragmentation. The

coulomb-fission reaction involves the electromagnetic excitation of the projectile via the exchange of virtual photons between the projectile and the target, see Fig. 1.5.

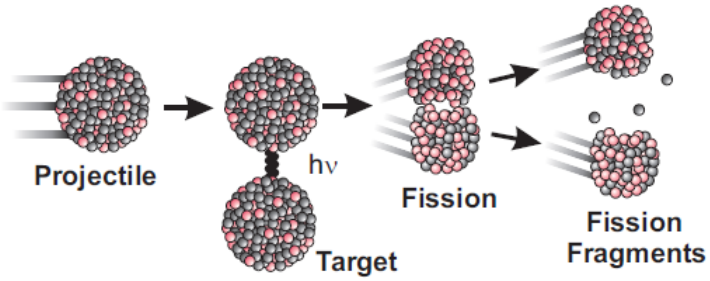

Figure 1.5: Representation of a coulomb-fission reaction via the exchange of a virtual photon between the projectile and the target nuclei [Geissel, 2018].

In the abrasion-fission reaction, the high energy projectile suffers the abrasion of part of the nucleons in a light target (for example beryllium), leading to the formation of an excited nuclei which can undergo fission, see Fig. 1.6.

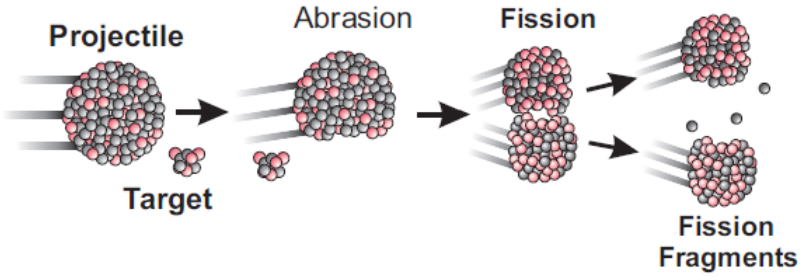

Figure 1.6: Schematic representation of abrasion-fission reaction, where a fissile nucleus is generated after the abrasion of part of the nucleons from the projectile. The target has much lower A than the projectile.

In a projectile fragmentation reaction, the abrasion of part of the nucleons from the projectile in a light target (for example beryllium) can generate a nucleus which will deexcite by the evaporation of nucleons (ablation) and the emission of gamma rays, see Fig. 1.7.

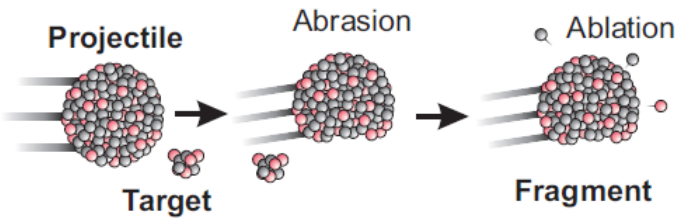

Figure 1.7: Schematic representation of the projectile fragmentation reaction. The target has much lower A than the projectile.

The block diagram of the in-flight separation method can be seen in Fig. 1.8. Here, the produced nuclei will not have low energies out of the target as in the ISOL technique,

flying through an electromagnetic separator where they are separated and selected. After separation and selection, the beam can be provided to experiments that accept ions at these high energies such as storage rings or in-flight spectroscopy experiments. Also, a secondary target can be included after the electromagnetic separator for further reactions of the produced fragments. Some of the strong points of this method are the short time needed to produce and deliver the nuclei to the experiments. This technique has the advantage to be chemistry-independent between target and projectile. Precision experiments carried at relativistic energies are challenging and require complex and rather big setups. This intrinsic characteristic will be addressed by the hybrid method, which was employed in this work and is presented in the next point.

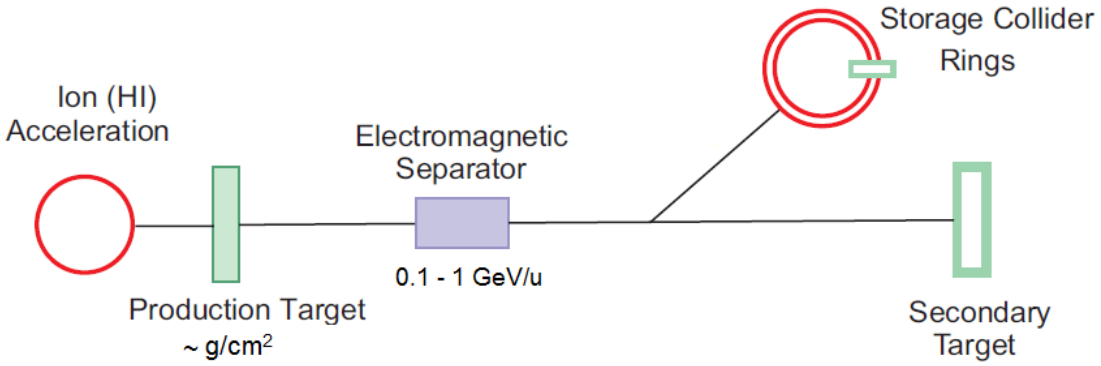

Figure 1.8: In-Flight-type production facility block diagram [Geissel et al., 2014, Geissel et al., 1995]. Red line: heavy ion (HI) accelerator infrastructure, red double line: storage rings, green: targets, violet: electromagnetic separator.

1.2.3 Hybrid Systems

In the hybrid method, the in-flight separated fragments are stopped in a gas-filled stopping cell and extracted, providing the exotic fragments at low energies (eV to keV). As can be seen in Fig. 1.9, the fragments are still produced in a thick target (few g/cm^2), as in the in-flight method, and are injected in the electromagnetic separator at relativistic energies (hundreds of MeV/u). After the separation and selection, and here is the main difference with the in-flight, the fragments are stopped in a gas-filled stopping cell. The stopped ions, can be delivered to low-energy precision experiments or re-accelerated in order to perform further nuclear reactions in a secondary target. This method keeps the strengths of the in-flight method, such as universal element production and chemistry independent. At the same time, it delivers the exotic fragments at low energies, being more convenient for precision experiments. The stopping of relativistic ions is done in few ms, being able to deliver also short-lived fragments at low energies. In this work a hybrid facility is used, the FRS-Ion Catcher. It is located at the Fragment Separator

(FRS) at GSI, and is composed of a cryogenic gas-filled stopping cell followed by precision low-energy experiments, where mass measurements of exotic nuclei have been performed.

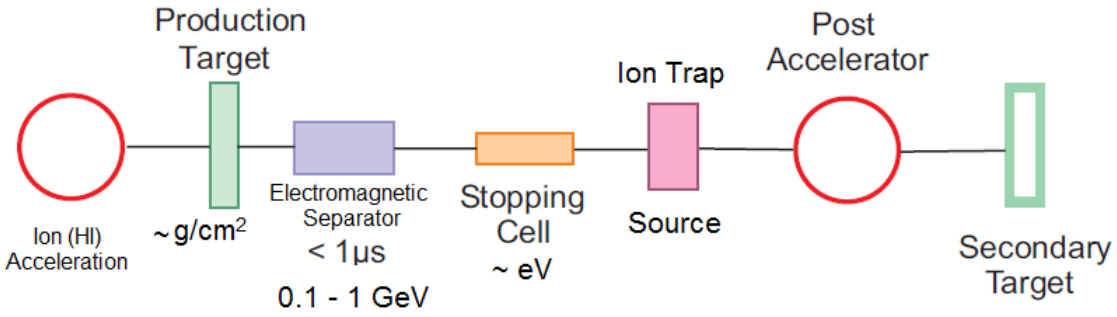

Figure 1.9: Hybrid-type production [Geissel et al., 2014, Geissel et al., 1995] block diagram. Color code as previous figure and in orange: stopping devices such as stopping cells.

1.3 Mass Measurement Techniques

The beginning of the mass measurements techniques started with Wien discovering the interaction of charged particles with electromagnetic fields. Wien discovered that under a strong magnetic field, particles of positively charged sign could be deflected in different trajectories depending on their mass-to-charge ratios [Wien, 1902]. Following Wien′s results, J.J. Thomson built a spectrometer where the charged particles were deflected with electromagnetic fields, where he saw different curvature lines for different mass-to-charge ratios. He saw two lines, of weight about 20 and 22 times the weight of the hydrogen (two neon isotopes), but at this time, he could not explain what he saw [Thomson, 1913]. The modern techniques differ in complexity and in many performance parameters (such as accuracy) by orders of magnitude from the first spectrometers, but in contrast, are based in the same principle as the beginning: interaction of charged particles with electromagnetic fields and the measurement of trajectories, time-of-flights (TOF), frequencies, etc. In this section, an introduction to the main modern mass measurement methods used in nuclear physics will be given. The focus of this introduction will be the multiple-reflection time-of-flight mass-spectrometer (MR-TOF-MS) because is the method used in this thesis.

1.3.1 Storage Rings

The produced relativistic exotic ions can be injected and stored in a storage ring (an arrangement of different magnets, detectors, etc. in a closed loop), where one can

measure the revolution time or frequency of the ions and get the mass-to-charge ratio [Litvinov et al., 2010]. There are two techniques for the measurement of the mass in a storage ring, which are graphically described in Fig. 1.10 and correspond to the storage ring ESR (Experimental Storage Ring) at GSI.

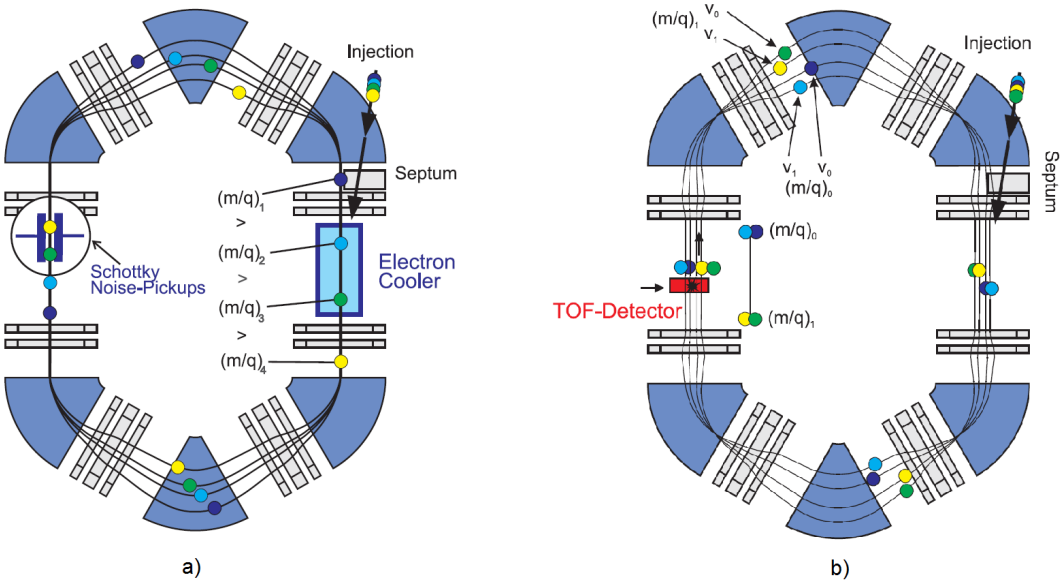

Figure 1.10: Illustration of both mass measurement techniques in the experimental storage ring (ESR) at GSI. **a)** SMS: in the picture, 4 ions with different mass-to-charge ratios are injected and cooled down by the electron cooler. The Schottky noise-pickups are then used to get the induced noise by the revolving charged particles in the ring and then determining the revolution frequency. **b)** IMS: in the picture, 4 ions of 2 different mass-to-charge ratios and different velocities are injected in the ring. The faster have longer paths to compensate the extra velocity. The TOF detector then detects the pass of the ions for every turn and with this information, the mass-to-charge ratio can be obtained.

The first one is called Isochronous Mass Spectrometry (IMS) [Geissel et al., 1992b], were the ion optics of the ring are tuned for compensating with different flight paths that different ions of the same mass-to-charge ratio have different velocities. Then the TOF, or revolution time, is measured by a detector positioned in beam (TOF Detector), recording each time an ion passes through the detector. One revolution to the ring is achieved in about 500 ns (2 MHz revolution frequency). The data from the TOF Detector is stored for few hundreds of μs (few hundreds of revolutions) to obtain the mass value. The second method, Schottky Mass Spectrometry (SMS) [Franzke, 1987, Schlitt et al., 1997], is based on recording the noise induced by the charged ions revolving in the ring with a noise pick-up detector. In this case, the velocity distribution of the ions is not compensated but reduced by means of stochastic and electron cooling. The process of cooling the ions is in the seconds scale and the overall mass measurement is then limited to nuclei with half-lives of few seconds. The

major advantage of the IMS technique is the short time needed to perform the mass measurement, which can be as low as tens to hundreds of microseconds. This advantage allows the technique to measure the mass of very short-lived exotic nuclei. On the other hand, the limited resolving powers on the few 10^5 with accuracy on the 10^{-6} level and long measurement time of few seconds (for the SMS technique), are the main disadvantages. For a comparison with other techniques see Tab. 1.2.

1.3.2 Penning Trap

A Penning trap is a device used for measuring masses of ions at low kinetic energies. Here, the ion is trapped in a strong magnetic field superposed with weak quadrupolar electric field. In Fig. 1.11, a typical construction of a Penning trap and the motion of the ion in the trap is shown. The ion motion inside the trap is the sum of the modified cyclotron motion (ω_{c+}), the magnetron motion (ω_m) and the axial motion (ω_a):

$$\omega_{total} = \omega_{c+} + \omega_m + \omega_a \tag{1.2}$$

The cyclotron frequency can be described as Eq. 1.3 [Kern et al., 1992, Gabrielse, 2009], where q is the charge state of the ion, m is the mass of the ion and B is the magnetic field.

$$\omega_c = \frac{q}{m}B = \sqrt{\omega_{c+}^2 + \omega_m^2 + \omega_a^2} \tag{1.3}$$

The frequencies of the different motions will be dependent on the trap parameters, magnetic field and the mass-to-charge ratio of the ion. The different amplitudes of the ion motions can be modified by applying an excitation of the given motion frequency. One way of calculating the mass of the ion is by obtaining the cyclotron frequency via the time-of-flight ion cyclotron resonance (TOF-ICR). If the ion is excited at the cyclotron frequency with a quadrupolar field generated in the ring electrodes, the magnetron motion will be transformed into a pure cyclotron motion. This will increase the radial kinetic energy of the ion since it will be rotating at a much higher frequency ($\omega_{c+} \gg \omega_m$) in a bigger radius. After the excitation, the ions are ejected towards a detector. If the radial kinetic energy was increased by appliying an excitation with the proper frequency (see Eq. 1.2), the inhomogeneities of the magnetic field towards the detector will convert the increased radial kinetic energy in the trap into an increase of axial kinetic energy, resulting in lower time-of-flight (TOF) of the ions between the trap and the detector [König et al., 1995]. By scanning the TOF for different excitation frequencies, one can obtain the reduced cyclotron frequency. In the different scans,

there can not be more than one ion in the trap (contamination or a second nuclei of interest) which would spoil the TOF-ICR measurement. With the measured reduced cyclotron frequency together with a measurement of the magnetic field by a reference ion and the magnetron frequency, one can obtain the mass-to-charge ratio.

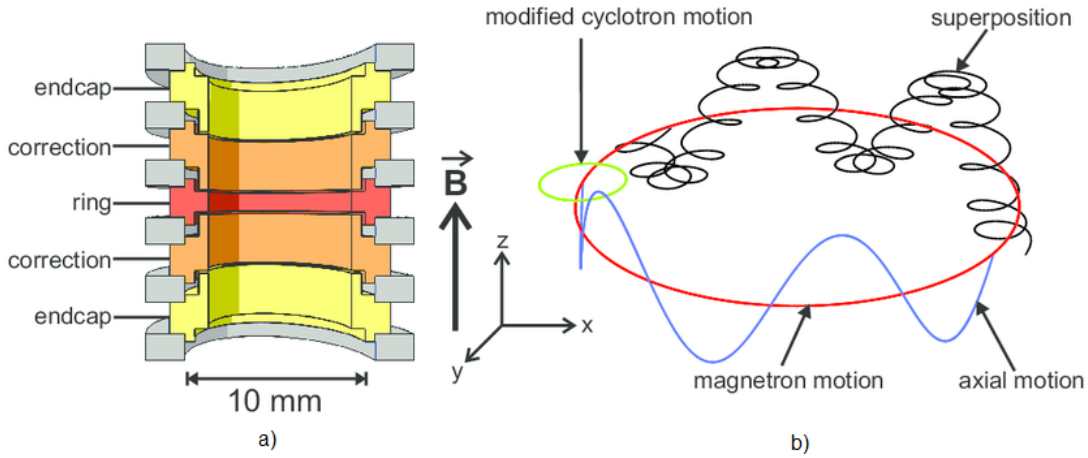

Figure 1.11: a) Section of a penning trap with the different electrodes for trapping and exciting the ion. b) Different motions of the ion in the Penning trap. Figure modified from [Smorra et al., 2015].

In the case of the penning traps, the main advantage is the high resolving power that can be achieved, being able to obtain the lowest mass uncertainties of the presented mass measurement techniques. The main disadvantage is the relative long time needed to perform the mass measurement (in the range of hundred milliseconds). It is worth to mention the relative new mass measurement technique, the Phase-Imaging Ion-Cyclotron-Resonance (PI-ICR) [Eliseev et al., 2013] technique which relies in measuring the radial phase evolution of the ion motion in a Penning trap with a position sensitive detector. This technique will push forward the performance characteristics of the penning traps. In comparison with the TOF-ICR, the PI-ICR technique will increase the resolving power and sensitivity of the mass measurements. In the other hand, is a narrow-band mass measurement technique, where multiple isobars cannot be measured at once. See Tab. 1.2 for a comparison.

1.3.3 Time-of-Flight Mass Spectrometers

In the time-of-flight mass-spectrometry (TOF-MS) technique, short bunches of charged atoms (ions) are injected with the same kinetic energy into a field-free drift region where they fly for a certain length. Due to the law of energy conservation, ions with different mass-to-charge ratios but with the same kinetic energy will have different velocities: higher for the lighter and lower for the heavier masses as depicted in Fig. 1.12. There are two main equations related with this technique, one for the kinetic

energy and the other for the velocity, Eq. 1.4 and Eq. 1.5 respectively, where q is the charge state, U is the potential, m is the mass, v is the velocity, l is the length and t is the time difference between start (ions are ejected) and stop (ions are detected), the time-of-flight (TOF).

$$qU = \frac{1}{2}mv^2 \tag{1.4}$$

$$v = \frac{l}{t} \tag{1.5}$$

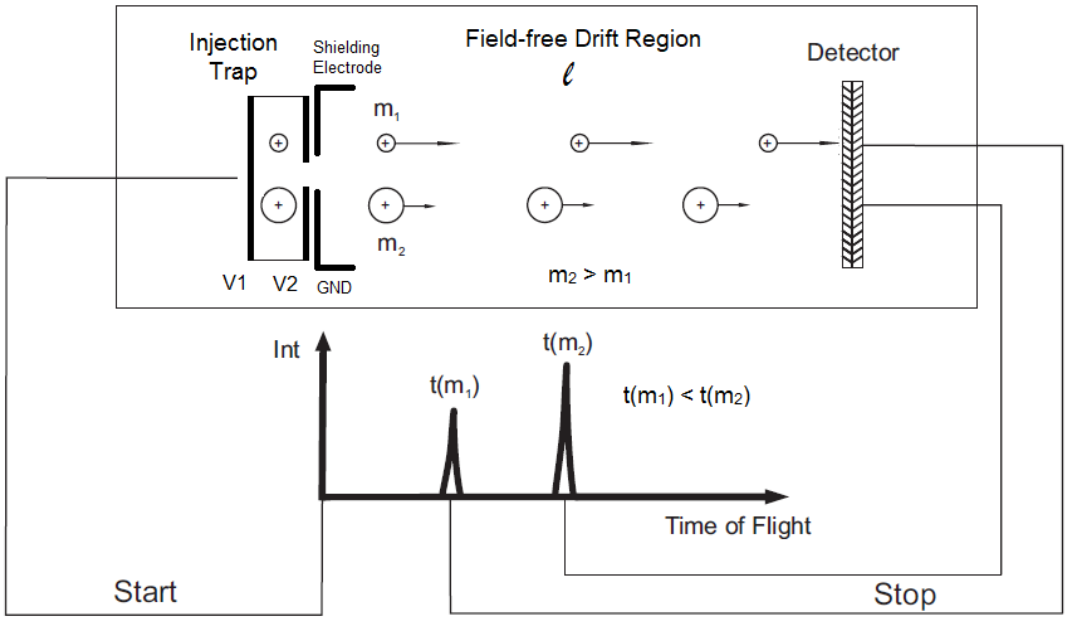

Figure 1.12: Time-of-flight mass spectrometer. Ions of different mass-to-charge ratio are bunched in the injection trap and stored at a given potential. Then at a start time, applying the extraction voltages to the electrodes of the injection trap, where V2 < V1 for positive ions, they are ejected to the field free drift region (detector assumed to be at ground potential), ideally all ions with the same kinetic energy and same starting point, fly towards the detector at different velocities due to the different mass-to-charge ratio. The time difference between the start and the ions impinging the detector is the so called time-of-flight (TOF). Picture modified from [Plaß, 1997].

Due to spatial distribution of the ions inside the injection trap, not all the ions with the same mass-to-charge ratio will have the same starting position. Therefore, they will not have the same starting potential neither the same flight path: the ions closer to the back plate of the injection trap (V1) will have higher potential and a longer flight path and the ions closer to the front plate (V2) will have lower potential and a shorter flight path (see Fig. 2.12 of [Jesch, 2016]). After some distance from the injection trap inside the drift region, the faster ions will catch the slower ions, reaching the primary

time focus [Dickel et al., 2017b]. If the detector is set in this position, the smallest TOF distribution will be obtained. On the other hand, if the detector is set at the end of a longer drift region, the TOF of the ions will start spreading again (the faster ions will then overcome the slower ions) and at the end no gain in resolving power for a longer drift tube will be obtained. The lack of a correction method to the energy spread obtained in the injection trap is the limiting factor to the mass resolving power of this technique. The mass resolving power (R_m), defined as in Eq. 1.6 where Δ_m corresponds to the mass distribution width (for example the full width at half maximum (FWHM)), will be in this particular case on the order of several hundreds.

$$R_m = \frac{m}{\Delta_m} \tag{1.6}$$

The solution to this problem was introduced by [Alikhanov, 1957] and [Mamyrin, 1966]. It consists in including a single reflector at the end of the field-free drift tube in order to correct the time focus due to the energy spread. Basically, the faster ions will penetrate deeper in this reflector, having a longer path. The energy difference will be then compensated by a difference in flight path, achieving the time focus in the detector. A sketch of a reflectron can be seen in Fig. 1.13. Even if this energy spread caused by the initial spatial distribution is perfectly compensated, the ion cloud will have certain time spread in the detector due to the thermal velocity of the ions in the injection trap. This thermal velocity causes a time needed by the ions with thermal velocity in the opposite direction of the ejection, to turn and gain velocity in the direction of ejection, the turn around time [Wiley and McLaren, 1955].

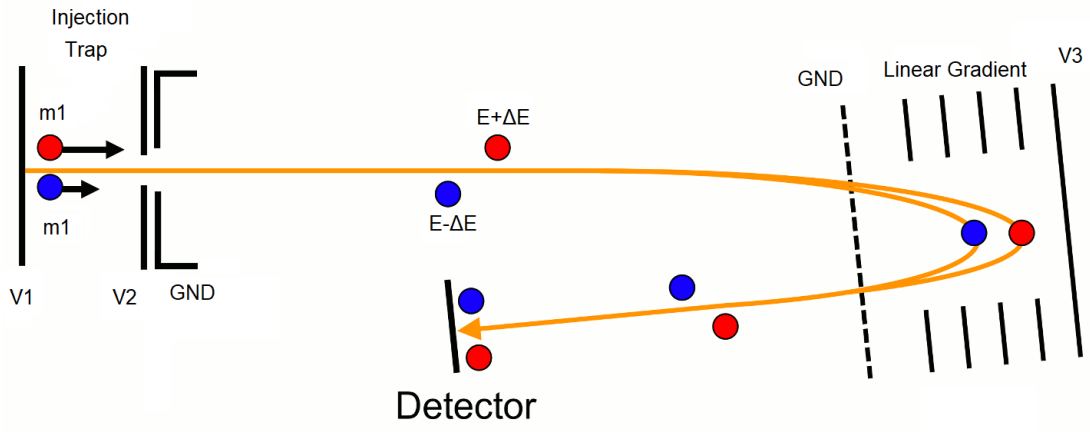

Figure 1.13: Drawing of a reflectron. Two ions of the same mass (m1) are injected with a kinetic energy spread of $\pm\Delta E$ in the field free-drift region. The reflection compensates the difference in kinetic energy with different path lengths, decoupling the time focus given by the injection trap and the final time focus, set to be in the detector. Adaption from [Wikipedia, 2018b].

The reflectron can achieve a mass resolving power of several thousands, limited by the size of the field-free drift region. To further increase the resolving power, increasing the flight path by increasing the field-free drift region is not a practical solution. The increase in flight path is achieved by trapping the ions inside an analyzer, composed of a field-free drift region and two coaxial electrostatic ion mirrors [Wollnik and Przewloka, 1990]. In Fig. 1.14, a representation of a time-of-flight and a multiple-reflection time-of-flight mass spectrometer is presented.

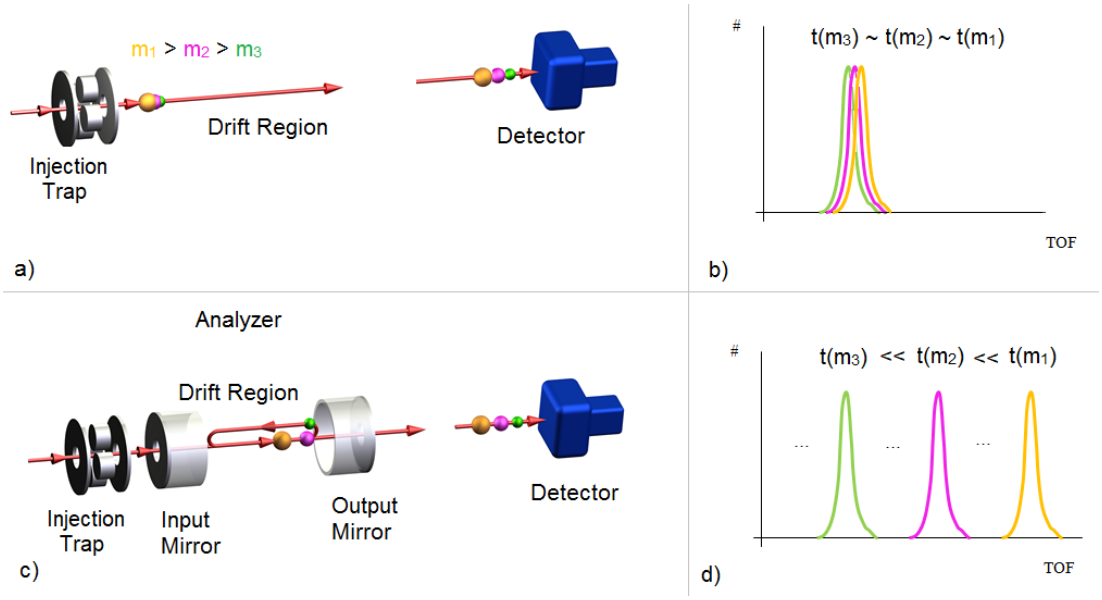

Figure 1.14: Illustration of a TOF-MS and a MR-TOF-MS, including a depiction of a recorded spectrum. a) TOF-MS with three different mass-to-charge ratios, analyzed from the injection trap to the detector. b) Example of spectrum obtained by the TOF-MS technique. Note the peaks are not resolved due to the low mass resolving power (several hundreds). c) MR-TOF-MS implemented with two pulsed electrostatic mirrors for trapping the ions. d) Representation of a spectrum obtained by the MR-TOF-MS, where due to the longer flight path higher spatial and TOF separation are achieved.

The mirrors can keep the initial time focus given by the injection trap unchanged (isochronous reflection), or shift the time focus towards the detector. This change in time focus is achieved by changing the voltages applied to them [Dickel et al., 2017b]. If no time focus is performed in the analyzer, a time focus shift reflector can be included afterwards for shifting the time focus, similar to the reflectron. The total flight path will be increased by the number of isochornous turns (N_{IT}) that the ions perform inside the analyzer, increasing the resolution of the device. For injecting or ejecting the ions in or from the analyzer, the potential of the mirrors or of the drift region can be switched [Wolf et al., 2012].

The time-of-flight to mass relationship can be calculated as in the following. First, there will be some electrical delay between the start signal and the injection into the

analyzer, t_0. After travelling l_{in} in a time t_{in} the ions will be located between the two mirrors, and at this time, the input mirror will be closed. Since the output mirror is also closed, the ion will be reflected many times, and after N_{IT} isochronous turns, will have flown for $N_{IT} \cdot t_{IT}$ time and $N_{IT} \cdot l_{IT}$ length, where t_{IT} is the time needed by the ions to perform one isochronous turn and l_{IT} is the length travelled in one isochronous turn. If now the output mirror is opened when the ion is at the same position as when the input mirror was closed, another segment of length l_{out} will be travelled in a time t_{out} towards the detector. The input and output time and length (t_{in}, l_{in} and t_{out}, l_{out}) correspond to the time and path between the ejection trap until the detector without performing any isochronous turn, only the time focus shift (t_{TFS} , l_{TFS}). Then the total time of flight and the total flight path can be written as Eq. 1.7 and Eq. 1.8, respectively.

$$t_{total} = t_{in} + t_{IT} \cdot N_{IT} + t_{out} + t_0 = t_{TFS} + t_{IT} \cdot N_{IT} + t_0 \tag{1.7}$$

$$l_{total} = l_{in} + l_{IT} \cdot N_{IT} + l_{out} = l_{TFS} + l_{IT} \cdot N_{IT} \tag{1.8}$$

If the Eq. 1.4, 1.5, 1.7 and 1.8 are used, the mass in terms of time-of-flight can be expressed as [Haettner, 2014]:

$$m = \frac{2qU(t_{total} - t_0)^2}{{l_{TFS}}^2(1 + N_{IT} \cdot \frac{l_{IT}}{l_{TFS}})^2} \tag{1.9}$$

The t_{total} will be the measured time. $\frac{l_{IT}}{l_{TFS}} = b$, $\frac{2qU}{{l_{TFS}}^2} = c$ and t_0 will be constants that will be determined by measuring the total TOF of calibration masses. The resolving power in terms of time distribution of the arrival time of the ions (Δ_t) in Eq. 1.10.

$$R_m = \frac{t_{total} - t_0}{2\Delta_t} \tag{1.10}$$

The major advantage of this technique is the unique combination of the different parameters, especially the high sensitivity and the short measurement time combined with a broadband measurement range, which are key points for the measurement of exotic nuclei due to their short half-lives and low production rates.

In Tab. 1.2 a comparison of the main parameters of the mass measurement techniques presented in this section is given.

Technique	Maximum Resolving Power m/Δm	Typical Measurement Time	Minimum Number of Detected Nuclei Needed	Typical Relative Uncertainty (δm/m)	Scanning?
Storage Rings (IMS)	1 - 2 · 10^5	10 - 100 μs	2	10^{-6}	No
Storage Rings (SMS)	5 - 6 · 10^5	5 - 60 s	1	$3 \cdot 10^{-7}$	No
Penning Trap (TOF-ICR)	1 - 2 · 10^6	100 ms	100	high 10^{-8}	Yes
Penning Trap (PI-ICR)	> 2 · 10^6	100 ms	100	low 10^{-8}	No
MR-TOF-MS	4 - 5 · 10^5	20 ms	10	10^{-7}	No

Table 1.2: Comparison of the typical main parameters of the different mass measurement techniques used in nuclear science nowadays. Shown are the typical values with conditions given for exotic nuclei (short half-lives and low production rates) of medium mass (A = 150). Different references have been used for the completion of this table. IMS: [Knöbel et al., 2016], SMS: [Litvinov et al., 2005, Chen et al., 2010], TOF-ICR: [Blaum et al., 2013] and for the MR-TOF-MS: [Ebert, 2016, Hornung, 2018, Ayet San Andrés, 2018]. The PI-ICR technique is in development, therefore, the values given here correspond to measurements of long-lived nuclei and are based on [Eliseev et al., 2013, Orford et al., 2017].

2 The FRS-Ion Catcher Experiment

In this chapter, a description of the FRS [Geissel et al., 1992a] and the FRS-Ion Catcher [Plaß et al., 2013a] will be presented. The FRS, in combination with the FRS-Ion Catcher, will allow to perform experiments of exotic nuclei at low energies (see Section Hybrid). The FRS-Ion Cather is divided in 3 main parts: (i) the gas-filled cryogenic stopping cell (CSC) for thermalizing the exotic nuclei produced at relativistic energies, (ii) a beamline based on radio frequency quadrupoles (RFQ) for mass selective transport and differential pumping, which is equipped with detectors (channeltrons and silicon detectors) and ion sources for diagnostic purposes (counting, α-decay energy measurement), called diagnostic unit (DU), and finally, (iii) an MR-TOF-MS for performing direct mass measurements.

2.1 Fragment Separator

The Fragment Separator (FRS) is a high resolution magnetic spectrometer for in-flight separation [Geissel et al., 1992a] which is located at the GSI Helmholtz Center for Heavy Ion Research as shown in Fig. 2.1.

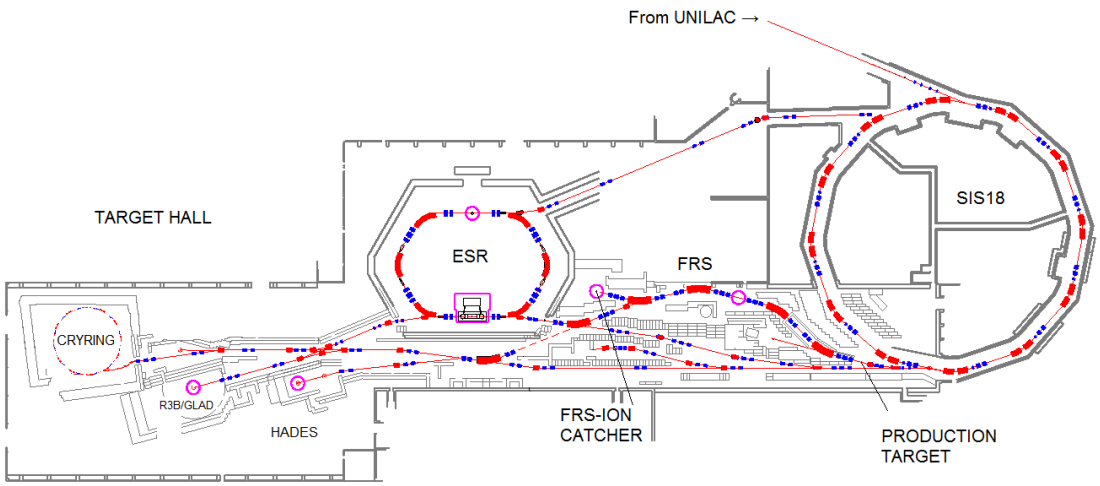

Figure 2.1: Schematic view of the GSI facility after UNILAC showing the main experimental areas and the location of the FRS-Ion Catcher. Picture modified from [Wollersheim, 2018].

Elements, ranging from protons to uranium, are first accelerated at the Universal Linear Accelerator (UNILAC) to ∼11.4 MeV/u. Afterwards they are injected into the heavy ion synchrotron, SIS-18, where they get further accelerated to relativistic energies. The relativistic primary beam is extracted towards the FRS, where it interacts with the production target undergoing nuclear reactions generating exotic fragments (see Section In-Flight). The fragments are in-flight separated in the FRS. The schematic view of the FRS with the FRS-Ion Catcher in the final focal plane is shown in the Fig. 2.2.

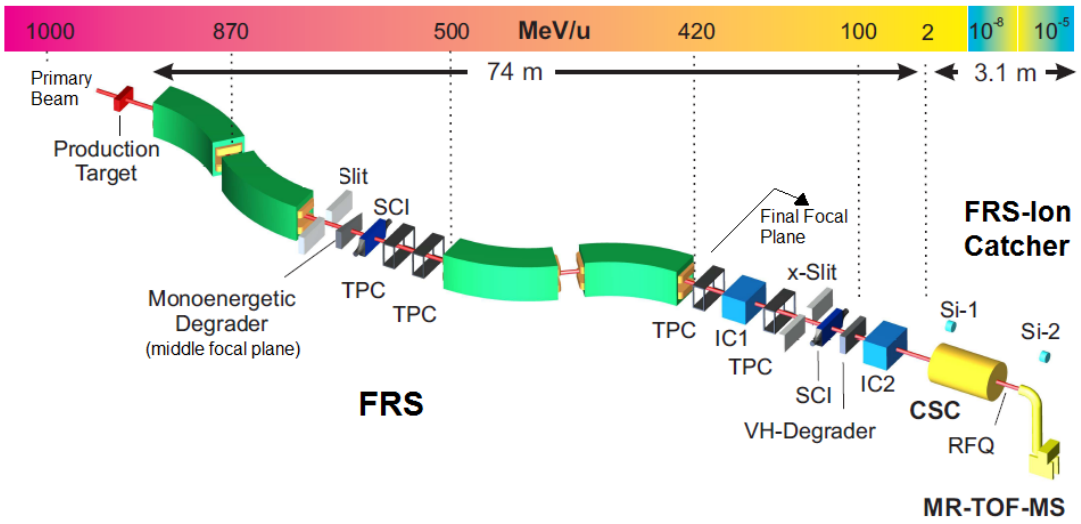

Figure 2.2: Schematic view of the FRS and the FRS-Ion Catcher including the typical energy of the ions during their travel through the FRS until they are stopped in the CSC. The scintillators (SCI), time projection chambers (TPC) and ionization chambers (IC) are used for particle identification (PID) via Bρ-ΔE-TOF measurements [Farinon, 2011].

The FRS is a two stage magnetic spectrometer where each stage consist of: two dipole magnets for magnetic rigidity analysis and ten quadrupole magnets and several sextupole magnets for focusing and ion optical corrections. For the separation, the Bρ-ΔE-Bρ method is used. The first magnetic spectrometer stage will select a certain mass-to-charge ratio (m/q) with its magnetic rigidity (Bρ) depending on the velocity of the fragments. There is a dispersive middle focal plane located between both stages, where different m/q will have different positions. Since the energy loss of the ions penetrating through matter depends on the Z^2, with the help of a specially shaped degrader in the dispersive focal plane, different Z for similar m/q ions will have different momentum after the degrader due to their difference in energy loss (ΔE). Thanks to the high energy of the beam delivered by the SIS-18, even the heaviest elements are fully stripped after penetrating the degrader. In the second stage, this difference in energy loss will also be selected by the magnetic rigidity of the second stage (Bρ), achieving at the final focal plane a separation in m/q and Z. The spectrometer can be tuned in an achromatic mode, resulting in the final focal plane in a minimum spatial

distribution of the fragments, or in monoenergetic mode, resulting in a minimum energy distribution in the final focal plane. The monoenergetic mode is the preferred one for implantation experiments, where the range distribution of the fragments has to be minimized. A specially shaped degrader in the middle focal plane (monoenergetic degrader) bunches the energy of the fragments [Weick et al., 2000] to efficiently stop them in the CSC. In the last meters, the energy of the fragments is reduced by means of degraders, whose thickness is adjusted such that the fragments of interest are stopped inside of the CSC.

2.2 Cryogenic Stopping Cell and Diagnostic Unit

The cryogenic stopping cell (CSC) is the device responsible for the final slowing down and thermalizing the energy-bunched fragments produced and selected in the FRS. The thermalization is achieved in a volume filled with ultra-pure helium gas at cryogenic temperatures [Schäfer, 2010, Ranjan et al., 2011, Ranjan et al., 2015]. After the thermalization, the fragments are extracted and transported with a RFQ based beamline to the MR-TOF-MS (see Fig. 2.3). The diagnostic unit (DU) provides also a differential pumping stage between the systems, ion counting and identification capabilities [Miskun et al., 2015].

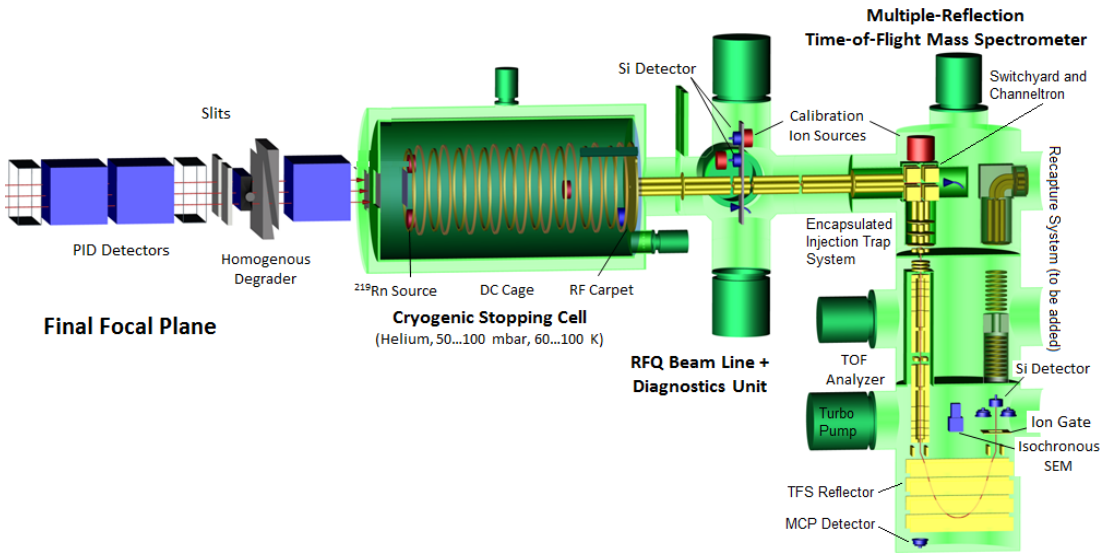

Figure 2.3: The FRS-Ion Catcher set-up, including FRS detectors in the final focal plane used for particle identification, is shown. The main components of the FRS-Ion Catcher are: (i) the CSC, (ii) the RFQ Beamline and Diagnostic Unit and (iii) the MR-TOF-MS.

A cross section of the CSC can be seen in detail in Fig. 2.4. It is a double chamber device. The outer chamber is at room temperature and the inner chamber is thermally

isolated by vacuum at cryogenic temperatures. Inside the cryogenic chamber, concentric electrode rings (DC Cage) are mounted to generate an electric field gradient for pushing the stopped positive charged ions towards the exit (right direction in the Fig. 2.4), where they will be extracted by a radio-frequency ion guide (RF Carpet). The RF Carpet is a PCB based ion guide composed of 500 concentric electrodes, with 250 μm pitch and 125 μm of spacing for the electrodes (see detail of Fig. 2.4). An RF signal is applied to the odd electrodes and the same signal with a 180° phase shift is applied to the even electrodes. This RF counteracts the pushing force applied by the electric fields of the DC cage, preventing the ions to impinge in the RF Carpet. In combination with the RF signal, a DC gradient along the RF Carpet electrodes is applied to generate an electric field that guides the ions towards the exit nozzle. The exit nozzle is a metal cylinder (PCB via) with a diameter of 0.6 mm and a length of 1.3 mm. The combination of RF and DC fields transports the stopped fragments towards the exit nozzle, where thanks also to the gas flow, they are finally extracted.

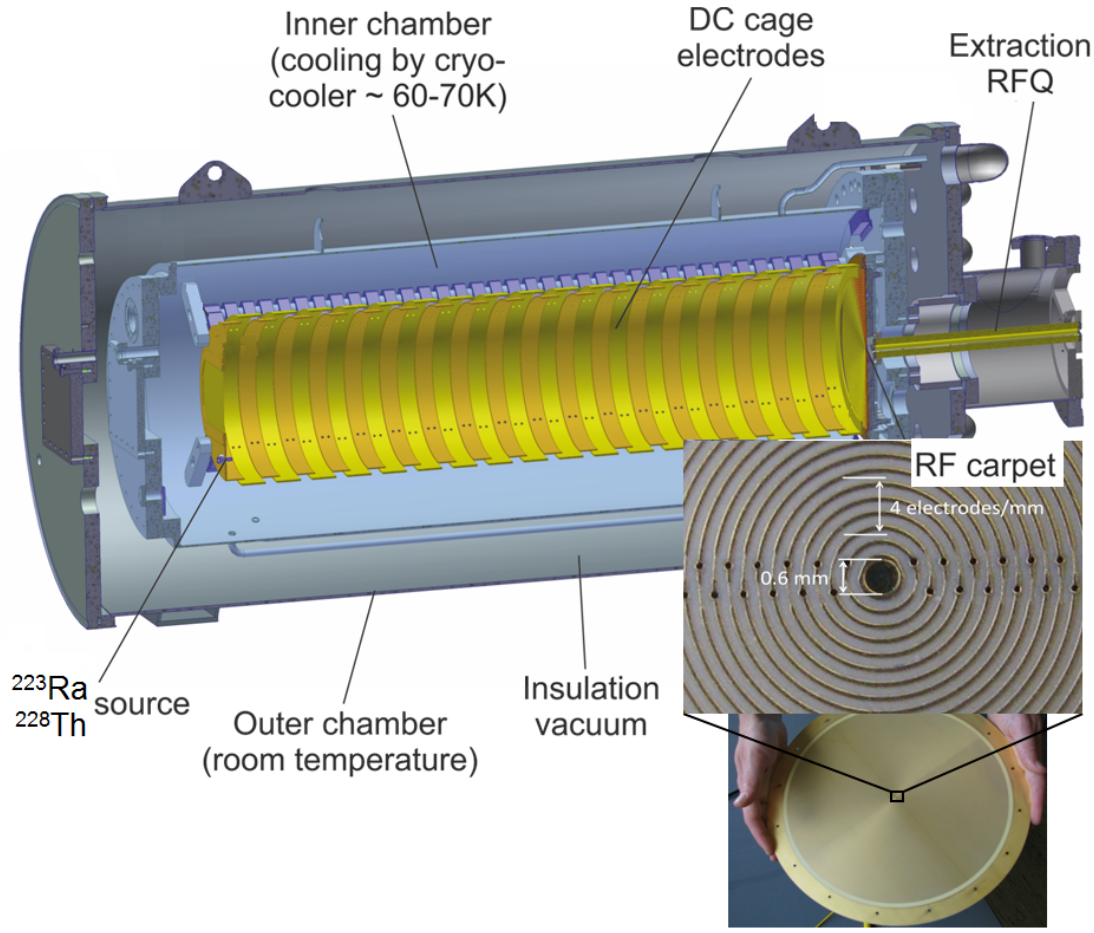

Figure 2.4: CSC section showing the different chambers and electrodes used for guiding the ions towards the exit nozzle. Also, a detailed picture of the RF Carpet ion guide is shown with a zoom to the exit nozzle where the ions are finally extracted from the CSC.

Behind the CSC, the DU is able to work as a compact RFQ transport beamline, where also collision induced dissociation (CID) of molecules extracted from the CSC can be performed. This is achieved by accelerating the extracted products in the gas filled RFQs to some tens of eV, where the molecules will heat up due to collisions and dissociate [Greiner, 2017]. It can also work as a diagnostic device using three detectors: two silicon detectors for α-decay spectroscopy and a channeltron for stable ion detection. The system can be seen in Fig. 2.5. A short segment of the beamline, of a length of few centimeters, can be moved in few seconds from transport mode to the different detectors mentioned above. Also a gate valve can be used to isolate the vacuum from the CSC and the MR-TOF-MS by moving a second RFQ. Towards the MR-TOF-MS, a thermal ion source is mounted in order to check the transport from the DU to the MR-TOF-MS.

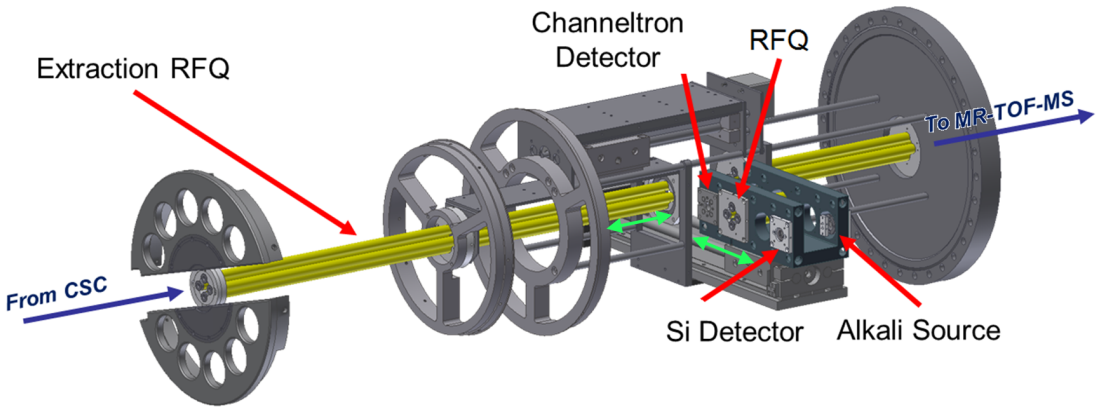

Figure 2.5: Drawing of the versatile beamline for transport and diagnostics located between the CSC and the MR-TOF-MS. Ions are delivered from the CSC on the left side of the picture and transported towards the MR-TOF-MS, on the right of the picture. The moveable RFQs are depicted with green arrows [Reiter, 2015].

2.3 Multiple-Reflection Time-of-Flight Mass Spectrometer

A drawing of the multiple-reflection time-of-flignt mass-spectrometer (MR-TOF-MS) [Plaß et al., 2008] can be seen in Fig. 2.6. The mass spectrometer is based on the technique described in 1.3.3.

The device can be used for direct mass measurements of thermalized exotic nuclei or as isomer separator for purifying the beam with the Bradbury–Nielsen gate (BNG), located behind the analyzer [Dickel et al., 2015, Hornung, 2018]. On the entrance of the MR-TOF-MS, a gas-filled RFQ-based switchyard (RF Switchyard)

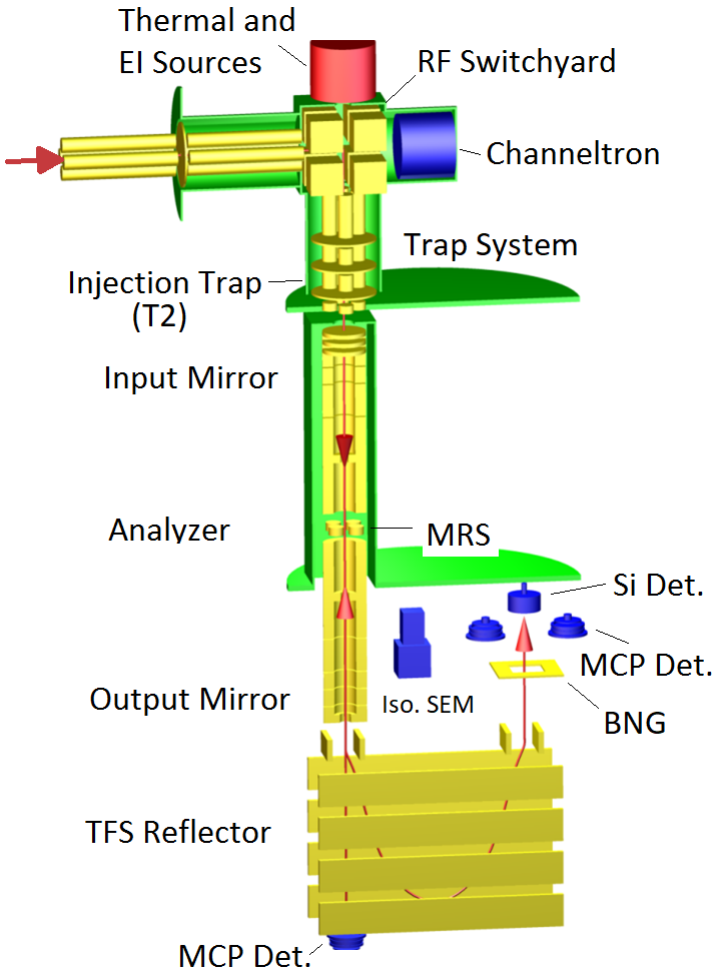

Figure 2.6: Drawing of the MR-TOF-MS of the FRS-Ion Catcher. The top-left red arrow represents the incoming ions from the CSC via the DU. The other red arrows represent the ion paths in the system. A movable detector system can be set to perform mass measurements with an isochronous secondary emission multiplier (SEM) or mass-selective α-decay measurements with a combination of a Bradbury–Nielsen gate and a silicon detector. In this case, micro-channel plate (MCP) detectors can be used to monitor the deflected ions.

[Greiner, 2013, Plaß et al., 2015, Ebert, 2016], can merge the ions extracted from the CSC with calibration ions from a thermal and electron-impact ion sources. The ions entering the MR-TOF-MS have a kinetic energy of the order of eV. They are bunched in T0 and transported to the injection trap (T2) over the trap system [Jesch, 2009], see Fig. 2.7. In T2, the reference potential of the ions is lifted from about -100 V to 1300 V (see Fig. 2.8). Then, the ions are injected towards the analyzer, which has the drift tube at ground potential, gaining a kinetic energy of 1300 eV. All the timings and the generation of the logic signals, for controlling the potential of the different electrodes along the ion path, is done via an FPGA-based system [Jesch, 2016].

The analyzer consists of two electrostatic ion mirrors, input and output, of 4 electrodes

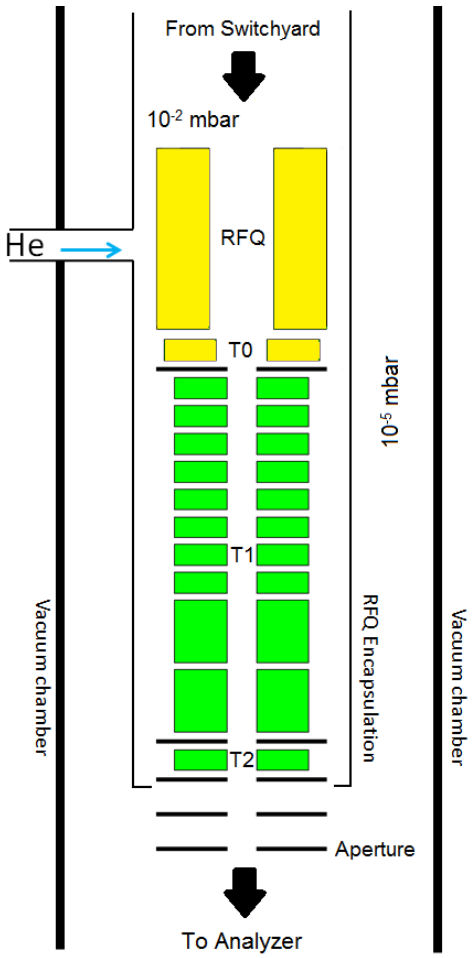

Figure 2.7: Encapsulated injection trap system of the MR-TOF-MS. In yellow the electrodes with sinusoidal RF and in green the electrodes with square RF are depicted. The ions are delivered from the switchyard, bunched in T0, transported to T1 and then transported to T2. The potential lift is performed at T2 where the ions are stored in a RFQ segment surrounded by two apertures. The potential of the segment and the apertures is raised to the desired potential, shifting the potential reference of the ions. Note that due to the encapsulation, the internals of the Injection System are difficult to pump, therefore contaminants from the helium gas or inside the trap system will not be easily removed. On the other hand, less residual helium will reach the analyzer and less losses due to collisions will happen in the analyzer.

each and a field free drift region at ground potential with a mass range selector (MRS) located in the centre. By switching the input mirror of the MR-TOF-MS, the ions can be injected in the analyzer, where they are trapped for certain number of isochronous turns in order to increase the flight path and the spatial separation of the different ions according to their mass-to-charge ratios. After the ions have traveled a certain number of turns, the analyzer exit mirror is opened letting the ions escape from the analyzer and perform a last reflection in the time focus shift (TFS) reflector, shifting the time focus plane of the ions onto the detector plane [Dickel et al., 2017b].

2.3.1 Operation and Performance

The MR-TOF-MS was first commissioned in 2008 [Plaß et al., 2008, Dickel, 2010]. The system was running with a kinetic energy of 750 eV at a repetition rate of up to 400 Hz. The analyzer mirrors were opened or closed by pulsing the voltage of two different electrodes on each mirror. When the mirrors were closed, the voltages were provided by high performance Iseg (www.iseg-hv.com) power supplies and an extra stabilization circuitry [Czok, 2010]. The system was able to reach up to 600000 mass resolving power after 49 ms of total TOF in offline conditions with a special optical tuning, but the reliability and stability of the system did not allow to perform long term measurements. The buffer gas delivered to the encapsulated trap system and RFQs was clean enough to transport low ionization potential (IP) elements, but not enough to transport high IP or highly reactive elements. This hindrance of the transport occurs due to charge exchange and reactions (e.g. formation of adducts) of the ions with the impurities of the buffer gas (hydrogen, oxygen, water, hydrocarbons, etc.), which causes the neutralization and loss of the ions. A summary of the performance characteristics of the MR-TOF-MS before this work is listed in Tab. 2.1.

Parameter	**Performance**	**Limiting Device**
Kinetic Energy	$\leqslant$ 750 eV	Potential Lift Electronics
Repetition Rate	$\leqslant$ 400 Hz	Potential Lift Electronics
Temp. Coefficient of TOF	20 ppm/°C	Power Supplies and Voltage Stabilization
Max Resolving Power	600000 in 49 ms of TOF	Analyzer Electronics (Stabilization)
Buffer Gas Cleanliness	Low efficiency for high IP or highly reactive elements	No gas cleaning device used

Table 2.1: Performance characteristics of the MR-TOF-MS in 2010. Data extracted from [Dickel, 2010].

2.3.2 Developments and Improvements

A major part of this work focuses on improving the routinely performance of the MR-TOF-MS under real experimental conditions. In the following section, a deeper understanding of each parameter described in Tab. 2.1, with a description of the improvement implemented and a comparison of the performance before and after the improvement, will be presented.

2.3.2.1 Increase of Kinetic Energy and Repetition Rate

As already discussed, the ions are delivered and transported from the CSC or the calibrant source to the MR-TOF-MS at low energies (eV) with a reference potential of $\pm$ few tens of volts. In order to get higher resolving powers in less time-of-flight (TOF), the kinetic energy of the ions has to be increased, limited previously to 750 eV [Jesch, 2009]. The higher kinetic energy will increase the flight length for the same TOF and reduce the emittance of the ions in the analyzer, obtaining an overall increase in the resolving power [Plaß et al., 2015]. The ions get this kinetic energy by the potential difference between the injection trap and the drift region of the analyzer. This potential difference can be obtained either by setting the potential of the drift region lower than the potential of the injection trap or by setting the potential of the injection trap higher than the potential of the drift region. In this system, the potential of the injection trap (T2) is lifted to P_{lift} (1300 V, formerly limited to 750 V) keeping the reference potential of the analyzer fixed to ground potential. The injection trap consists of a small RFQ segment (TS_19) with square RF applied and two apertures (TS_17 and TS_20), see Fig. 2.8.

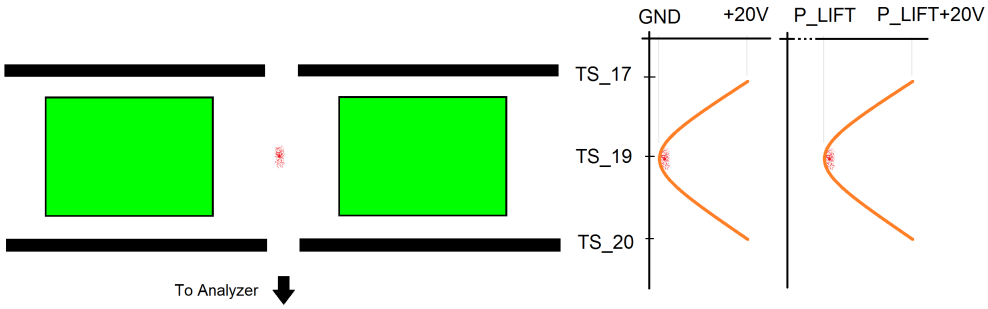

Figure 2.8: On the left, section of the trap T2 with some ions stored in the centre (red dots) is depicted. In black the apertures (TS_17 and TS_20) and in green 2 out of 4 electrodes of the RFQ segment (TS_19) are shown. On the right, in orange the DC potential section formed in the trap by the three electrodes before and after the lift to a P_{lift} potential is depicted. Besides the DC, an RF signal is applied to the RFQ segment TS_19.

The electronics that provide the potentials to the trap system were redesigned to be able to reach a potential lift to more than 1300 V and a repetition rate exceeding 1000 Hz, limited before to 750 eV and 400 Hz. The RFQ segment is controlled by a newly developed two-phase RF generator based on a double half-bridge metal–oxide–semiconductor field-effect transistor (MOSFET) in push-pull configuration. It can pulse a maximum of 500 V at frequencies exceeding 4 MHz. The power dissipated of up to 50 W per phase limits the possible amplitude-frequency combinations, see Appendix A.1 for more information. The generated RF, shifts the reference potential from -100 V to a desired P_{lift} potential in less than 50 ns at a rate of more than

1000 potential shifts per second, allowing to run the MR-TOF-MS with a repetition rate exceeding 1000 Hz. In Fig. 2.9, the block diagram of the electronics developed for generating the potential lift and the RF for trapping the ions in TS_19 is presented. The same concept is used for T1 and the rest of the electrodes driven by square RF in the trap system. A total of 4 voltages are generated by two floating power supplies (CGC Instruments), two voltages for the RF signal at low potential level and two voltages for the RF signal at high potential level. The pulsers PHV_1 and PHV_2 and the pulsers PRF_1 and PRF_2 were designed in the framework of this thesis (see Appendix A.1 for more information).

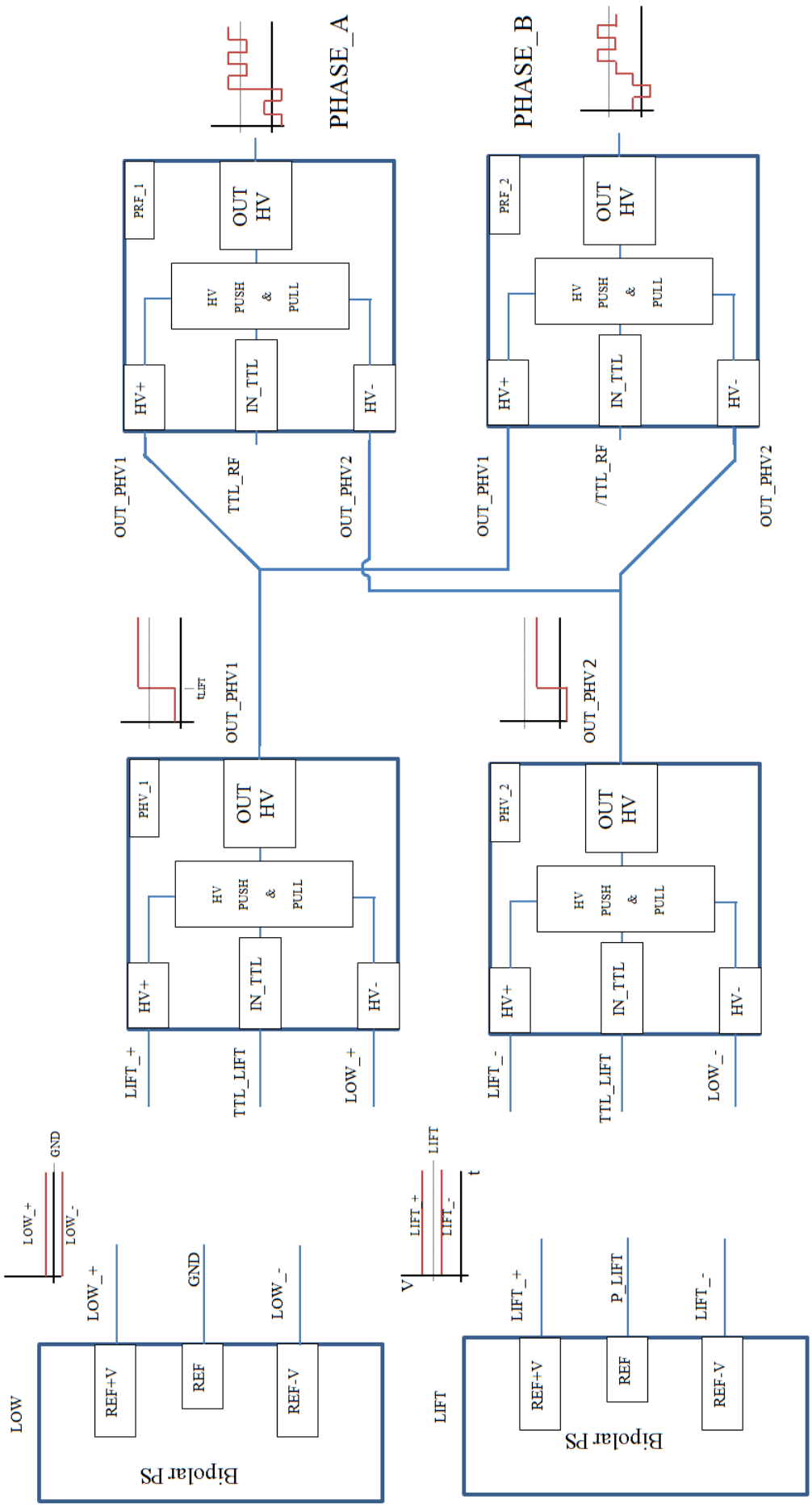

Figure 2.9: Block diagram of the electronics designed to generate the potential lift and the RF: two bipolar floating power supplies, one referenced to ground and the other to P_Lift, two High Voltage Current Pulsers (PHV_1 and PHV_2) and two RF Pulsers (PRF_1 and PRF_2). The concept is the same used in [Jesch, 2016] but the pulser electronics have been redesigned. See Appendix A.1 for more information about the newly designed pulsers.

The pulsers that drive the apertures TS_17 and TS_20 during potential lift and ejection were also redesigned. This allowed the application of higher potential difference between TS_17 and TS_20 during ejection, increasing the extraction field strength in T2 from 31 V/mm to 72 V/mm even at high repetition rates. This reflects in a lower initial time spread of the ions (lower turn around time) which is essential to achieve a given resolving power in shorter time of flight [Plaß et al., 2015] as shown Eq. 2.1.

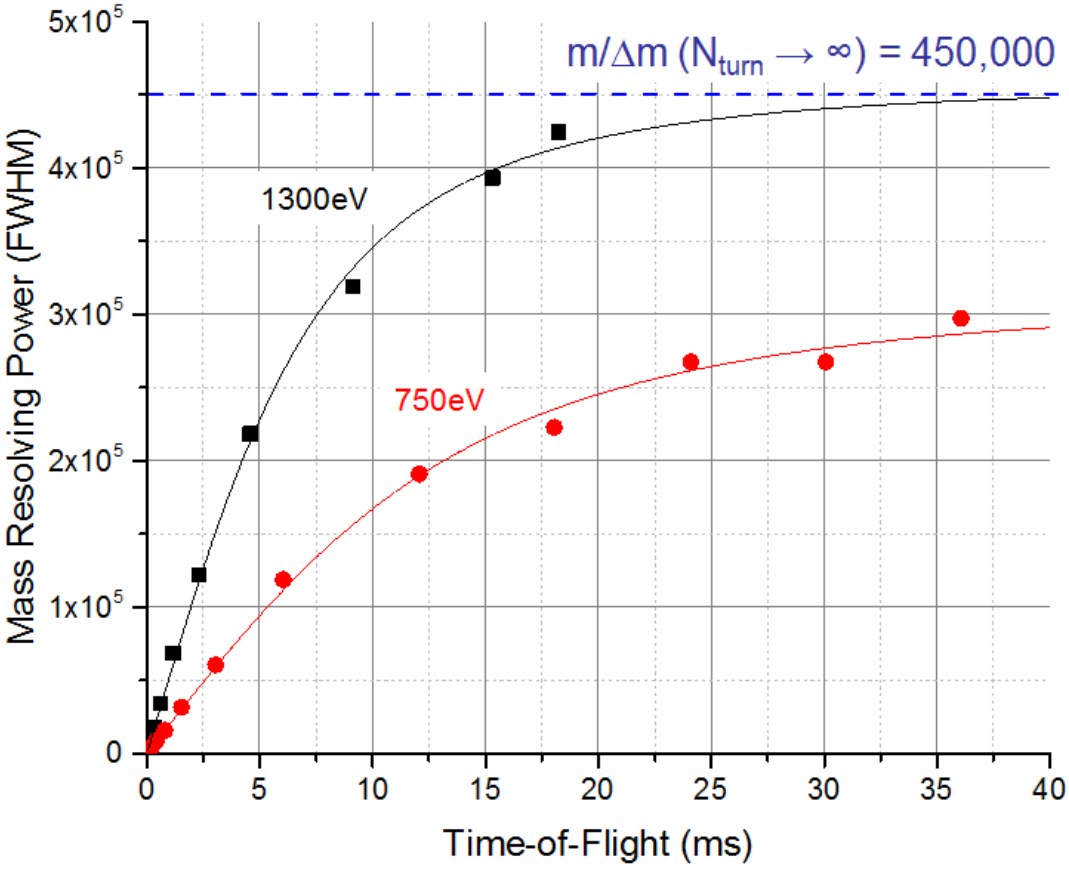

Figure 2.10: Typical mass resolving power for $^{133}Cs^{+1}$ ions vs. TOF for the kinetic energies before and after the upgrade of the potential lift electronics. Picture adapted from [Plaß et al., 2015]. Red circles: data measured with 20 Hz repetition rate, 750 eV kinetic energy and 31 V/mm of extraction field strength in T2. Red line: fit to the data with Eq. 1.4. Black squares: data measured with 50 Hz repetition rate, 1300 eV kinetic energy and 72 V/mm of extraction field strength in T2. Black line: fit to the data with Eq. 2.1. The theoretical maximum mass resolving power shown is calculated for $N_{IT} \rightarrow \infty$.

The new RF generation electronics for the trap system were installed and stable operation with a kinetic energy of 1300 eV and an extraction field strength of 72 V/mm was achieved. In Fig. 2.10, a comparison of the mass resolving power (MRP) for the 750 eV and 1300 eV kinetic energies, with 31 V/mm and 72 V/mm extraction field strength respectively, is presented. The mass resolving power in dependency on the number of turns can be approximated by Eq. 2.1 [Plaß et al., 2013b], where t_{IT} is the

time-of-flight for one turn in the analyzer, $t_{TFS} = t_{in} + t_{out}$ is the time-of-flight from the injection trap to the detector without any isochronous reflection in the analyzer, Δt_{TFS} is the initial time spread (including the turn-around time, inversely proportional to the extraction field strength), N_{IT} is the number of isochronous turns in the analyzer and Δt_{IT} is the time-of-flight spread added on each turn due to the optical aberrations of the analyzer. The improvement due to the increase in kinetic energy is reflected in the maximum achievable resolving power by lowering the emittance of the ions in the analyzer, which reduces the effect of the aberrations in the analyzer. The increase of the extraction field strength in the injection trap reduces the initial time spread of the ions (Δt_{TFS}), obtaining a higher resolving power for short times-of-flight.

$$\frac{m}{\Delta m} = \frac{t_{IT} + \frac{t_{TFS}}{N_{IT}}}{2 \cdot \sqrt{(\frac{\Delta t_{TFS}}{N_{IT}})^2 + (\Delta t_{IT})^2}} \tag{2.1}$$

In a next step, the analyzer ion optical tuning was optimized. This was done with a relative light element ($^{39}K^{+1}$) to have a longer flight path with the maximum flight time of 20 ms for the 50 Hz repetition rate. In Fig. 2.11, the MRP vs. TOF is shown for $^{39}K^{+1}$ ions at 1300 eV kinetic energy with the MR-TOF-MS running at 50 Hz repetition rate.

Fitting again with Eq. 2.1, a limit in the resolving power of 870000 was obtained for $N_{IT} \to \infty$. In the limit of the flight time (20 ms) used for this measurement, a mass resolving power of 600000 was achieved. This corresponds for a mass of 39 u to a mass resolution at FWHM of about 65μu or 60 keV/c^2. The time-of-flight spectrum of $^{39}K^{+1}$ taken over 60 s for the highest resolving power (1024 turns), exceeding 600000, is shown in Fig. 2.12. This high resolving power enables with only 10 counts, a mass measurement with a relative statistical mass uncertainty of about $2 \cdot 10^{-7}$, enough to pin down information about nuclear structure or nuclear astrophysics.

Not only the resolving power was improved but also the repetition rate was increased to more than 1000 Hz, allowing handling higher ion rates when using the spectrometer as an isobar separator or measuring nuclides with shorter half-lives. However, by increasing the repetition rate of the device, the maximum TOF is limited and therefore the resolving power, so a trade-off between resolving power (important to achieve the desired mass accuracy) and measurement time (important for short-lived nuclei) has to be taken. As an application of the new capabilities of the system, first direct mass measurement of a short-lived (1.78 ms) nuclei, ^{215}Po, was performed with a repetition rate of 400 Hz (2.5 ms cycle time), a kinetic energy of 1300 eV and mass resolving powers exceeding 60000. This combination of performance parameters would not have been possible without the developments presented in this chapter.

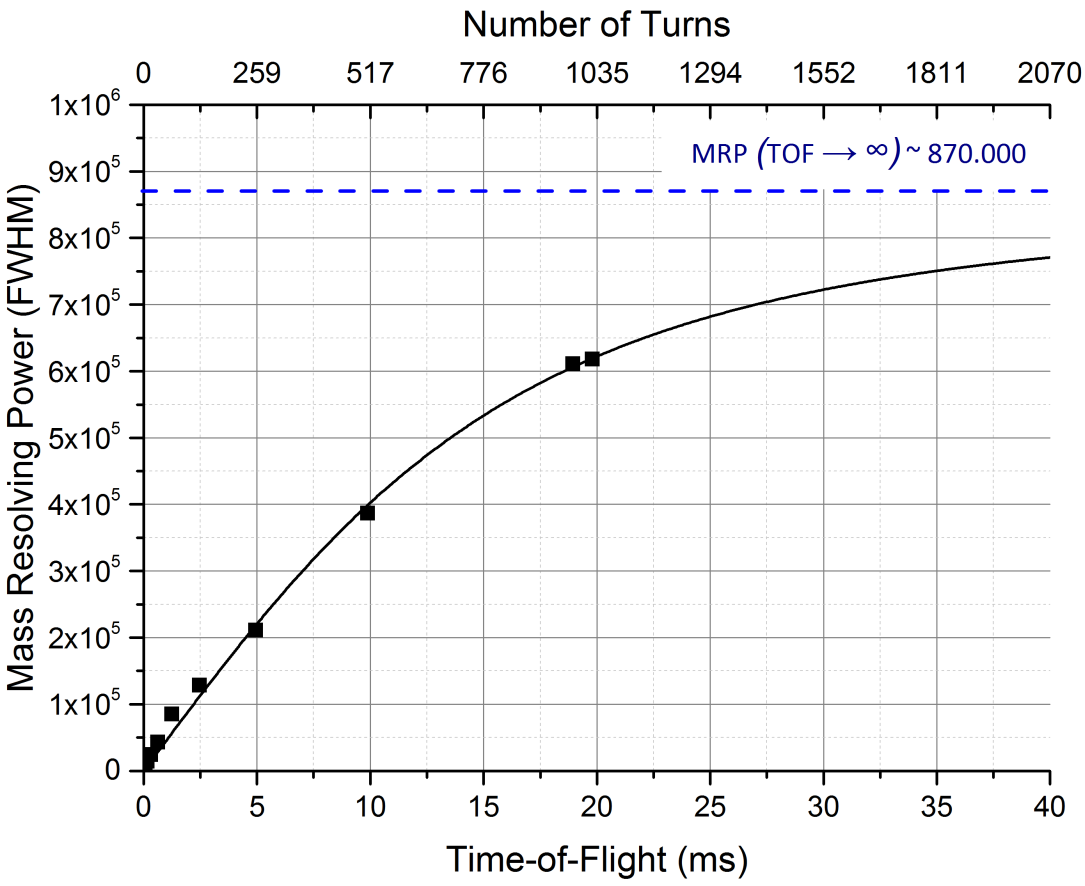

Figure 2.11: Mass resolving power vs. TOF and turn number for $^{39}K^{+1}$ ions at 1300 eV kinetic energy and 50 Hz repetition rate. In black squares the measured data is shown. The black line represents the fit of the data with Eq. 2.1.

2.3.2.2 Improved System Stability and Reliability

The drifts over time of the time-of-flight (TOF) are mainly depending on the mechanical and electronic stability of the analyzer, where the ions spend most of the time for the spatial separation. If the drift of the TOF happens in the low frequency regime, < 0.1 Hz (minutes scale), it can be corrected with a reference ion whose mass is well known. From the electronics perspective, drifts on the TOF will occur due to changes of the potentials applied to the analyzer electrodes. These changes are caused by temperature changes or low frequency instabilities of the power supplies. The drifts due to the thermal expansion of the electrodes from the analyzer result in a change of the flight length for each turn. If the relative changes are large (10^{-4}), the aberrations of the analyzer may change and as a consequence the peak shape of the TOF spectrum. Typical slow changes in the room temperature of $\pm$ 1°C, will change the length of the analyzer by about 15 μm and the voltages of the power supplies by about 100 μV.

The TOF drifts in the high frequency regime (ms scale) are mainly attributed to the noise on the power supplies that provide the potentials to the analyzer, here no cor-

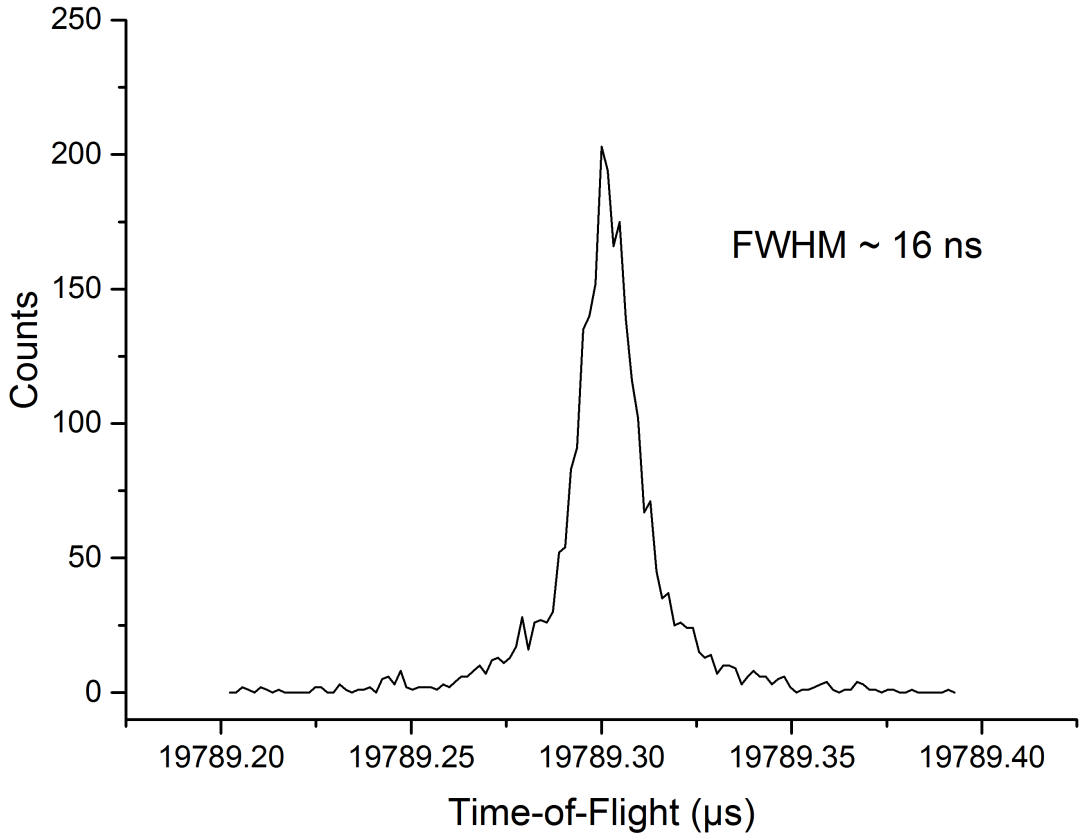

Figure 2.12: Acquired time-of-flight spectrum for $^{39}K^{+1}$ at 1300 eV performing 1024 turns in the analyzer, with an average total time-of-flight of 19789.3 μs, exceeding a resolving power of 600000. The measured peak is formed by the sum of Gaussian functions convoluted with two exponential functions (one on each side), as will be described in the next chapter. The average detected rate is 35 ions per second (less than one ion per cycle) and the total acquisition time 60 seconds.

rection with a reference is possible. In order to improve the stability of the TOF, the potentials applied to the analyzer were supplied from new low-noise and high stable commercial power supplies assembled in a custom made temperature stabilized cabinet with Peltier elements (Telemeter). Also, these potentials were further stabilized with 4th order low-pass RC (100 kΩ and 1μF) filters (see Fig. 2.13) with cut-off frequencies of about 0.2 Hz in order to suppress the high frequency noise.

A TOF stability test was performed with $^{133}Cs^{+1}$ ions with a total time-of-flight of about 15.5 ms with a kinetic energy of 1300 eV. In the Fig. 2.14, the TOF and temperature drifts recorded over more than 2 days are shown. Starting with a "cold" system, an initial warm-up phase of about 5 hours is needed. Then, the TOF drifts with a 24 h period shifted around 5 hours from the day-night room temperature fluctuations. The temperature coefficient of the TOF with room temperature changes after the warm up phase is 8 ppm/°C. The changes of the temperature inside the cabinet with the power supplies, which are most sensitive to the TOF, are negligible. In [Dickel, 2010],

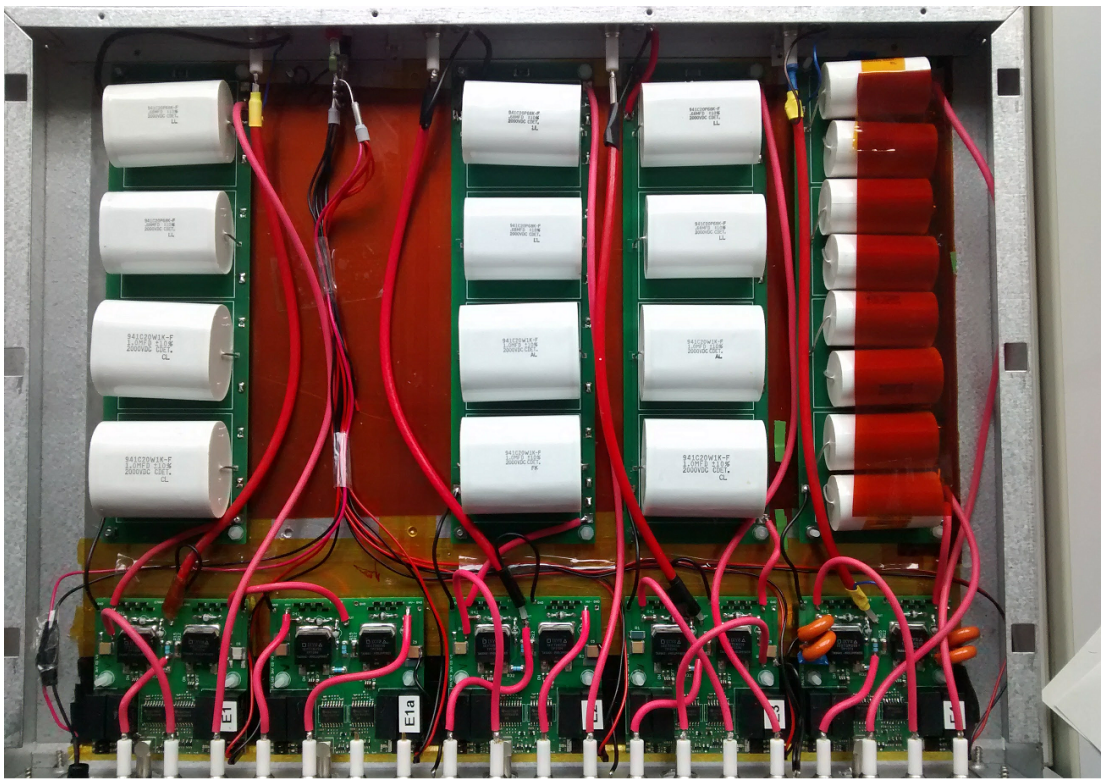

Figure 2.13: Photograph of the stabilization box installed for the input and output mirror (4 electrodes each), including the 4th order RC filters on the top, to suppress the noise with frequencies higher than 0.2 Hz, and the custom developed pulsers in the bottom, for pulsing the potentials of the electrodes. See Appendix A.1 for more information about the pulsers.

a small delay (minutes) between the change of temperature and TOF was observed, with a temperature coefficient of about 20 ppm/°C. This was caused by the introduction of an extra temperature coefficient to the potentials applied to the mirror electrodes by the previous voltage stabilization solution. With the current developments, the slow TOF drifts are governed by the thermal expansion of the analyzer, made out of standard stainless steel with a thermal expansion coefficient of 12 ppm/°C. This can be easily corrected by the time resolved calibration. The use of materials with low coefficient of thermal expansion (< 1 ppm/°C) such as INVAR, has demonstrated to be effective in reducing the temperature drifts of the TOF down to 0.3 ppm/°C [Dickel, 2010, Lang, 2016].

2.3.2.3 Cleanliness of Buffer Gas

In Fig. 2.15 a vacuum diagram of the MR-TOF-MS, including pumps, gauges and gas lines, is presented.

The buffer gas is directly fed inside the encapsulated RFQs of the MR-TOF-MS for cooling the ions in the different traps. Helium is used as a buffer gas because it is the

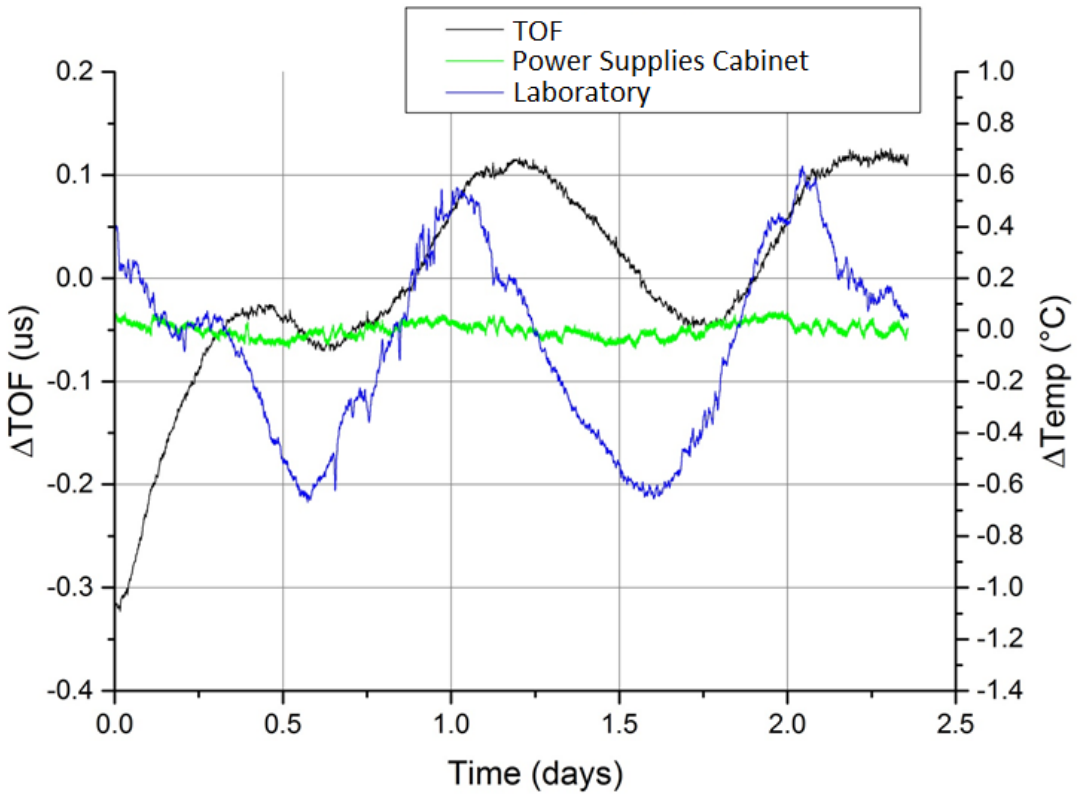

Figure 2.14: Black: TOF deviation for $^{133}Cs^{+1}$ with a total TOF of 15.328 ms (left y-axis). The initial warm up phase shifts the TOF about 300 ns, corresponding to a relative mass-to-charge change of $2{\cdot}10^{-5}$. Blue: room temperature deviation where the MR-TOF-MS was running at GSI (right y-axis). Green: temperature deviation of the power supplies supplying the potential to the most TOF-sensitive mirror electrodes of the analyzer (right y-axis).

element with the highest first ionization potential (IP = 24.59 eV) and has low chemical reactivity, transporting other species of ions without neutralization or formation of molecules. The initially purity of the helium used is of 99.9999% (6.0). Due to the long gas lines (some meters) needed to transport the helium from the tank to the system, the purity gets reduced substantially. The value obtained after testing the purity with a commercial MicroVision residual gas analyzer (RGA) (www.mksinst.com) was about 99.9%. The problem of having contaminants (typically hydrogen, water, oxygen, nitrogen, hydrocarbons...) in the buffer gas arises when the contaminant is highly reactive or has an IP lower than the ion to be transported. When there is an interaction between the ion and the contaminant (neutral), the contaminant will easily transfer an electron to the ion, lowering its charge state or even neutralizing it, making impossible the further transportation by means of electromagnetic fields. Another problem that can occur while cooling the ions to be transported with a buffer gas containing contaminants is the chemical reaction and formation of molecules. There are some elements which are highly reactive, especially with hydrogen, oxygen, hydrocarbons, nitrogen,

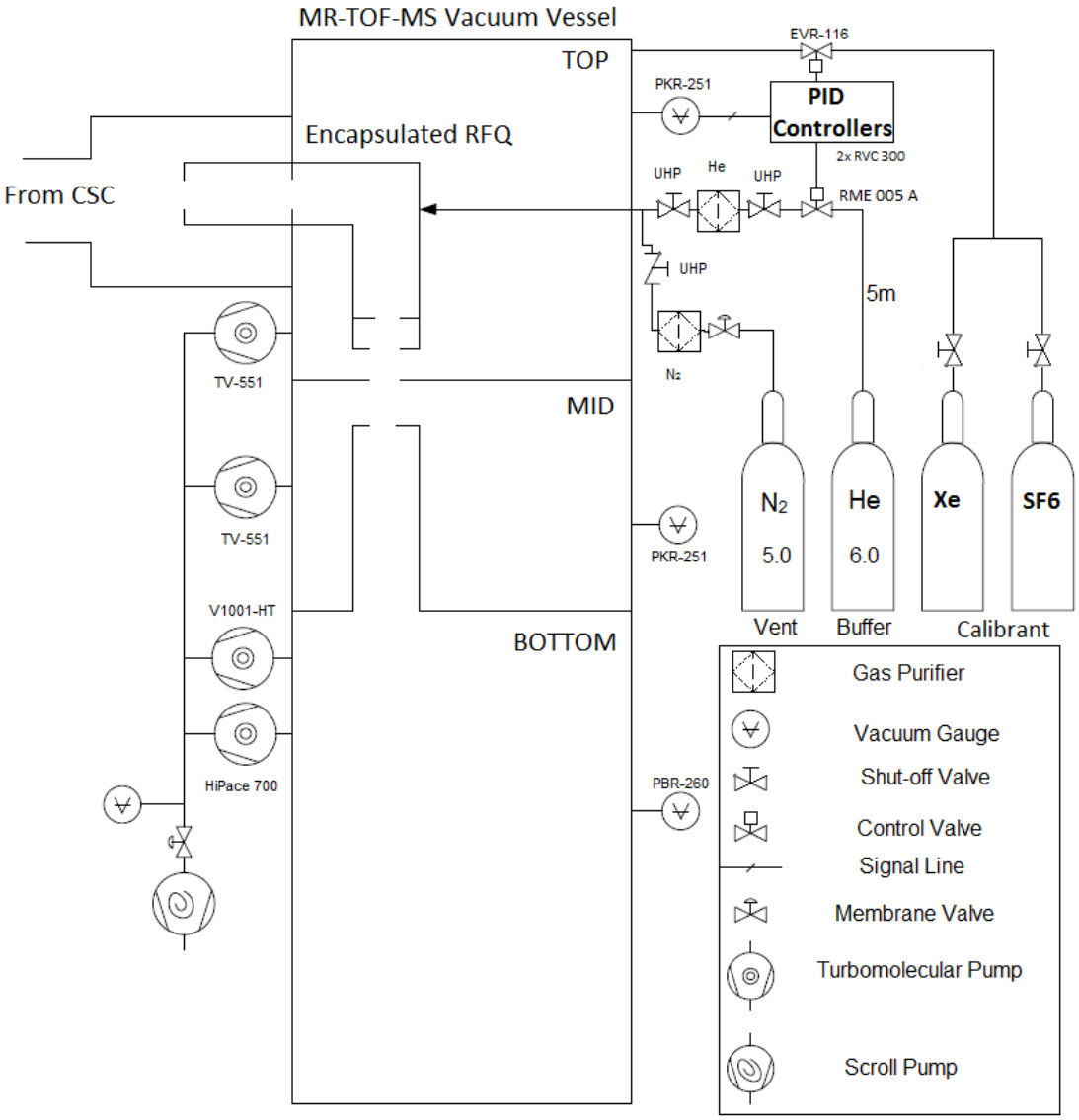

Figure 2.15: Vacuum diagram of the MR-TOF-MS. Purifiers for buffer gas (He) and for venting gas (N_2) were installed. Also normal shut-off valves are avoided and only ultra-high purity (UHP) all-metal valves are installed.

etc. like uranium or thorium [Anicich, 2003]. When combining with the contaminants and forming molecules, the ionization potential will change and could be neutralized. Therefore, a pure buffer gas, where the ions to be transported do not change their charge state nor react with any contamination is needed in the MR-TOF-MS.

In order to increase the purity of the gas, the valves of the buffer gas line and the venting gas line were exchanged by ultra high purity (UHP) all-metal valves (Swagelok 6LVV-DPRS4). Also gas purifiers were installed in both lines: in the buffer gas line, TTE-750-4 and in the venting gas line, AIO-750-4 (Fig. 2.15).

To check the purity of the buffer gas inside the encapsulated RFQs and the trap system before and after the changes, the survival efficiency of the system for krypton (IP = 13.99 eV) ions with different storage times inside the trap system was measured. The

longer the storage time is inside the trap system, the higher the probability of a charge exchange reaction with a contaminant. By measuring how fast the survival efficiency drops with storage time, the cleanliness of the buffer gas employed for cooling can be benchmarked. In order to monitor the efficiency losses of the trap for different storage times, rubidium ions were taken as reference, were neutralization is highly improbable due to the low IP (4.17 eV) and no chemical reactions are expected. Fig. 2.16 shows the efficiency results obtained for different storage times at T1 for krypton and rubidium ions.

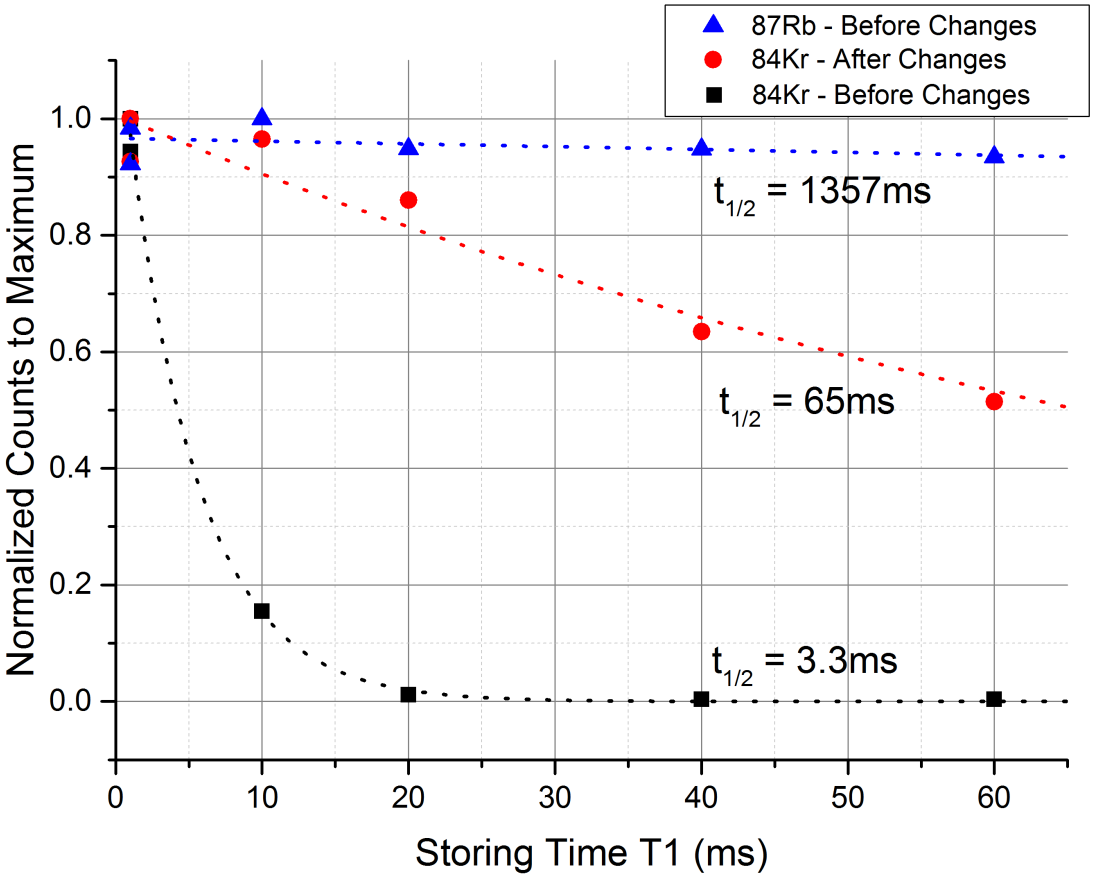

Figure 2.16: Survival fraction of singly charged Rb and Kr ions in T1 as function of the storage time (1 ms, 10 ms, 20 ms, 40 ms and 60 ms) before and after the upgrades in the gas supply system. The dashed curves represent the fitted exponential decay function to the data. The time shown represents the storage times for 50% of survival fraction.

For rubidium, even without changes, one can see the almost constant efficiency for different storage times due to its low IP (4.17 eV) and low reactivity. On the other hand, the krypton survival efficiency for long storage times gets improved dramatically by almost a factor of 20 after the installation of the gas purifiers. If the storage times of all the traps (T0 and T1 and T2) are taken in account, a total storage time of about 15 ms is obtained (> 80% efficiency for krypton), pointing that the cleanliness of the buffer gas is a key point when working with high IP or highly reactive elements.

After the developments described in this section (increase in kinetic energy and repetition rate, improved stability and reliability and improvement of the cleanliness of the gas), the MR-TOF-MS has the performance parameters presented in Tab. 2.2. With this current performance parameters, mass measurements of exotic nuclei with a 10^{-7} level of relative uncertainty are possible with fewer counts (few tens), faster (20 ms cycle time) and for a wide variety of elements. Also the resolution of short-lived isomers with excitation energies of few hundreds of keV is enabled.

Parameter	**Performance**	**Enabling Development**
Kinetic Energy	1300 eV	New P. Lift Electronics
Repetition Rate	> 1000 Hz	New P. Lift Electronics
Temp. Coefficient of TOF	8 ppm/°C	Temp. Stabi. and New Stabi. Box
Max Resolving Power	600000 in 20 ms of TOF	New HV Cabinet + Stabilization
Buffer Gas Cleanliness	Ar, Kr, Xe, Rn and +2 Ions	Gas Purifiers and UHP valves

Table 2.2: Performance characteristics of the MR-TOF-MS after the upgrades presented in this section. The temperature coefficient is reduced and only long term drifts (hours) affect the TOF.

In the next chapter, results of direct mass measurements of short-lived nuclei, performed with two different MR-TOF-MS, where all or some of the developments described in this chapter were implemented, will be presented.

3 Experiments and Results

The improvements presented in the previous chapter were developed in order to reach higher performance with the MR-TOF-MS, enabling mass measurements of a wide variety of short-lived nuclei (including heavy nuclei with $A \geq 200$) with relative uncertainties in the 10^{-7} level in less than 20 ms. This uncertainty levels were so far only reached by Penning traps with lighter nuclei or by much larger and complicated accelerator structures such as storage rings. The results presented in this chapter were obtained in three experiments at GSI (GSI Helmholtzzentrum für Schwerionenforschung GmbH, Germany), in 2014 and 2016, with the FRS-Ion Catcher, where mass measurements of ^{238}U fission fragments and ^{238}U and ^{124}Xe projectile fragments were performed. The results include in addition the identification of several uranium charge states, uranium molecules and fission fragments extracted from the stopping cell via high accuracy mass measurements. The fourth part of the results was obtained in an experiment at TRIUMF (Canada's National Laboratory for Particle and Nuclear Physics, Canada), in 2017, with the MR-TOF-MS of TITAN (TRIUMF′S Ion Trap for Atomic and Nuclear Science) developed and built in the Justus-Liebig University in Gießen [Jesch et al., 2015, Jesch, 2016], where first direct mass measurements of neutron-rich gallium isotopes were performed. All improvements were developed and implemented first at the FRS-Ion Catcher and then partially implemented in the MR-TOF-MS of TITAN, Canada, and in a mobile MR-TOF-MS [Lang, 2016, Lippert, 2016] at the Justus-Liebig University in Gießen.

Both systems have the data acquisition system in common, based on a commercial time-to-digital converter (TDC), model Ortec-9353, which digitizes the time-of-flight between the ejection of the ions from the injection trap and the arrival at the detector. The data evaluation procedure and tools used to calculate the mass values and uncertainties from the TOF spectra acquired in the experiments at GSI and TRIUMF were different. The data evaluation from the first experiments performed at the FRS-Ion Catcher, during 2014 and 2016, was developed to quantify and understand all the individual contributions to the total mass uncertainty. An overview including the latest improvements of this data evaluation procedure will be given. The knowledge of the individual contributions to the total uncertainty allows decreasing some of the individual errors or even eliminate them in future experiments, achieving the highest possible precision. Using this acquired knowledge during the development of the evaluation

procedure for the experiments at GSI, and due to the special features of the data acquired during the experiment at TITAN, a simplified version of the data evaluation procedure was possible. This procedure will be introduced as well.

3.1 Experiments in a Hybrid Facility

The production mechanism of exotic nuclei based on the hybrid method was already presented in Fig. 1.9. The hybrid facility, formed by the FRS and the FRS-Ion Catcher has been presented in the last chapter and a sketch can be seen in Fig. 2.2 and Fig. 2.3. In Fig. 3.1, the FRS-Ion Catcher at the final focal plane of the FRS during an experiment is shown.

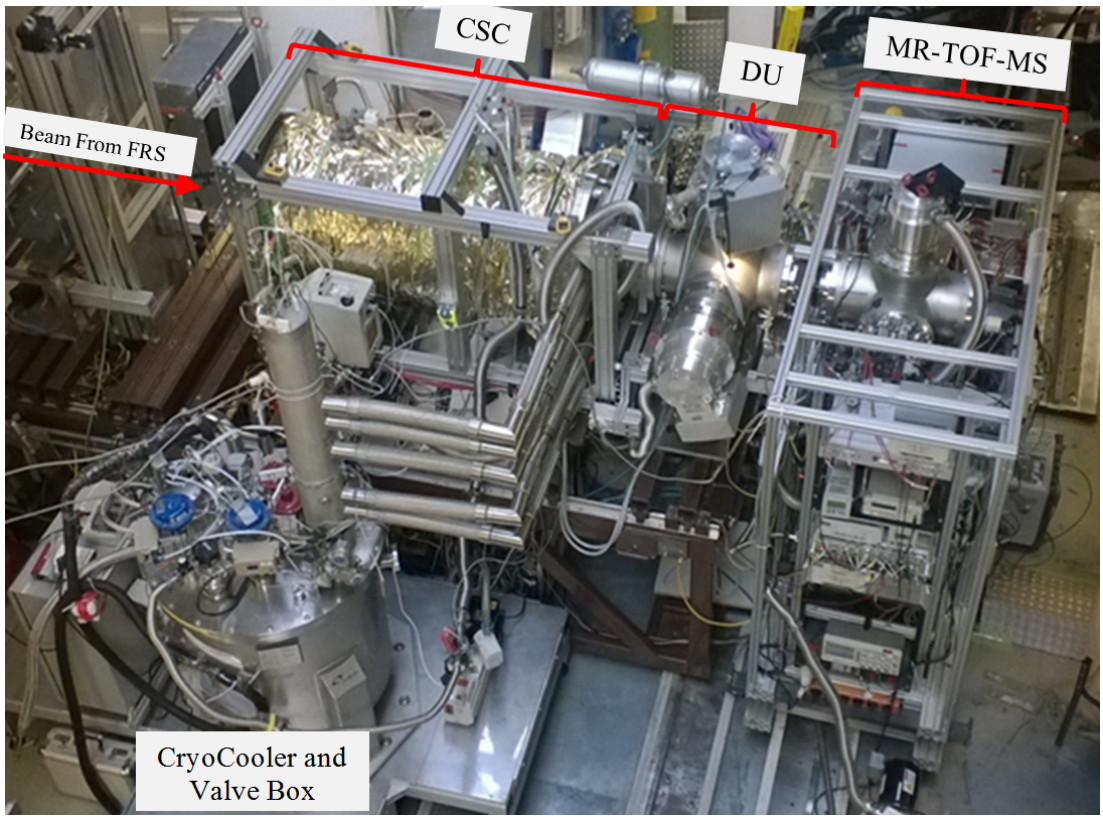

Figure 3.1: Photograph of the FRS-Ion Catcher system at the final focal plane of the FRS during the experiment in 2014; in 2016, a similar arrangement was used. On the left the beam is delivered from the FRS and injected into the CSC. The cryogenic system (including the valve box) is used to cool down the stopping gas and the inner chamber of the CSC to cryogenic temperatures. The FRS-Ion Catcher fits in less than 4 m of beamline.

3.1.1 Data Evaluation

The TOF of the different nuclei is recorded using MAc software [Bergmann, 2018a]. This software is used as well for preparing the data (data treatment, formatting, exporting, etc.) for the final analysis and extraction of the mass-to-charge values and uncertainties of the nuclei. The final analysis is carried out with a software developed in *R* [R Core Team, 2017], a programming language for statistical computing. It is based on the analysis procedure described in [Ebert, 2016] and contains additional features and improvements. The data evaluation procedure of the two experiments carried out at the FRS-Ion Catcher at GSI comprises both parts, the preparation of the data in MAc and the analysis with *R*. In Fig. 3.2, a diagram of the data evaluation procedure is shown.

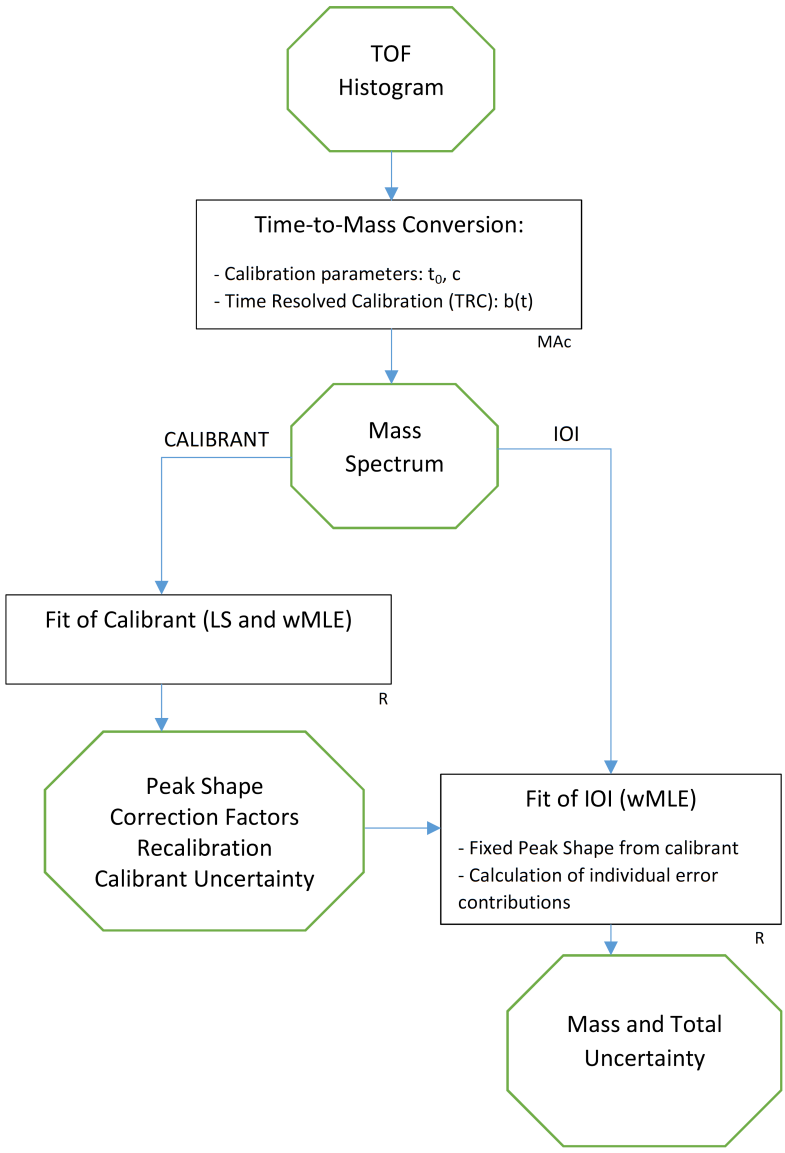

Figure 3.2: Simplified diagram of the data evaluation procedure, presenting the main steps to be followed. The description of the steps can be found in the text.

In the following, an extensive description of the different steps followed in the data evaluation process, taking special attention to the calculation of the final mass value and the different uncertainty contributions, is given. This includes the special treatment needed in the case of close lying peaks.

1. The data evaluation starts with the time-of-flight (TOF) data recorded in MAc, containing a histogram of the TOF of the different nuclei summed over a certain number of cycles of the spectrometer (typically 50 summed spectra, therefore at 50 Hz repetition rate, 1 summed spectrum per second is recorded). In this data, the TOF of a certain mass-to-charge ratio can have fluctuations, mainly due to two reasons: changes in the potentials applied to the mirror electrodes in the analyzer and thermal expansion of the analyzer as presented in the previous chapter. One of the nuclei included in the spectra is a well-known mass (calibration mass) and can be used as a reference to correct the slow TOF fluctuations.

2. The formula that relates the TOF of an ion with its mass is given in Eq. 1.9. The parameters c, t_0 and b have to be obtained from calibrant masses in MAc in order to measure the mass-to-charge ratio of the ion of interest (IOI). The parameter t_0 and c, are first calculated using the time-of-flight of at least two calibrant masses that were measured in pass-through (zero turns). Depending on the calibrants available in the spectrum of the IOI, there are two options: (i) if in the spectrum two calibrant masses perform different number of turns, c and b can be calculated from those references. In this case the new c will replace the one calculated with the calibrants of the spectrum with no turns. With this new c, lower uncertainties in the mass-to-charge ratio of the IOI will be achieved when no calibrant is available with the same turn number than the IOI. (ii) If there are only calibrants available at a given number of turns (same or different than the ion of interest), only b can be calculated and t_0 and c, are taken from the calculation with the calibrants performing no turns. To correct the drifts of the TOF, as mentioned before, the parameters t_0 and c are kept fixed and one calibrant is used to calculate the time dependence of b, obtaining the time-resolved calibration (TRC). This parameter b will vary in time such that the fluctuations in the TOF from the calibrant are converted to the same mass-to-charge ratio. High frequency fluctuations on the TOF caused by electric fields (kHz range and higher), are averaged by the ions, which interact with the fields of the mirrors at a frequency of few tens of kHz. In the case of fluctuations at the low frequency range (Hz) due to changes in the electric fields, the stabilization box (Fig. 2.13) attenuates this fluctuation. For even slower drifts on the TOF (mHz range and lower frequency) caused by voltage fluctuations of the power supplies or thermal expansion of the analyzer, the TRC is the correction method in charge of the minimization of the fluctuations in this frequency range. In order to perform the TRC (assuming that

t_0 and c have already been calculated), firstly the TOF of the calibrant during the measurement of the IOI has to be obtained. A TOF window is defined where the software will search for the calibrant peak, determining the TOF of the calibrant using the interpolated median method [Wikipedia, 2018a] in the given window. For the next calibration points, the window center is moved to the last TOF of the calibrant obtained, assuring that the window can be smaller than the TOF fluctuation of the calibrant. In the calculation of the calibration points, a compromise between the TOF accuracy of each calibration point and the distance between the calibration points needs to be taken. Each calibration point needs enough events to calculate b accurate enough to not add extra error to the final mass value. Additionally, the TOF of the calibrant needs to be calculated often enough to correct the fluctuations in the mHz range. For obtaining the TRC, i.e. a continuous b, a linear interpolation is done between the calculated calibration points. For obtaining the final mass spectrum to be later analyzed, the TRC is applied to the nuclei present in the spectrum. If the calibrant and the other nuclei present in the spectrum experience the same electric fields, the time resolved calibration will correct the drifts. If this is not the case, an extra mass uncertainty will be added to the final mass value of the ion of interest.

3. The next step is to extract the time-resolved calibrated data from MAc to obtain the mass-to-charge ratio of the IOI with *R*. The original data was a TOF histogram with certain fixed bin size, where the events were uniformly distributed in each bin. After the conversion to mass, the bin size and position is different for each summed spectrum. Therefore, the data will not be extracted from MAc as a histogram with fixed bin size, but as a list mode data with each event randomized uniformly on its bin. With this step, the preparation of the data in MAc for the analysis is finished and the unbinned data containing the events of the calibrant and the other IOI in spectrum will be used as an input for the analysis in *R*.

4. The first step in *R*, is the peak shape determination of the acquired data. This is done by fiting an analytical formula to a peak with high number of events, obtained simultaneously with the IOI. Normally, this peak is the calibrant which was used for the TRC. The analytical formula describing the peaks obtained with the MR-TOF-MS is the Hyper-EMG [Purushothaman et al., 2017] function, which consists in a sum of a given number of left (L) and right (R) exponentially modified Gaussian (EMG) functions, i.e. Gaussian convoluted with an exponential, noted as Hyper-EMG (L,R) in the following (see [Purushothaman et al., 2017] for the mathematical formulation). For the data in the thesis, a maximum of two EMGs of each type (left and right) will be considered. The parameters to be calculated for a Hyper-EMG (L,R) are:

- Parameters for the Gaussian function:
  a) σ: standard deviation.
  b) μ: centroid.
- Parameters for the exponentials on the left:
  a) τ_{L_1}: growth constant of the first left exponential.
  b) τ_{L_2}: growth constant of the second left exponential.
  c) η_L: weight of the areas of the first η_L and second $1-\eta_L$ left exponentials. Needed in case of L $>$ 1.
- Parameters for the exponentials on the right:
  a) τ_{R_1}: decay constant of the first right exponential.
  b) τ_{R_2}: decay constant of the second right exponential.
  c) η_R: weight of the areas of the first η_R and second $1-\eta_R$ right exponentials. Needed in case of R $>$ 1.
- A: total area of the Hyper-EMG function.
- θ: weight of the areas of the left (θ) and right ($1-\theta$) EMGs in case L $\neq$ 0, and R $\neq$ 0.

In some cases, a relative small Gaussian peak (5-10% of the area of the main peak) has to be added in order to get a more accurate definition of the peak shape. This side peak appears due to ion optical aberrations in the system and its strength depends on the tuning of the analyzer. The extra parameters to be added in case of using an extra Gaussian side peak are: sigma (can be different than the one from the main peak), relative area from the main peak and distance between main peak and side peak. Also, a uniformly distributed background can be defined to be taken in account in the fits. The definition of the peak shape with this level of accuracy is of special interest if evaluating data which contains overlapping peaks and the area and mass values of the overlapping peaks have to be determined with high accuracy [Purushothaman et al., 2017]. The first step is to determine the number of exponentials that are needed on each side in order to describe the peak shape of the data and if the analytical formula needs to include the Gaussian side peak. After a first eye-estimate of the number of exponentials and the existence of the Gaussian side peak, a least square (LS) minimization between the data and an initial estimate of the peak shape parameters, using the Levenberg-Marquardt iteration algorithm, is performed to obtain the peak shape

parameters and its uncertainties with the chosen number of exponentials. The mass window analyzed to determine the peak shape, will contain in the limits an average of one event in the histogram. An example of the peak determination of a mass spectrum obtained with the MR-TOF-MS from the FRS-Ion Catcher, using in this case a Hyper-EMG (1,2) and a Gaussian for comparison, is presented in Fig. 3.3.

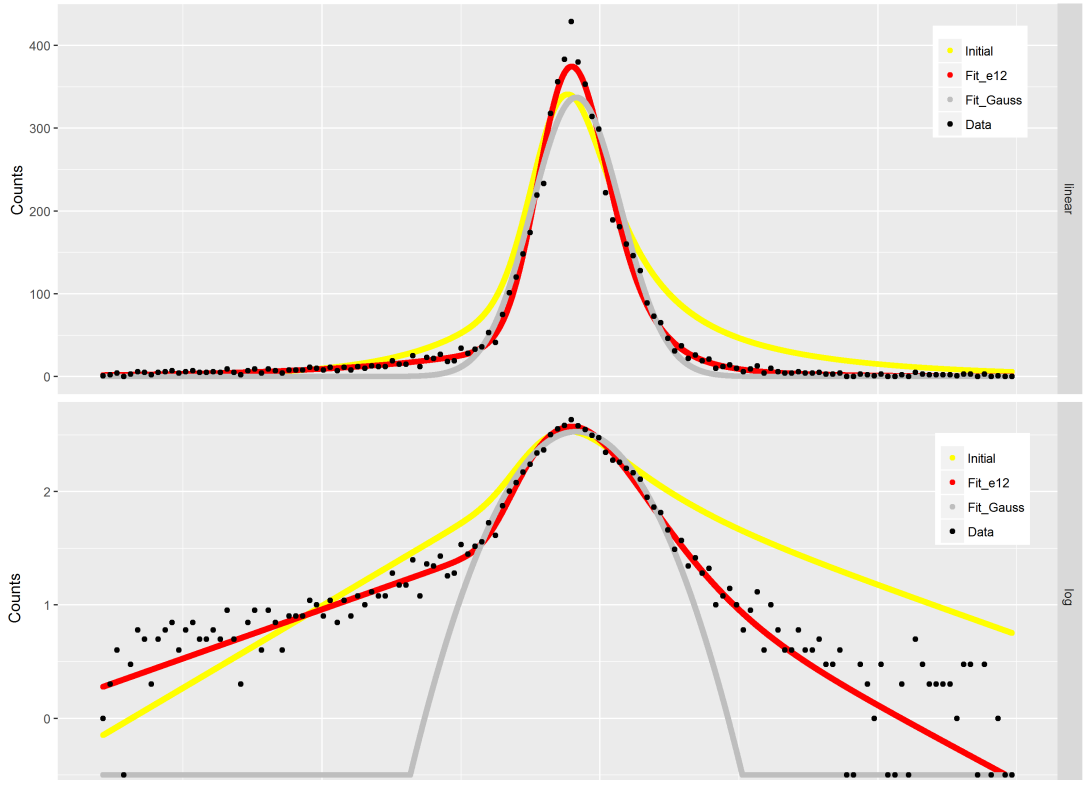

Figure 3.3: Initial estimate (yellow) and fitted functions with the LS method: Hyper-EMG(1,2) (red) and pure Gaussian (grey). Upper part in linear scale and lower in logarithmic scale. The tails are clearly not properly described by the Gaussian function. In black dots, the binned original data, which corresponds to the calibrant of the spectrum shown in Fig. 3.17.

At this point, a value with the uncertainty for all the defined parameters of the peak shape is obtained, and the square root of the mean square residuals (residual standard error) of the fit is calculated. If the peak shape is not well described (too few exponentials, side peak existence wrongly chosen, initial Hyper-EMG parameters too far from reality, etc.), the residual standard error of the fit will be high, meaning that the peak shape model fitted does not describe the data of the peak with enough accuracy. In this case, the number of exponentials, the possible existence of a side peak and the initial parameters have to be reconsidered. On the other hand, if the peak shape model to be fitted contains too many exponentials or the side peak is too weak in the data considered, the uncertainty of the parameters will be higher than the parameter itself. In this case a simpler function, removing those parameters with higher uncertainties

than the parameter itself needs to be chosen. After getting a residual standard error of the fit, which hints that the data is well described, peak shape parameters with uncertainties not larger than the parameter itself and a positive visual check, Kolmogorov–Smirnov (KS) tests (comparison of the cumulative distribution functions) are performed between the calculated analytical model and the data, obtaining another parameter ($0 \leq$ p-value ≤ 1), which will indicate if the events from the data can be described by the analytical probability distribution. If this peak contains much higher number of events than the IOI, KS tests between the analytical formula obtained and samples obtained from part of the data containing similar number of events than the IOI are performed, validating or invalidating that the peak shape is well enough described for the number of events contained in the IOI.

5. The calibrant data is fitted with peak shape function determined in the previous point using a weighted maximum likelihood estimation (wMLE), where the only free parameter is the centroid. The used weighting function is the natural logarithmic of the function used as peak shape. The weighting is perform to minimize the influence of outliers to the determined centroid [Ebert, 2016].

6. The parameters describing the peak shape, including its uncertainties, and the determined mass of the calibrant with a wMLE fit, were obtained in the last two points. The uncertainties of the different parameters contribute independently (assumed for simplification) to the uncertainty of the mass value (centroid, μ). Each parameter of the model is changed by its uncertainty, keeping the rest as calculated in the previous point, and a wMLE, where the only free parameter is the centroid μ, is performed with the calibrant data. The wMLE method is implemented using a non-linear minimization of the negative logarithmic (natural logarithmic in this case) of the weighted-likelihood function. In this case the weights of the data are chosen to be the analytical formula itself (see section 4.1.4 of [Ebert, 2016]). The value obtained fitting the data with the original peak shape parameters is divided by each mass values obtained from the fit of the data changing each of the peak shape model parameters by its uncertainty, plus the uncertainty and minus the uncertainty, while the others are fixed. The values obtained are called correction factors and two correction factors for each parameter are obtained. This correction factors will be used in the fit of the IOI to obtain the uncertainty of the relative position between the calibrant and the IOI due to a not correctly determined peak shape (peak shape error). The centroid of the calibrant and the IOI have to be determined with the same method. Since in MAc the centroid of the peaks is determined via a weighted mean, a precision calibration factor (R) is calculated by fitting the calibrant data with the same method that will be used for the IOI, the wMLE method.

7. Up to now, only the data corresponding to the calibrant peak has been treated. After the calculation of the peak shape model and the correction factors, the next step is to calculate the mass and uncertainty of the IOI. Some of the peak shape parameters calculated from the calibrant (σ and the τ) have to be first scaled. The scaling factor of the parameters can be a simple scaling factor, based in the mass-to-charge ratios of the calibrant and the IOI, or a more elaborated scaling taking in account what is the ion optical effect of the scaling of each parameter. For the second case, the scaling factor (S) of σ and τ will be based on Eq. 3.1, where $\frac{m}{q}_{IOI}$ and $\frac{m}{q}_{CAL}$ are the mass-to-charge ratio of the ion of interest and the calibrant and Rm_{IOI} and Rm_{CAL} are the resolving power for the ion of interest and calibrant ion respectively calculated as Eq. 2.1. For scaling the τ, the resolving powers (Rm_{IOI} and Rm_{CAL}) are calculated with zero turn-around time because this contribution to the peak shape is attributed to optical aberrations which do not depend on the turn around time.

$$S = \frac{\left(\frac{m}{q}\right)_{IOI}}{\left(\frac{m}{q}\right)_{CAL}} \cdot \frac{Rm_{CAL}}{Rm_{IOI}} \tag{3.1}$$

$$R_m = \frac{t_{IT} + \frac{t_{TFS}}{N_{IT}}}{2 \cdot \sqrt{(\frac{q_{REF}}{q}) \cdot (\frac{t_a}{N_{IT}})^2 + (\frac{\Delta t_{TFS}}{N_{IT}})^2 + (\Delta t_{IT})^2}} \tag{3.2}$$

Where q_{REF} is the charge state of the reference used for calculating the rest of the parameters, q is the charge state of the IOI or the calibrant, t_{IT} is the time-of-flight for one turn in the analyzer, t_{TFS} is the time-of-flight from the injection trap to the detector without any isochronous reflection in the analyzer, Δt_{TFS} is the time spread due to aberrations for no turns, t_a is the turn-around time, N_{IT} is the number of isochronous turns in the analyzer and Δt_{IT} is the time-of-flight spread added on each turn due to the optical aberrations of the analyzer.

With the peak shape parameters scaled and fixed, only the center of the Hyper-EMG function is left as a free parameter. A wMLE is performed with the analytical formula of the peak shape model and the data of the ion of interest to obtain its fitted mass value, $m_{IOI-wMLE}$, which will be used for the calculation of the final mass value.

3.1.1.1 Final Mass Value and Uncertainty Contributions

To obtain the final mass value and the uncertainty, some corrections have to be applied to the fitted mass value ($m_{IOI-wMLE}$) and the calculation of the different uncertainties

has to be performed. In the following, a brief description of the corrections applied to obtain the final mass and the different contributions to the final mass uncertainty will be given.

- Mass Range Selector (MRS) Shift.

The MRS electrodes are located in the middle of the drift tube of the analyzer. Pulsing the MRS electrodes in order to isolate a certain mass range, causes for each switching of the MRS a small change in the voltages applied to some electrodes of the analyzer, thus the ions shift their TOF depending on the number of cycles applied to the MRS. This error will be non-existing if the induced voltages are experienced equally by the calibrant and the IOI, but sometimes, the MRS is switched off to have calibrant ions in the spectrum while the IOI data is acquired with MRS on in order to have a clean and unambiguous mass spectrum. Then, the shift obtained by pulsing the MRS electrodes will be different for the ion of interest ($MRS_{ShiftIOI}$) and calibrant ($MRS_{ShiftCal}$). This shift is calculated using Fig. 3.4 and the information about how many isolation cycles were done for calibrant and IOI.

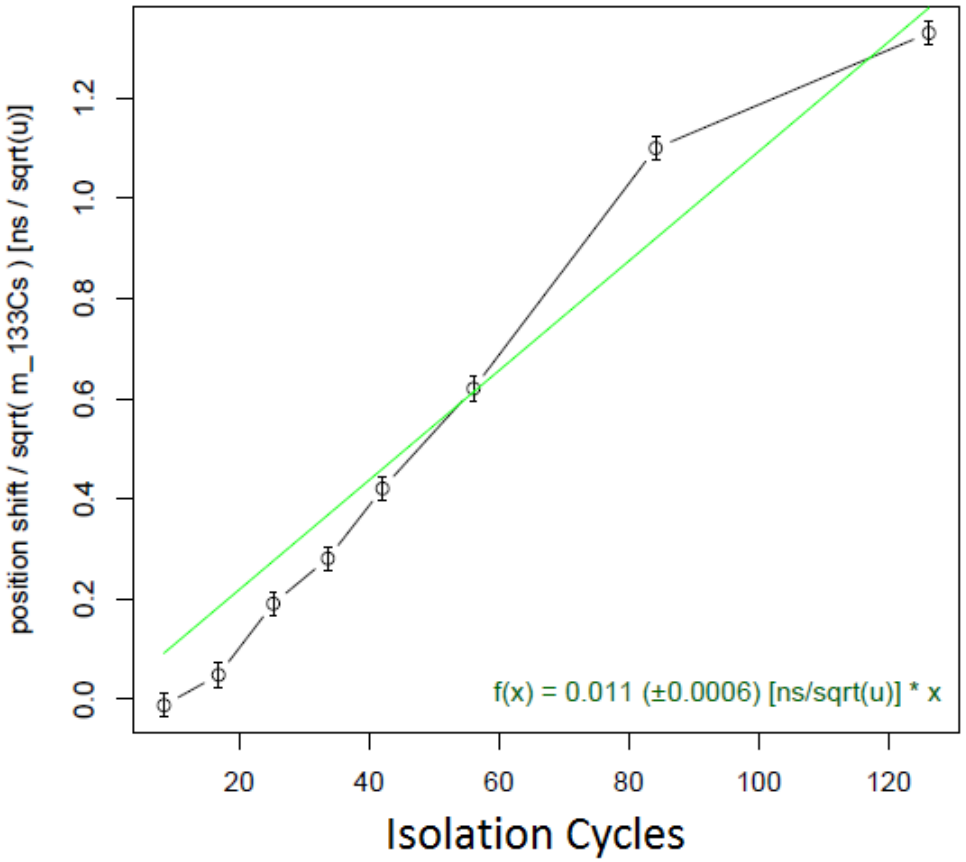

Figure 3.4: TOF shift contribution due to the effect of pulsing the MRS for a certain number of isolation cycles. The data was measured with ^{133}Cs ions [Bergmann, 2018b] and fitted with a linear function (green).

In the measurement of a nuclei (^{123}Xe) during an experiment in 2016, the effect of the MRS shift was maximized due to the high number of isolation cycles (half of the total turns) which were only experienced by the IOI and not by the calibrant, and the short flight time (about 4.5 ms) of the ions. Without the shift correction included, the mass of ^{123}Xe was more than 3 σ. After the MRS shift correction, calculated as explained before and the extra uncertainty contribution due to the MRS shift (see next point), the mass was corrected to about one σ.

- Precision Calibration.

To obtain the final mass value of the IOI from the fitted mass value $m_{IOI-wMLE}$, the MRS shift of the IOI ($MRS_{ShiftIOI}$) and the precision calibration factor (R), defined in Eq. 3.4, will be applied as described in Eq. 3.3:

$$m_{FINAL\_IOI} = R \cdot (m_{IOI-wMLE} - MRS_{ShiftIOI}) \tag{3.3}$$

$$R = \frac{m_{CAL-LIT}}{m_{CAL-wMLE} - MRS_{ShiftCal}} \tag{3.4}$$

Where $m_{CAL-LIT}$ is the literature mass [Huang et al., 2017], $m_{CAL-wMLE}$ is the mass of the calibrant obtained by the wMLE fit with the original peak shape parameters and the $MRS_{ShiftCal}$ is the shift of the mass-to-charge ratio due to the effect of the mass range selector (MRS) of the calibrant. Its relative uncertainty can be written as:

$$\frac{\Delta_R}{R} = \sqrt{(\frac{\Delta m_{CAL-LIT}}{m_{CAL-LIT}})^2 + (\frac{\Delta m_{CAL-wMLE}}{m_{CAL-wMLE}})^2} \tag{3.5}$$

Where $\Delta m_{CAL-LIT}$ is the AME16 uncertainty for the calibrant mass and $\Delta m_{CAL-wMLE}$ the statistical uncertainty of the fitted calibrant.

In the following, the possible contributions to the mass uncertainty will be described.

- Peak Shape Error:

This contribution takes into account that the peak shape determined from the calibrant peak can differ from the real peak shape of the IOI after applying the scaling factor. The peak shape error is calculated by fitting the IOI, where on each fit, a peak shape parameter is changed by its uncertainty (plus and minus). The results of the different fits are then corrected by the correction factors, previously calculated, and the mass obtained with the original peak shape parameters is subtracted. The larger of the two

(plus/minus) values for each parameter is quadratically added to obtain the total peak shape error.

- Statistical Error:

This error contribution, accounts for the standard error of the mean. In samples following a normal distribution, it is calculated as $\frac{\sigma}{\sqrt{N}}$, with σ the standard deviation of the normal distribution and N the number of samples. For the wMLE fit with a Hyper-EMG, an empirical approach is followed. From the peak shape that was employed to fit the data, independent random samples following the probability distribution obtained from the peak shape, with the same mass value and the same number of events as the calibrant or IOI, are produced. Then, a fit to the samples with the same peak shape is performed. The standard deviation of the mass values obtained for the different random samples is calculated and used as statistical error for the mass of the calibrant or the IOI. This approach is followed with single and double peak fits.

- Non-Ideal Ejection (NIE) Error:

The pulsed voltages applied to the analyzer electrodes need some time (some μs) to stabilize after changing the state. In the case of switching the output mirror to an open state to let the ions escape from the analyzer and travel to the detector, ions with different mass-to-charge ratios which are spatially separated can experience different fields. The effect of this error depends mainly on the electronics that pulse the voltages of the analyzer electrodes and the spatial separation of the ions. For the calculation of this error contribution, an empirical approach is followed before or after the experiment. The deviation of the time-of-flight is measured depending on the delay applied to open the output mirror in the last turn. Since this effect occurs only during ejection from the analyzer, its absolute value is constant and independent on the number of turns. Therefore, to maximize the TOF stability and enhance the NIE effect, low number of turns are used. An example of the data taken with ^{133}Cs as calibrant for the calculation of this error for 2016 data is shown in Fig. 3.5. Here, the calibrant performs two turns. If the opening delay is such that the ions are at the beginning (lower delays) or at the end (higher delays) of the second turn, the ions will experience a strong disturbing field as shown in the upper panel of Fig. 3.5. The bottom panel is a zoom of the marked green area from the top panel, where the ions might be affected by instabilities in the output mirror after being open.

The instabilities of the total time-of-flight for the calibrant, Δt_{NIE}, will be calculated as the standard deviation of the time-of-flight, and the error contribution will be calculated as Eq. 3.6.

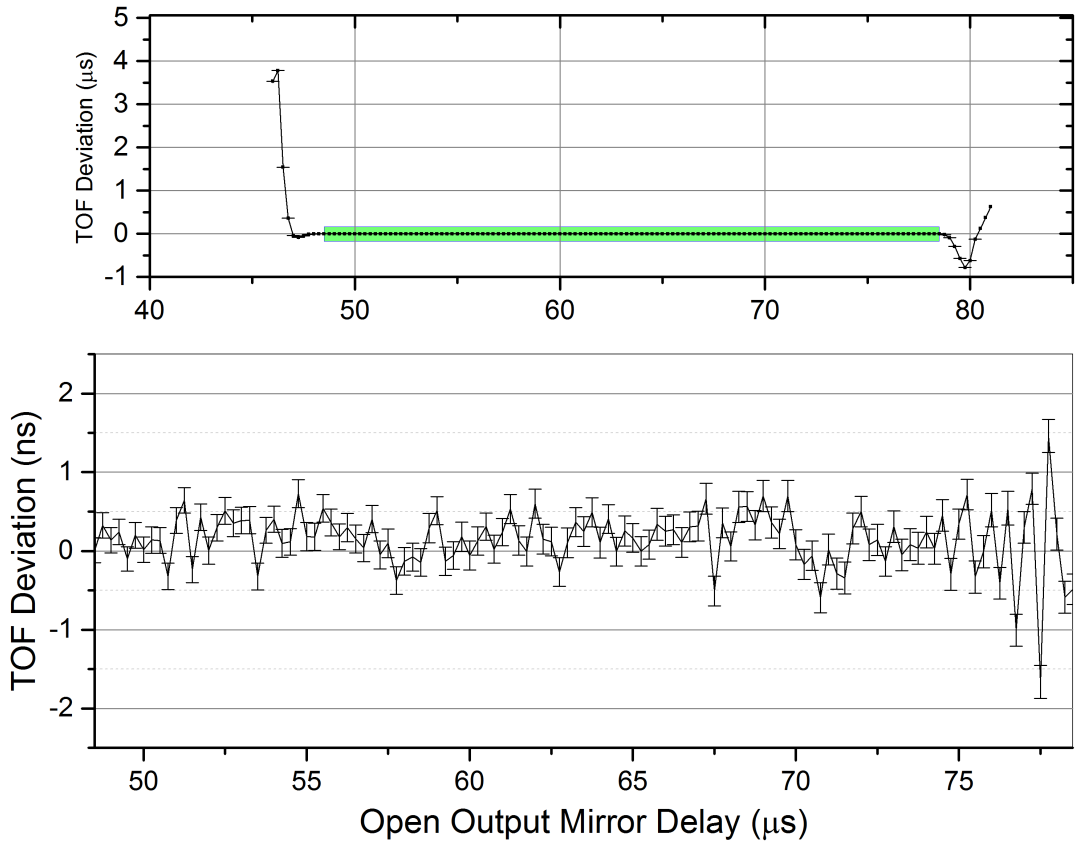

Figure 3.5: Deviation on the time-of-flight for ^{133}Cs ions. The ions perform two turns. The opening delay of the mirror is scanned for the second turn. In the extremes of the delay, a strong deviation can be seen because the mirror electrodes are pulsed while the ions are near the output mirror when starting (left side) or finishing the second turn (right side). The zoom corresponds to the marked green region. The non-ideal ejection error refers to the error on the time-of-flight from the range of delays shown in the zoomed window.

$$\Delta_{NIE} = \frac{2\Delta t_{NIE}}{TOF_{IOI}} \cdot \sqrt{\frac{\left(\frac{m}{q}\right)_{IOI}}{m_{CAL}} \cdot \left(\frac{m}{q}\right)_{IOI}} \tag{3.6}$$

Where Δ_{NIE} is the error contribution due to the non-ideal ejection, Δt_{NIE} is the standard deviation of the total time-of-flight obtained for different opening delays of the output mirror (shown in Fig. 3.5), $m_{^{133}Cs}$ is the mass of ^{133}Cs (or the mass of the calibrant used to obtain the Δt_{NIE} data), TOF_{IOI} is the total time-of-flight for the IOI and $\left(\frac{m}{q}\right)_{IOI}$ is the mass-to-charge ratio of the IOI. The values of Δt_{NIE} were determined to be 0.1 ns and 0.5 ns for the data obtained in 2014 and 2016, respectively. The ions which are flying towards the detector very close to the output mirror when switched to open, will experience non-ideal fields due to electrical ringing in the mirror electrodes. This will be reflected in an oscillation in the time-of-flight deviation for the longer opening delays as shown in the lower panel from Fig. 3.5. In the case that the ions experience

these fields, the Δt_{NIE} will be increased to the peak value of the oscillation, which for the figure shown, is about 2 ns.

- Time Resolved Calibration (TRC) Error:

As already discussed, the TRC is the method used for correcting fluctuations in the TOF using a calibrant as a reference. If the fluctuations are not totally corrected, an error contribution should be considered. Two different contributions of this error will be distinguished and quantified based on measurements done during the respective experiments. Both contributions will be calculated based on the statistics available on the calibration blocks (number of events), number of calibration blocks and empirical data calculated from the effective time between calibration blocks (t_{eff}), calculated as Eq. 3.7, where t_i is the center of each calibration block, t_{begin} and t_{end} are respectively the starting and ending time of the acquisition of the IOI and n is the number of calibration blocks.

$$t_{eff} = \frac{2 \cdot (t_1 - t_{begin})^2 + 2 \cdot (t_{end} - t_n) + \sum_{i=2}^{n} (t_i - t_{i-1})^2}{t_{end} - t_{begin}} \tag{3.7}$$

The first contribution attributed to the TRC will increase the width of the IOI peak compared to the peak used for the TRC, reflected in a increase of the determined peak shape parameter σ. This increase is calculated using empirical data, where the root-mean-square of the relative mass deviation caused by the linear interpolation between calibration points was calculated for different time between blocks (t_{eff}) and different statistics of the calibrant on each block. The data was obtained for both experiments in 2014 and 2016 at the FRS-Ion Catcher at GSI due to the changes in the system between the experiments. These calculations can be seen in Fig. 3.6 for both experiments.

The final parameter used for the fit of the IOI data is calculated as shown in Eq. 3.8 and Eq. 3.9.

$$\sigma_{TRC} = \alpha \cdot m_{IOI} \tag{3.8}$$

$$\sigma_{IOI} = \sqrt{\sigma_{cal}^2 + \sigma_{TRC}^2} \tag{3.9}$$

Where σ_{TRC} is the standard deviation to be added due to the TRC contribution, α is the value obtained from the Fig. 3.6 for a certain t_{eff}, m_{IOI} is the mass of the ion of interest, σ_{cal} is the peak shape parameter obtained from the calibrant used for the TRC (after the scaling) and σ_{IOI} is the final peak shape parameter to be used for the fit of

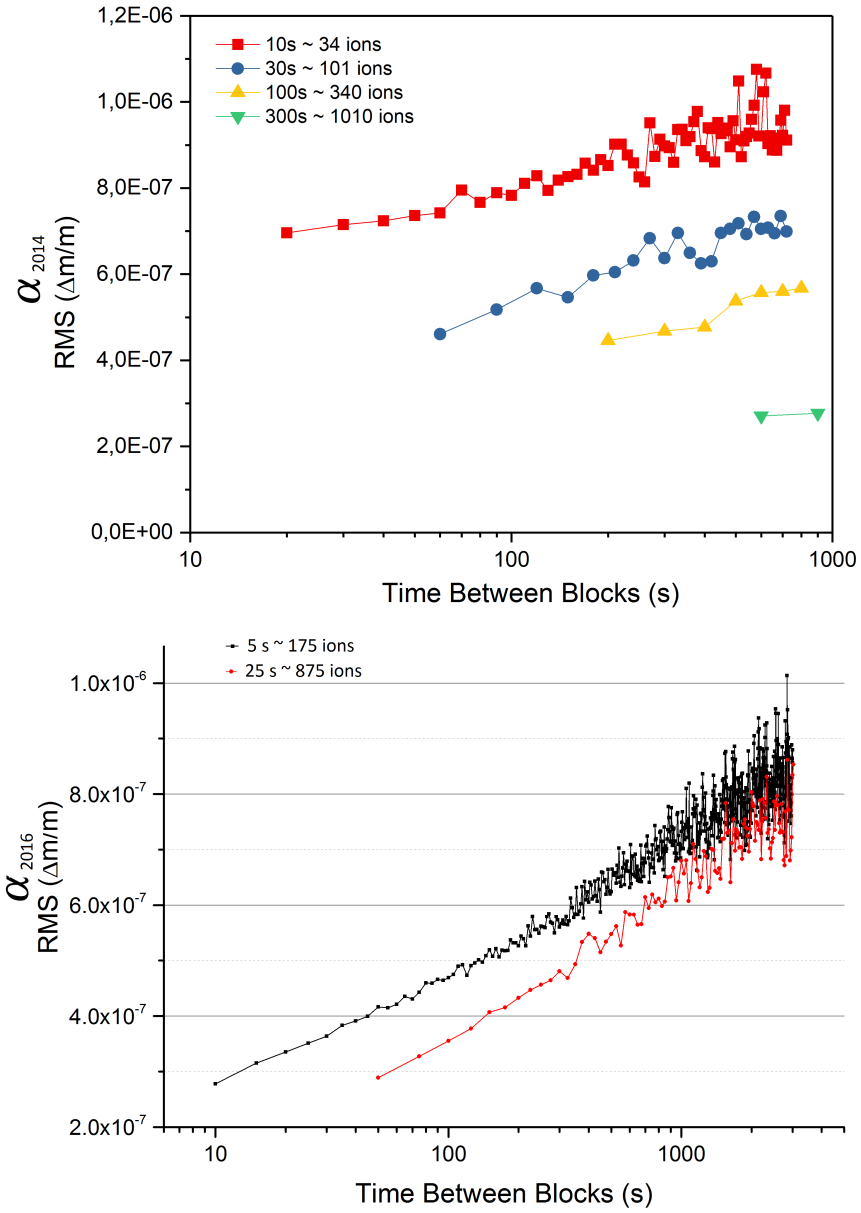

Figure 3.6: Root-mean-square of the relative mass deviation caused by the linear interpolation between calibration points for different time between blocks and different statistics of the calibrant on each block calculated for the data obtained in 2014 (upper panel) and in 2016 (lower panel).

the IOI. For the error of σ, 20% of σ_{TRC} is quadratically added to the error obtained from the peak shape determination.

The second contribution will be reflected directly to the mass uncertainty, taking into account that the linear interpolation between calibration points not only increases the peak width but also can shift the mass center of the peak. In this case, the empirical data used for the calculation of the error contribution, is based on the square root of the quadratic difference between the RMS obtained for the relative mean mass deviation caused by the linear interpolation between each calibrant block and the RMS value

over its statistical determination ($\frac{RMS}{\sqrt{O}}$, where O is the effective number of calibration blocks, calculated as in Eq. 3.10). The value was calculated for different effective time between blocks and different statistics of the calibrant in the blocks. The result is shown in Fig. 3.7.

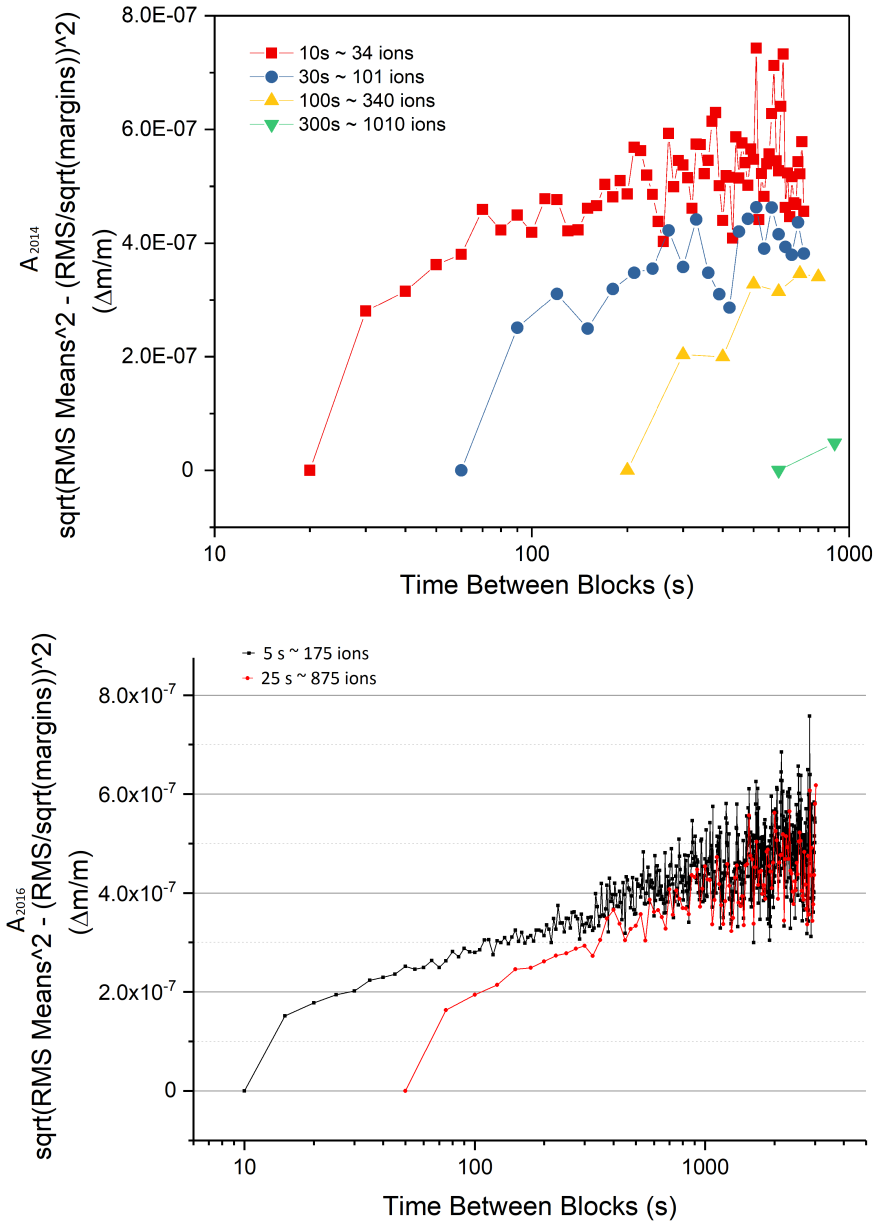

Figure 3.7: Square root of the quadratic difference between the RMS of the relative mean mass deviation caused by the interpolation between each calibration point and the statistical error of the RMS value presented before (defined as A) for different time between blocks and statistics of the calibrant on each block. The upper panel corresponds to data obtained for the 2014 experiment and the lower panel corresponds to data obtained for the 2016 experiment.

The error contribution is calculated using Eq. 3.10 and Eq. 3.11.

$$O = \frac{t_{end} - t_{begin}}{t_{eff}} \tag{3.10}$$

$$\Delta_{TRC} = \frac{A}{\sqrt{O}} \cdot \left(\frac{m}{q}\right)_{IOI} \tag{3.11}$$

Where O is the effective number of calibration blocks, calculated using the end (t_{end}), begin (t_{begin}) of the measurement and the calculated effective time between calibrant blocks (t_{eff}), Δ_{TRC} is the mass uncertainty due to the TRC, A is the value obtained for a certain t_{eff} from Fig. 3.7 and $\left(\frac{m}{q}\right)_{IOI}$ is the mass-to-charge ratio of the ion of interest.

- Calibration Parameters Error (Δt_0, Δc and Δb):

The uncertainty of the calibration parameters will have a direct reflection in the mass uncertainty, see Eq. 1.9. For t_0, the effect in the mass uncertainty is calculated following the formula described in [Rink, 2017]. This error contribution is normally very small for long TOF, being normally a negligible source of error. For c the error contribution to the mass is calculated in MAc by changing c by its error and calculating a new b. Then the deviation of the obtained masses with the different b parameters will be the mass uncertainty contribution of c. The uncertainty of c is zero if calibrant and IOI are performing the same number of turns. The higher the difference of turns between the calibrant used for b and the IOI, the higher the contribution of the error of c. The error of b is included in the precision calibration factor error.

- Scaling Parameter Error:

As already mentioned before, the peak shape parameters, σ and the different τ, have to be scaled from the calibrant where the peak shape was extracted, with certain mass-to-charge ratio, to the mass-to-charge ratio of the IOI. The error is calculated from the difference between the scaling factor calculated taking in account the resolving power or not (see Eq. 3.1 for scaling factor). This error is reflected in the errors of the corresponding scaled peak shape parameters (error of σ and the different τ), where are quadratically added.

- Mass Range Selector (MRS) Error:

As previously discussed, pulsing the MRS influences the TOF of the ions depending on the number of turns that it was pulsed. The uncertainty of this shift ($\Delta MRS_{ShiftCal}$) is assumed to be half of the value ($MRS_{ShiftCal}$). The IOI was acquired with certain

fraction of the time with the MRS switched on $\frac{MRS\_On_{IOI}}{Measurement\_Time}$ and the calibrant was acquired also with a fraction of a time with the MRS switched on $\frac{MRS\_On_{CAL}}{Measurement\_Time}$. For obtaining the final mass uncertainty contribution due to the MRS shift, $\Delta MRS_{ShiftCal}$ is then multiplied by the difference on the fraction of time seen by the calibrant and IOI where the MRS was on.

$$\Delta_{MRS} = \Delta MRS_{ShiftCal} \cdot \left(\frac{MRS\_On_{CAL}}{Meas.\_Time} - \frac{MRS\_On_{IOI}}{Meas.\_Time}\right) \tag{3.12}$$

- TDC Dead-Time Error:

The TDC used for the acquisition of the data, Ortec-9353, has a non-extending dead-time and the detector has an extending dead-time. This means that after the detection of an event, there will be a window of time (1.5 ns in the case of Ortec-9353) where no event will be recorded. The dead-time effect will be stronger in the part of the distribution where more counts are expected, the center. This effect causes that the amplitude of the central part of the peak will be attenuated more than the tails, being translated in a different peak shape, an increase of the σ, which causes a shift in the centroid of the peak acquired under dead-time conditions. A dead-time correction [Greiner, 2017] is implemented in MAc to correct this error. No error contribution has to be added in the data presented in the thesis because the data was not acquired under extreme dead-time conditions.

- Space Charge Error:

This contribution takes in account the interaction of isobaric ions while they are flying close together in the analyzer. The magnitude of this effect is measured and described in [Dickel et al., 2015], $1 \cdot 10^{-8}$ per detected isobaric ion per MR-TOF-MS cycle, and can be neglected for all the data presented in this work.

When dealing with close lying peaks, extra errors will have to be considered, which will be higher if the peaks overlap considerably. In the following, a classification of close lying peaks and a description of the extra error contributions to be taken into account are given.

3.1.1.2 Close Lying Peaks: Definition and Considerations

The data evaluation procedure presented is capable of providing reliable mass values and uncertainties even of close lying peaks. A classification of close lying peaks based on the shape of the summed analytical functions is defined in the following. In Fig. 3.8 an example of each class of close lying peaks is presented.

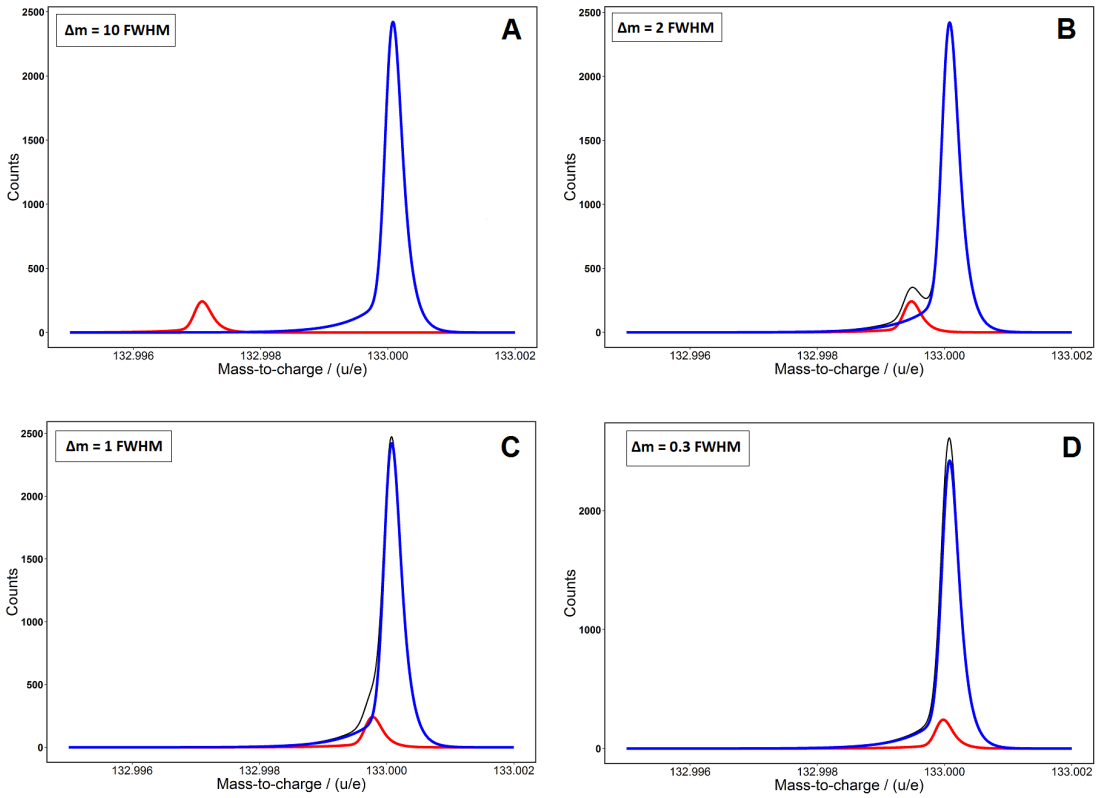

Figure 3.8: Example of close lying peaks (Hyper-EMG(1,1)) corresponding to the introduced classification. The peak shape parameters are the same for both peaks and were obtained from real data. Different distances between the peaks (Δm) of 10 FWHM, 2 FWHM, 1 FWHM and 0.3 FWHM are plotted keeping a constant areal ratio of 1 (red) to 10 (blue). The black line is the sum of both peaks. The parameters of the plotted peaks are: FWHM = $3 \cdot 10^{-4}$ u, $\sigma = 1 \cdot 10^{-4}$ u, $\mu_{blue} = 133$ u, $\mu_{red} = 133$ u - [30,6,3,1]$\cdot\sigma$, $\tau_{L_1} = 5 \cdot 10^{-4}$ u, $\tau_{R_1} = 1.4 \cdot 10^{-4}$ u, $\theta = 0.15$ and $A_{blue} = 10 \cdot A_{red}$.

A) The sum of the peaks reaches zero between the peaks. In this case the peaks can be considered as non-overlapping and an independent analysis can be performed.

B) The sum of the peaks has a minimum between the peaks different than zero. This can be considered as resolved overlapping peaks and an analysis for overlapping peaks will be performed. The determination of the peak shape is important for extracting the mass and areal ratios of the peaks.

C) The sum of the peaks does not have a minimum between the peaks. The effect of the overlap between the peaks can be seen only as a change in the peak shape (a shoulder, a broadening...) in the peaks. In this challenging case, the proper determination of the peak shape is crucial in order to first detect the existence of a second peak and second to extract the mass and areal ratios of the peaks.

D) No change in shape can be seen in the sum of the peaks. This is considered as non-resolved overlapping peaks and an extra error will be taken in account as

described later.

To which class belong two close lying peaks will be defined by the mass difference between the peaks, the shape and the areal ratio of the peaks.

The overlap between peaks causes that the fitted masses of the peaks tend to have a smaller distance (bias). The closer the peaks and the higher the difference in area, the stronger the effect of the bias in the mass. To cope with this, a bias correction method was developed and is applied to the data where close lying peaks are considered as overlapping peaks [Ebert, 2016]. This method, consists in a first estimate of the masses of each peak (m_{2FIT} and m_{1FIT}), area ratio (A_{1FIT} / A_{2FIT}) and the total number of events (N_{EVENTS}) with wMLE fits. Then, N spectra are simulated with the parameters obtained. The N spectra are then fitted and an average mass distance of the simulated data is calculated ($\Delta m_{SIM_{AVG}}$). The mass distance obtained with the original data and the average distance obtained with the N simulations of the data is compared (δ = Δm_{FIT} - $\Delta m_{SIM_{AVG}}$). If $|\delta|$ is lower than a certain threshold, ε, then a final fit with a fixed distance between the peaks corresponding to the calculated Δm is performed. If $|\delta|$ is larger than the threshold, new simulated data is generated with a corrected distance (Δm - δ) and the fit of the data is repeated. In Fig. 3.9 a flow of the bias correction procedure for overlapping peaks is shown. Typical values for this procedure are N = 100 simulated spectra and a threshold on the mass distance $\varepsilon = 0.002 \cdot$ FWHM, with the FWHM calculated from the peak model.

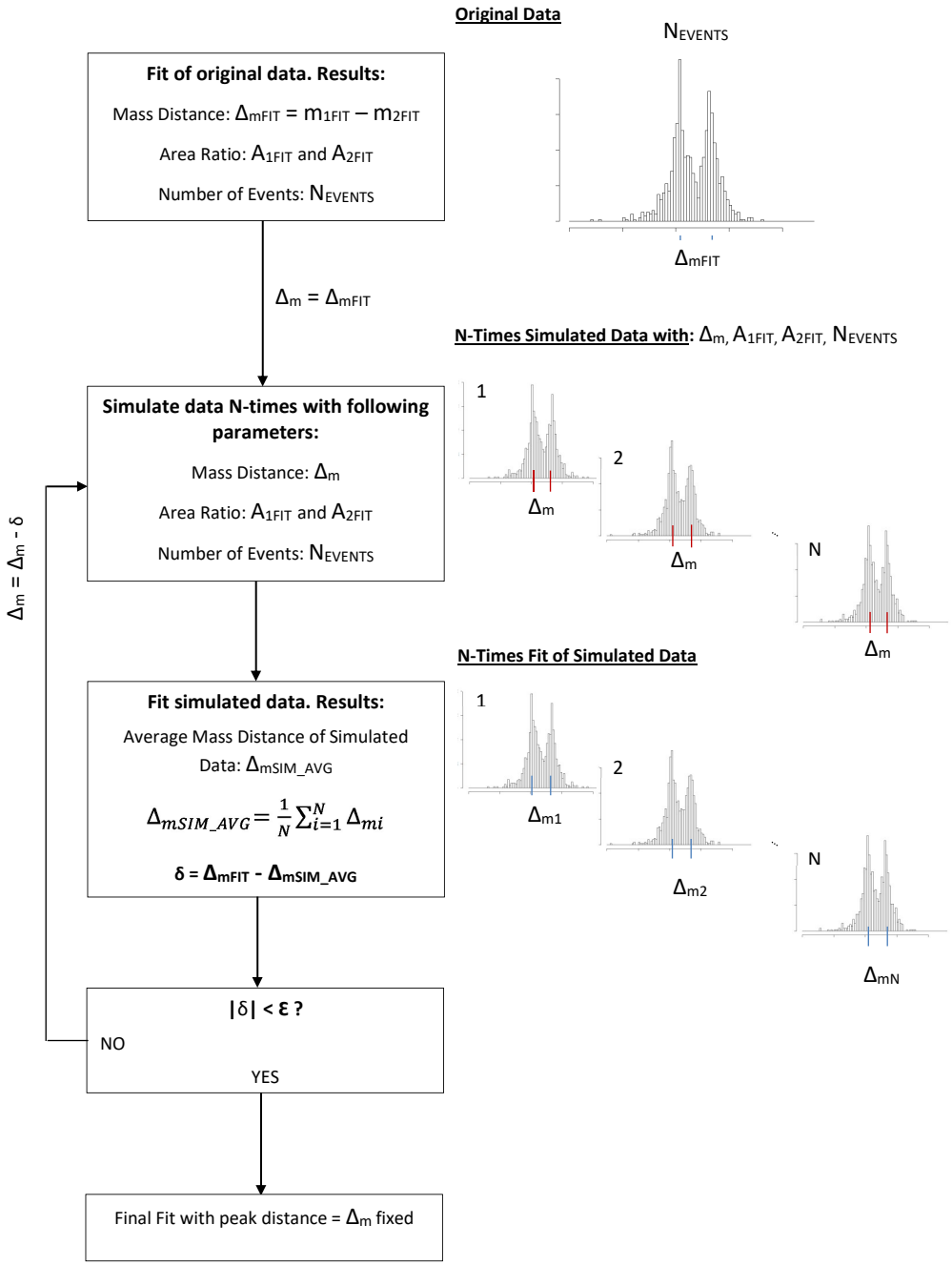

Figure 3.9: Flow diagram of the iterative bias correction method used for fitting two overlapping peaks with a certain mass difference. Based on [Ebert, 2016].

The effect of the bias correction method on the mass distance for simulated overlapping peaks of class C can be seen in Fig. 3.10.

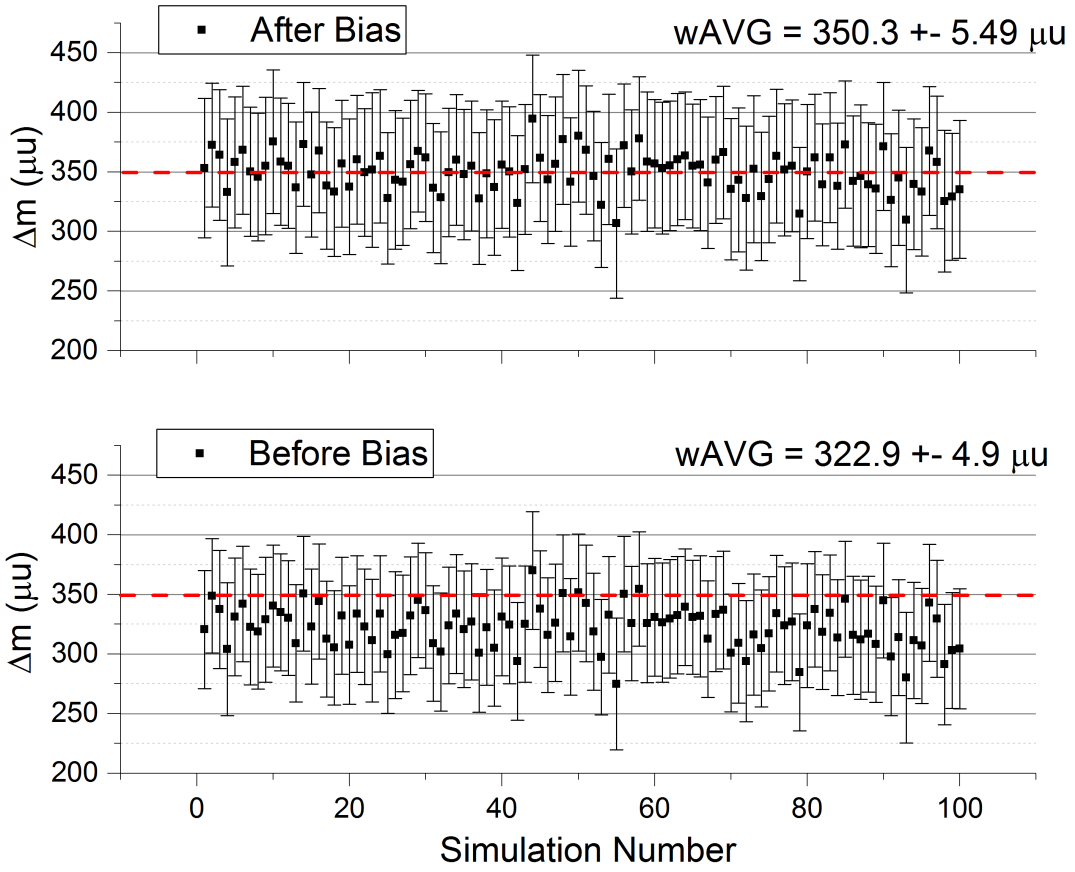

Figure 3.10: Mass difference obtained before and after the bias correction for 100 simulated spectra of class C overlapping peaks. The simulated data contained two overlapping peaks separated by $\Delta m = 3.5 \cdot 10^{-4}$ u (marked with a red dashed line) with a total of 1000 events. The upper values show the weighted average of the peak distance weighted with the uncertainty obtained for each fit. The peak shape used for simulating the data was: FWHM = $3 \cdot 10^{-4}$ u, $\sigma = 1 \cdot 10^{-4}$ u, μ_1 = 132.99965 u, μ_2 = 133 u, $\tau_{L_1} = 5 \cdot 10^{-4}$ u, $\tau_{R_1} = 1.4 \cdot 10^{-4}$ u, $\theta = 0.15$ and the ratio between the peaks was $A_1 = 0.25 \cdot A_2$. This peak shape was obtained from the calibrant of Fig. 3.17.

This simulations shows that the distance between peaks can be reproduced correctly by the bias correction. In Fig. 3.11, examples of bias correction from real data evaluated in this thesis are presented. Here, the deviation from the literature value of the measured mass difference of the isomers, before and after the bias correction are presented. All this pairs of ground and isomeric state correspond to overlapping peaks of class C. As can be seen in the figure and already shown before with simulated data, the first estimate of the fit (before the bias correction) on overlapping peaks of class C, tends to provide a smaller mass distance, which after the bias correction is within the error bars of the literature distance. For the overlapping peaks of class B, this bias effect is

almost negligible since the peaks are resolved, therefore the mass distance is almost not changed before and after the bias correction.

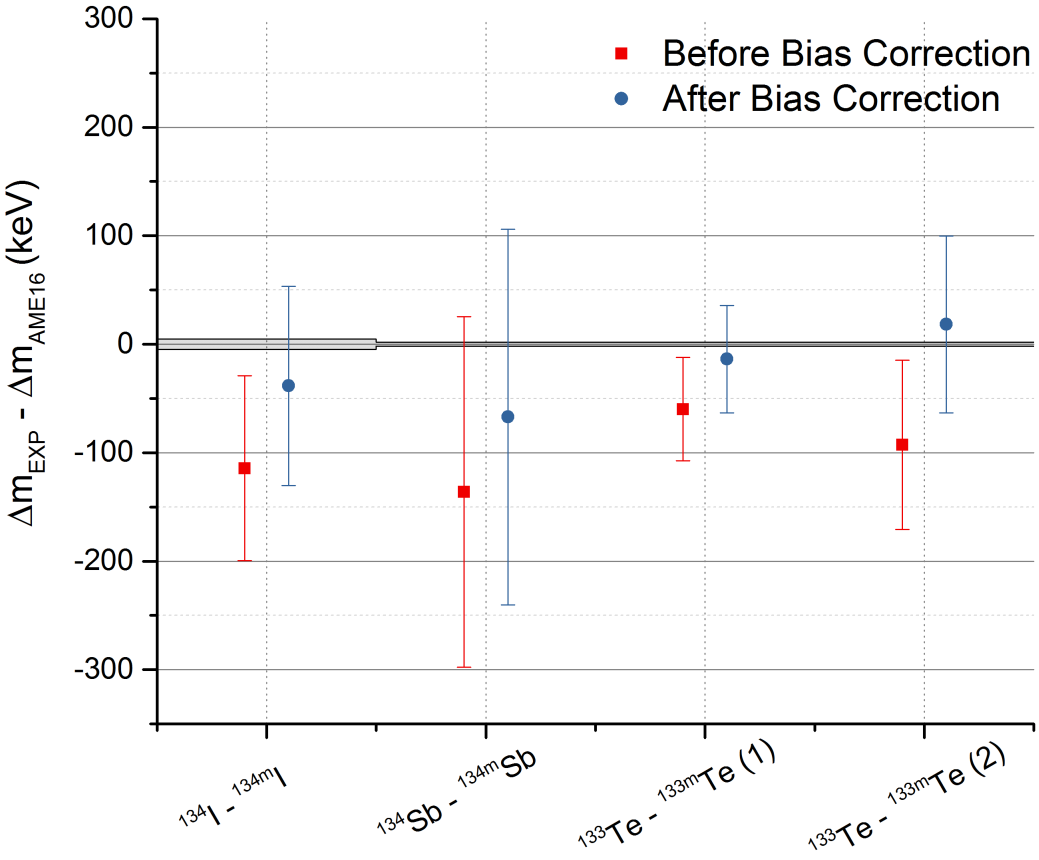

Figure 3.11: Deviation from literature of the distance between peaks (isomers) for class C overlapping peaks before (red) and after (blue) the bias correction. The error bar of the measurements before the bias correction does not include the bias correction error. In grey, the error bar of the mass difference calculated from the literature [Huang et al., 2017]. The data corresponds to the measurements performed with the MR-TOF-MS from the FRS-Ion Catcher, presented later in this chapter.

After describing the special treatment needed when fitting close lying peaks and the classification of different levels of close lying peaks, the extra uncertainties to be considered in a double peak fit are introduced in the following.

- Bias Correction Error of Overlapping Peaks:

The bias correction error arises from the uncertainty of the shift performed by the bias correction method of the overlapping peaks. In the tests performed showed in Fig. 3.10, the final error amounts to about 25% of the shift, therefore, the error from the bias correction is calculated as 25% of the absolute difference between the masses obtained with and without the bias correction.

- Unresolved Peaks Error:

When there is a possibility of two close lying peaks of class D, an extra error will be added to the masses obtained. In case that the expected peaks have a known distance and the ratio is not known, for example an unresolved isomer, isobar or an expected contamination, a factor of $\frac{\sqrt{3}}{6}$ times the mass difference of the non-resolved peaks will be the uncertainty contribution due to non-resolved peaks [Huang et al., 2017]. For the masses, a single peak fit is performed and half of this known distance will be added and subtracted to obtain the mass value of the two unresolved peaks. If the measured spectrum presents in addition unknown peaks close to the IOI, the contribution to the mass of the IOI from a possible underlying peak is estimated and added. The estimate of this contribution is obtained with simulated data containing two peaks: one representing the IOI and the other a possible contamination. As a reference for the areal ratio between the IOI and the contamination, the highest unknown peak appearing in the same mass number as the IOI is taken. Then, the contaminant peak is moved over the IOI, calculating the mass shift and the single peak KS test for the different distances. For the error contribution, the maximum shift weighted with the corresponding p-value of the KS test is taken.

The final mass uncertainty taking into account all the different sources of error that affect to the mass value, is calculated by the square root of the sum of the squares of the different sources, see Fig. 3.12.

3.1.1.3 Data Combination and Multiply Charged Ions

For the combination of independent mass measurements obtained of the same IOI, a weighted mean is performed as shown in Eq. 3.13, assuming that all errors are independent from each other:

$$\left(\frac{m}{q}\right)_{Comb} = \frac{\sum_i^N \sigma_i^{-2} \cdot \left(\frac{m}{q}\right)_i}{\sum_i \sigma_i^{-2}} \tag{3.13}$$

where N is the number of values $(\frac{m}{q})_i$ and σ_i to be combined. The value of the combined uncertainty will be calculated depending whether a) N different data sets were evaluated or weather b) the same data set was evaluated but with N different analysis. Eq. 3.14 and Eq. 3.15 are used for the calculation of the combined uncertainty for case a) and b) respectively.

$$\sigma_{Comb} = \frac{1}{\sqrt{\sum_i^N \frac{1}{\sigma_i^2}}} \tag{3.14}$$

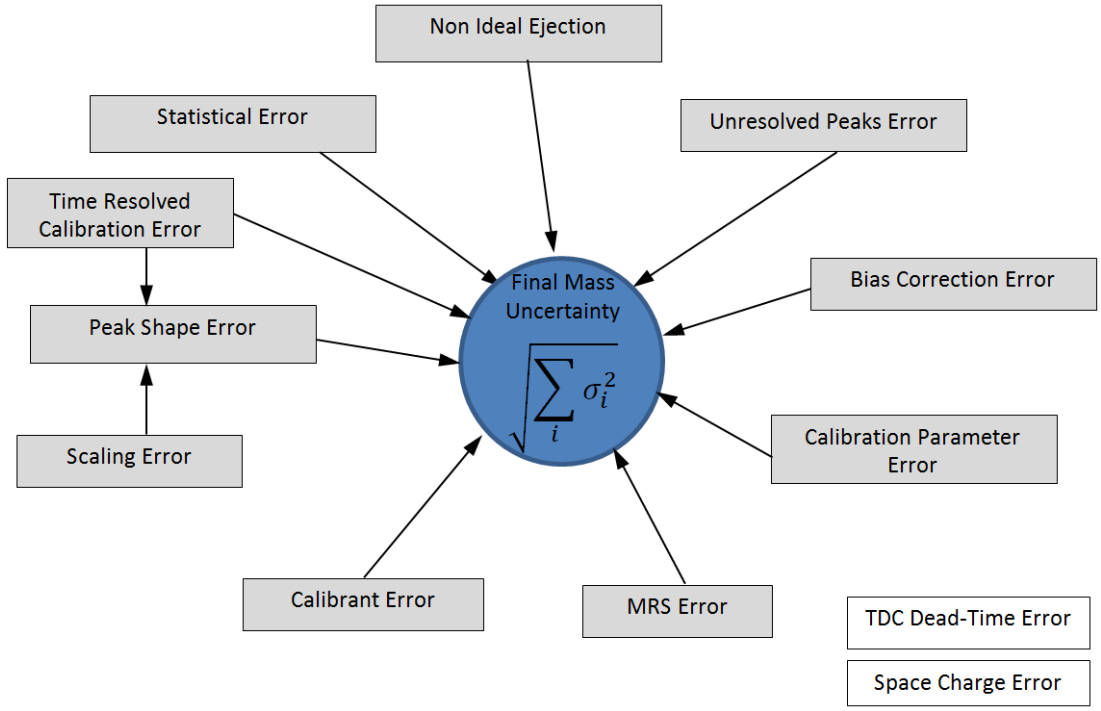

Figure 3.12: Diagram of the relationship of the errors to the total mass uncertainty. The uncertainty contributions corresponding to the TDC dead-time and space charge are negligible in the current uncertainty level of the spectrometer. Bias correction and unresolved peaks error affect only in case of close lying peaks which overlap. The explanation of the error sources has been presented before.

$$\sigma_{Comb} = \frac{1}{\sum_i^N \frac{1}{\sigma_i}} \tag{3.15}$$

For the calculation of the mass of ions measured in charge state (q) higher than 1, the mass-to-charge ratio and uncertainty obtained from the described data evaluation process have to be converted in an absolute mass value and uncertainty following Eq. 3.16 and Eq. 3.17, respectively:

$$m_{IOI} = \left(\frac{m}{q}\right)_{IOI} \cdot q_{IOI} + m_e \cdot q_{IOI} \tag{3.16}$$

$$\sigma_{IOI} = \sigma_{IOI(m/q)} \cdot q_{IOI} \tag{3.17}$$

where m_{IOI} and σ_{IOI} represent the final atomic mass and uncertainty, $\left(\frac{m}{q}\right)_{IOI}$ and $\sigma_{IOI(m/q)}$ represent the mass-to-charge ratio and its uncertainty obtained in the data evaluation process, m_e represents the electron mass and q_{IOI} represent the charge state of the measured ion of interest.

3.1.2 Identification of Molecules and Exotic Nuclei Via High Accuracy Mass Measurements

The unique features, namely the combination of a broad mass range and a high resolving power exhibited by the MR-TOF-MS, can be used for the identification of several species via high precision mass measurements. In essence, the characteristic footprint of the atomic mass defect, allows the identification of the individual species and the composition of molecules. In the following, identification of uranium ions and uranium molecules with different charge states for studies of the cleanliness of the system is demonstrated. Moreover, the identification of several fission fragments produced in the FRS will be shown, introducing an efficient unambiguous identification method for mass measurements of several exotic fragments at once.

3.1.2.1 Identification of ^{238}U Charge States and Molecules

A ^{238}U primary beam was injected into the CSC, stopped and extracted to the MR-TOF-MS for identification. Uranium is one of the most reactive elements and tends to react with oxygen, water, hydrocarbons, etc. forming molecules, specially uranium oxide [^{238}U^{16}O] [Anicich, 2003]. The first ionization potential (IP) of uranium is 6.19 eV, the second is 10.6 eV. When the uranium primary beam is stopped in the helium gas of the CSC, a distribution of singly and doubly charged ions is expected when nitrogen is the main contamination of the gas inside the CSC and the MR-TOF-MS. The third IP of uranium is higher than the IP of nitrogen, 15.6 eV. Therefore, no ^{238}U^{+3} is expected to be formed in the system. The molecules, are formed after stopping the uranium, during the extraction from the CSC. The MR-TOF-MS was used for the identification of uranium and uranium molecules in different charge states. In Fig. 3.13, a spectrum showing the identification of ^{238}U^{+1} and [^{238}U^{16}O]$^{+1}$ is presented. The two isobars with A = 208 (^{208}Pb^{+1} and ^{208}Tl^{+1}), used for calibration, are delivered from the radioactive ^{228}Th source placed inside the CSC. The mass window analyzed by the MR-TOF-MS exceeds 40 mass units, with a resolving power of about 100000, being able to resolve isobars which are less than 5 MeV/c^2 separated. The identified nuclei and molecules presented in Fig. 3.13 perform different numbers of turns in the analyzer. The isobars at A = 208 perform 137 turns, ^{238}U^{+1} performs 128 turns and [^{238}U^{16}O]$^{+1}$ performs 124 turns. Also, ^{238}U^{+2} and doubly charged uranium molecules ([^{238}U^{16}O]$^{+2}$, [^{238}U^{16}O$_2$]$^{+2}$ and [^{238}U^{16}O^{1}H]$^{+2}$) with higher rate than the singly charged, were identified.

Although the purity of the gas was improved in the MR-TOF-MS as well as in the CSC, [^{238}U^{16}O], [^{238}U^{16}O$_2$] and [^{238}U^{16}O^{1}H] in singly and mainly in doubly charge state were identified. With ultra-pure helium buffer gas used in the CSC obtained

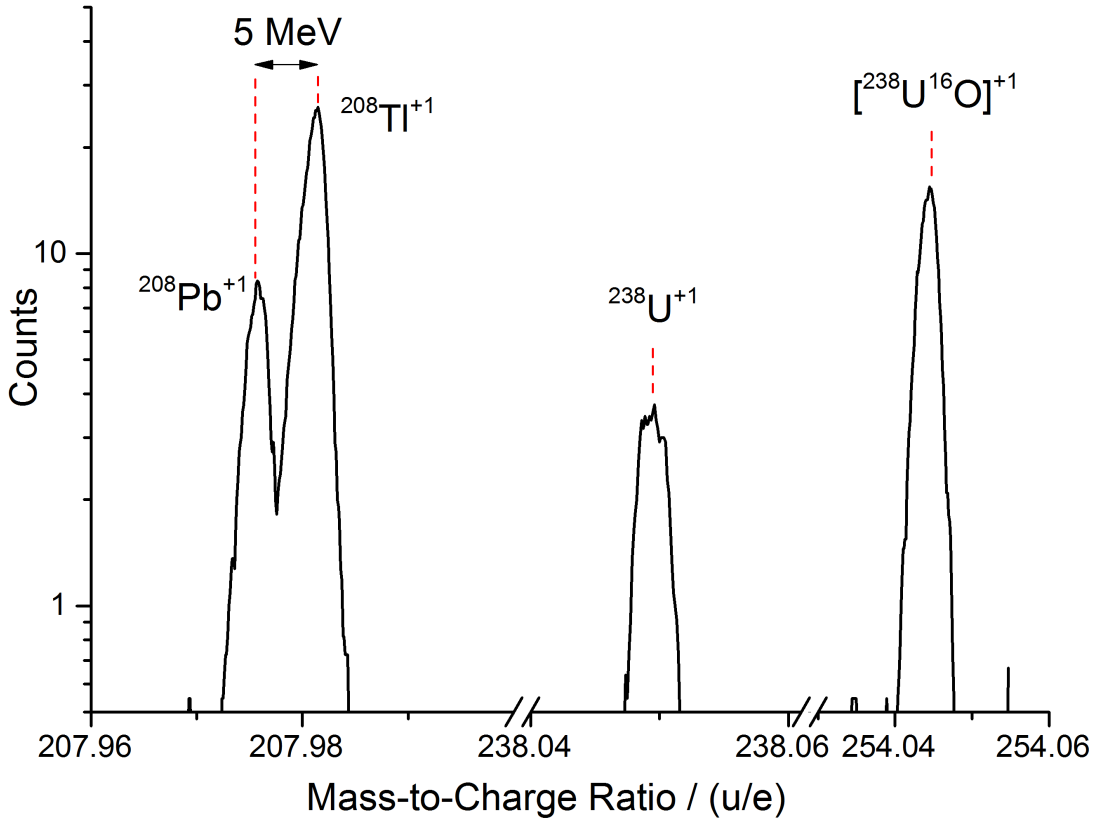

Figure 3.13: Identification by mass (or mass defect) of $^{238}U^{+1}$ (128 turns) and $[^{238}U^{16}O]^{+1}$ (124 turns). Calibrants with A = 208 (137 turns) from the ^{228}Th radioactive source in the CSC are used. Traces of other molecules such as $[^{238}U^{16}O_2]^{+1}$ or $[^{238}U^{16}O^{1}H]^{+1}$ were also identified in this spectrum.

by active gas purifiers, where the suppression of hydrogen, nitrogen and oxygen is higher, the amount of formed molecules will be further reduced in the future. New developments will also perform a improved CID, dissociating the remaining molecules and obtaining a clean spectrum out of the CSC. Gas traces inserted in the CSC will allow the manipulation of the charge state.

The combination of a broad mass range with resolving powers exceeding 100000 presented by the FRS-Ion Catcher's MR-TOF-MS is an ideal tool to perform diagnostics of the CSC during operation and commissioning.

3.1.2.2 Identification of ^{238}U Fission Fragments

As for the molecules, the MR-TOF-MS can also be used for the identification of atomic ions via high precision mass measurements, which will be described in the following. ^{238}U fission fragments were produced at 300 MeV/u in a beryllium target and in-flight separated in the FRS, range bunched, stopped in the CSC and extracted towards the

MR-TOF-MS for identification via high precision mass measurements. The unique combination of broad mass range and high mass resolving powers, exceeding 100000, enabled an efficient identification of all the stopped fragments in the CSC at once. The mass range selector (MRS) of the MR-TOF-MS was set to select a mass window of 8 u, between 113.6 u and 121.6 u. The time-of-flight spectrum obtained for the stopped fragments can be seen in Fig. 3.14. In this spectrum, the used reference ion with A = 119 was set to perform 128 turns.

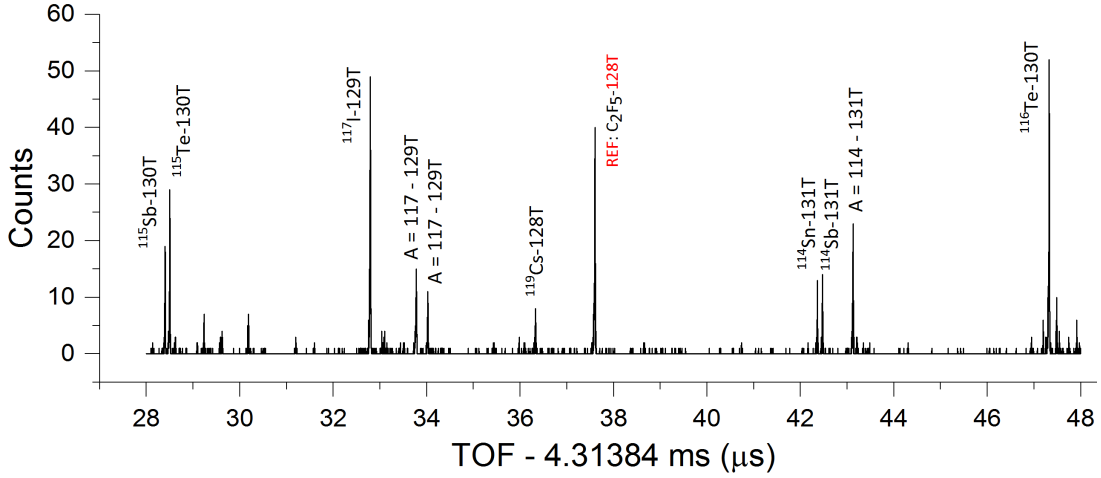

Figure 3.14: Time-of-flight spectrum for the stopped fragments in the CSC. The labels represent the assigned identification performed via high accuracy mass measurement, including the number of turns for each species. The reference mass with A = 119, $^{12}C_2$ $^{19}F_5$, is produced by the electron impact ion source from the MR-TOF-MS and set to perform 128 turns. No collision induced dissociation (CID) for the suppression of the molecules was employed. The x-axis presents the total-time-of-flight minus an offset of 4.31384 ms.

The fragments measured in the MR-TOF-MS correspond to mass numbers from A = 114 to A = 119 (except of A = 118, which is outside the analyzer window). They perform different number of turns, ranging from 128 to 131 turns. Also, peaks corresponding to molecules at mass numbers A = 114 and A = 117 are seen. Many spectra such as the one shown in Fig. 3.14 were recorded during the experiment to perform identification of the fragments delivered by the FRS.

In such spectra where many species are performing different number of turns, there is the possibility of a misidentification. In order to unambiguously identify the different species from a broad mass range without loosing statistics, a comparison with a spectrum where the species perform a different number of turns is performed. For instance, if with the help of the reference ion with 128 turns, the TOF spectrum shown in Fig. 3.14 is converted to a mass spectrum, a tentative identification of the nuclei ^{117}I and ^{117}Cs can be performed for 129 turns as shown in the top panel of Fig. 3.15.

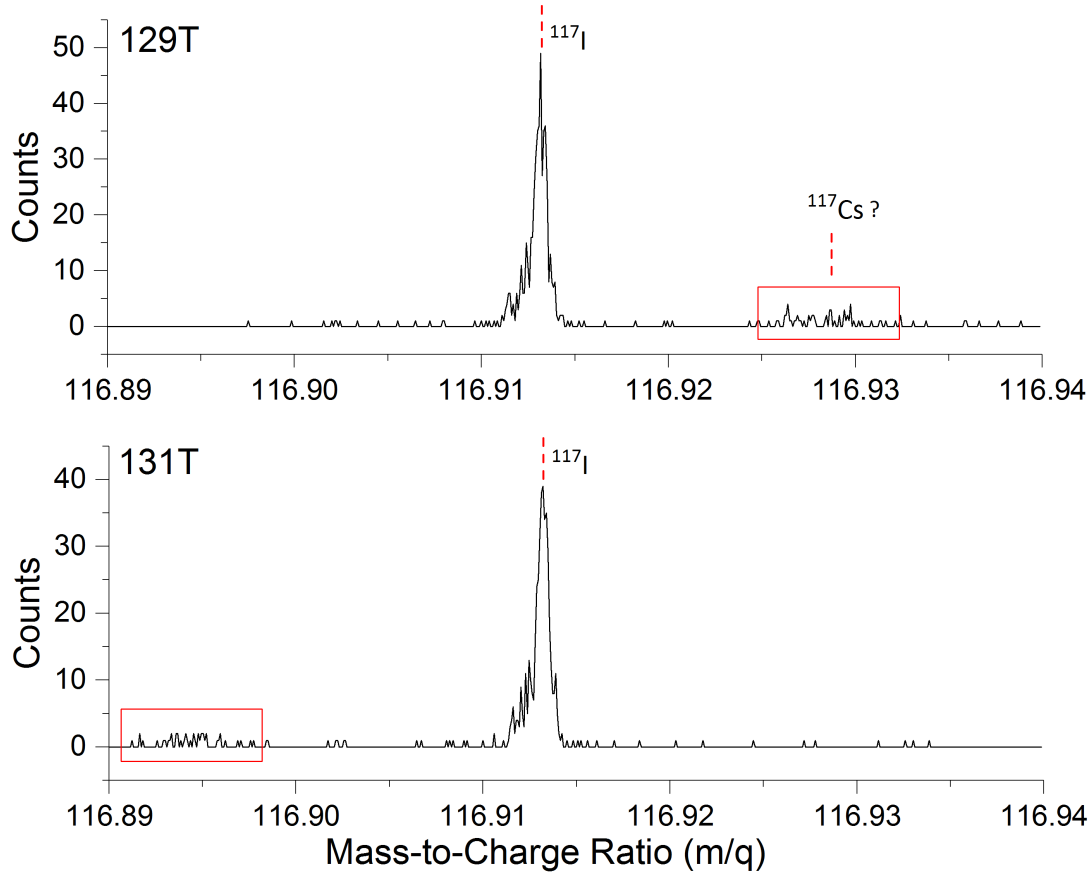

Figure 3.15: Mass spectrum for A = 117 performing 129 and 131 turns. The tentative identification of ^{117}Cs performing 129 turns is discarded by observing the spectrum taken with two more turns, where the supposed peak of ^{117}Cs has moved away, revealing that this peak does not correspond to the mass number A = 117.

If a spectrum is taken with two turns more, the tentative identification of isobars, which in reality can be species with other mass number, will be confirmed or discarded. As can be seen in the lower panel of 3.15, the tentative identification of ^{117}I is confirmed since the peak is identified again with the proper mass at 131 turns. However, for ^{117}Cs, the identification is discarded because with 131 turns the peak is no longer at the same mass position, revealing that in reality the peak corresponds to a mass number A $\neq$ 117. By combining both spectra obtained with different number of turns, an unambiguous identification of the species, discarding possible overlaps between different mass numbers, is obtained. In terms of efficiency, this unambiguous identification is performed with no event losses for the fragments. This is a very important, fast, reliable and powerful method when performing mass measurements of several exotic nuclei of different mass numbers at once.

3.1.3 Direct Mass Measurements of ^{238}U Fission Fragments

During a beamtime at GSI in fall 2014, fission fragments were produced with a primary beam of ^{238}U at 1000 MeV/u in a beryllium target, in-flight separated in the FRS, range bunched in a monoenergetic degrader, stopped in the cryogenic stopping cell and transferred to the MR-TOF-MS for direct mass measurements. The data acquired from the different nuclei extracted to the MR-TOF-MS was analyzed with the procedure described before, and the mass values and their uncertainties were determined. The fragments measured in the context of this work are: ^{134}I and ^{134m}I, ^{133}I and ^{133m}I, ^{134}Xe and ^{134m}Xe, ^{134}Te, ^{134}Sb and ^{134m}Sb and ^{133}Te and ^{133m}Te. The nuclei with the shortest half-life corresponds to the isomer ^{134m}Xe, 290 ms. Calibration was always performed using isobars from the internal sources of the MR-TOF-MS, delivering ^{133}Cs and xenon isotopes (^{134}Xe was used). In Fig. 3.16 the deviation between the obtained masses in this work and the Atomic Mass Evaluation 2016 (AME16) [Huang et al., 2017] is shown.

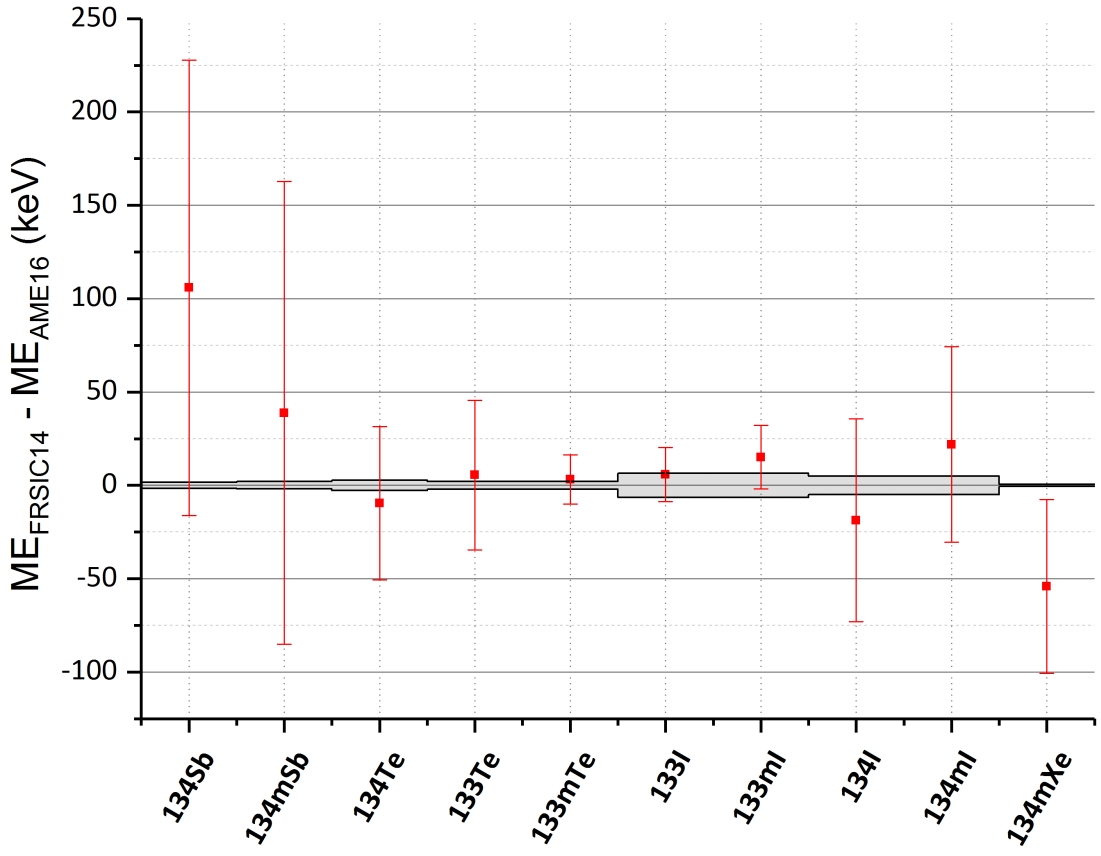

Figure 3.16: Mass excess deviation between this experiment (see Tab. 3.1) and the literature values [Huang et al., 2017]. The error bars represent the total uncertainty given in Tab. 3.1. The mass uncertainty from the literature is represented by the grey area.

In this experiment, the kinetic energy of the ions in the MR-TOF-MS analyzer was 1.3 keV, the mirrors were switched on and off with just one electrode each and the

voltages supplied to 4 electrodes of the analyzer were generated from low-noise high stable commercial power supplies. The rest of improvements were not implemented for this experiment because they were developed afterwards. The measured masses are in agreement with the literature values. In Tab. 3.1 the results of the mass measurement for this experiment after the analysis procedure described before are shown. When two or more independent measurements of the same nuclei were done, a weighted mean and its error are calculated as described in Section 3.1.1.3. The error contributions taken into account for these measurements are: statistical error, peak shape error, bias correction error, calibrant error (includes the literature error) and TRC error. The non-ideal ejection error contribution to the total uncertainty is negligible, being below 3 keV in average (Δt_{NIE} = 0.1 ns for this experiment). The time-of-flights for this data are much longer than the error of t_0, and due to the isobaric calibration, always performed with the same number of turns as the IOI, the error of c can be neglected. The MRS error is zero in all the cases since the calibrant and IOI always experience the same MRS fields. No background peaks close to the IOI were seen and no overlapping peaks of class D were detected, therefore, the unresolved peaks error did not contribute to the final mass uncertainty in this experiment. The low background was achieved in this experiment due to two reasons: the low rates injected in the CSC of about 500 ions per second, where about half of the injected ions corresponded to the IOI and second, due to the use of the MRS for selecting a single mass unit. The contributions to the total uncertainty are shown in Tab. 3.2.

Nuclei	**Mass**$_{FRSIC14}$ (u)	**ME**$_{FRSIC14}$ (keV)	Δ_{ME} (keV)	**Calibrant**
^{134}I	133.909756 (58)	-84062 (54)	-19 (54)	^{134}Xe
^{134m}I	133.910139 (56)	-83705 (52)	22 (52)	^{134}Xe
^{133}I	132.907834 (14)	-85852 (13)	6 (15)	^{133}Cs
^{133m}I	132.909598 (17)	-84209 (15)	15 (17)	^{134}Cs
^{134m}Xe	133.907445 (50)	-86214 (47)	-54 (47)	^{134}Xe
^{134}Te	133.911386 (44)	-82543 (41)	-10 (41)	^{134}Xe
^{134}Sb	133.920649 (130)	-73915 (122)	106 (122)	^{134}Xe
^{134m}Sb	133.920877 (133)	-73703 (124)	39 (124)	^{134}Xe
^{133}Te	132.910969 (43)	-82932 (40)	5 (40)	^{133}Cs
^{133m}Te	132.911326 (14)	-82600 (13)	3 (13)	^{133}Cs

Table 3.1: Results of direct mass measurements performed in the FRS-Ion Catcher in an experiment in 2014 with ^{238}U fission fragments. Measured atomic mass and mass excess, mass excess deviation from literature (Δ_{ME} = ME$_{FRSIC14}$ - ME$_{lit}$) and the calibrant used are included. The uncertainties shown correspond to the total experimental uncertainty.

In none of the data of this experiment, a side peak was needed to obtain an accurate description of the peak shape. The masses of all nuclei presented here, are already known to high precision. They are therefore ideal test cases for the new instrument and the de-

veloped analysis method, specially where low lying isomers are present and low statistics are available. This will be shown in the following. The ratio of detected isomeric state nuclei to ground state nuclei of the following pairs was calculated: ^{134m}Sb/^{134}Sb = 1.08 $\pm$ 0.73, ^{133m}Te/^{133}Te = 4.12 $\pm$ 0.26, ^{134m}I/^{134}I = 1.26 $\pm$ 0.26, ^{134m}Xe/^{134}Xe = 0.035 $\pm$ 0.006, ^{133m}I/^{133}I = 0.35 $\pm$ 0.02.

Nuclei	**Statistical** ($\cdot 10^{-7}$)	**Peak Shape** ($\cdot 10^{-7}$)	**Bias** ($\cdot 10^{-7}$)	**Calibrant** ($\cdot 10^{-7}$)	**TRC** ($\cdot 10^{-7}$)	**Total Rel.** ($\cdot 10^{-7}$)	**Total Abs.** (μu)
^{134}I (1)	4.1	0.7	0.6	0.4	2.3	4.8	64
^{134}I (2)	9.3	2	2.6	0.7	2.7	10	137
^{134m}I (1)	4.4	2.4	0.9	0.4	2.6	5.6	75
^{134m}I (2)	5.6	0.1	1	0.7	2.7	6.4	85
^{133}I (1)	0.6	0	0	0.2	0.9	1.1	15
^{133}I (2)	2.5	0.1	0	0.2	1.4	2.9	38
^{133m}I (1)	1.1	0.1	0	0.2	0.9	1.4	19
^{133m}I (2)	2.6	0.1	0	0.2	1.4	3	40
^{134m}Xe	2.6	1.4	0.1	0.4	2.3	3.8	50
^{134}Te	2.3	0.2	0	0.4	2.3	3.3	44
^{134}Sb	9.4	0.5	0.7	0.4	2.3	9.7	130
^{134m}Sb	9.6	1.3	0.7	0.4	2.3	9.9	133
^{133}Te (1)	1.7	3.2	0.9	0.2	0.9	3.8	51
^{133}Te (2)	5.6	0.2	1.9	0.2	1.4	6.1	81
^{133m}Te (1)	0.6	0.3	0.1	0.2	0.9	1.1	15
^{133m}Te (2)	2	0.4	0.4	0.2	1.4	2.5	33
AVG.	**4**	**0.8**	**0.6**	**0.3**	**1.8**	**4.7**	**63**

Table 3.2: Individual relative contributions to the total uncertainty for the ^{238}U fission fragments measured during the experiment in 2014 with the MR-TOF-MS, including the total absolute uncertainty. For the definition of each error contribution see Section 3.1.1.1 and Section 3.1.1.2. The number in brackets in the first column represents different data sets evaluated for the same IOI. The average of each independent contribution given in the table corresponds to the average of all the measured nuclei, independent if the error was contributing or not.

As shown in Tab. 3.2, the main contribution to the mass uncertainty from the measurements performed in 2014 relies in the statistical uncertainty. The contribution due to the time resolved calibration (TRC) will be reduced in the future by getting constantly a calibrant specie in the spectrum.

In Fig. 3.17, a typical spectrum taken with the MR-TOF-MS during the beamtime in 2014 and analyzed with the procedure described before is shown. In this spectrum, the calibrant and two nuclides with their long-lived isomeric states, can be seen. The masses and excitation energies of all the nuclei present are well-known from literature.

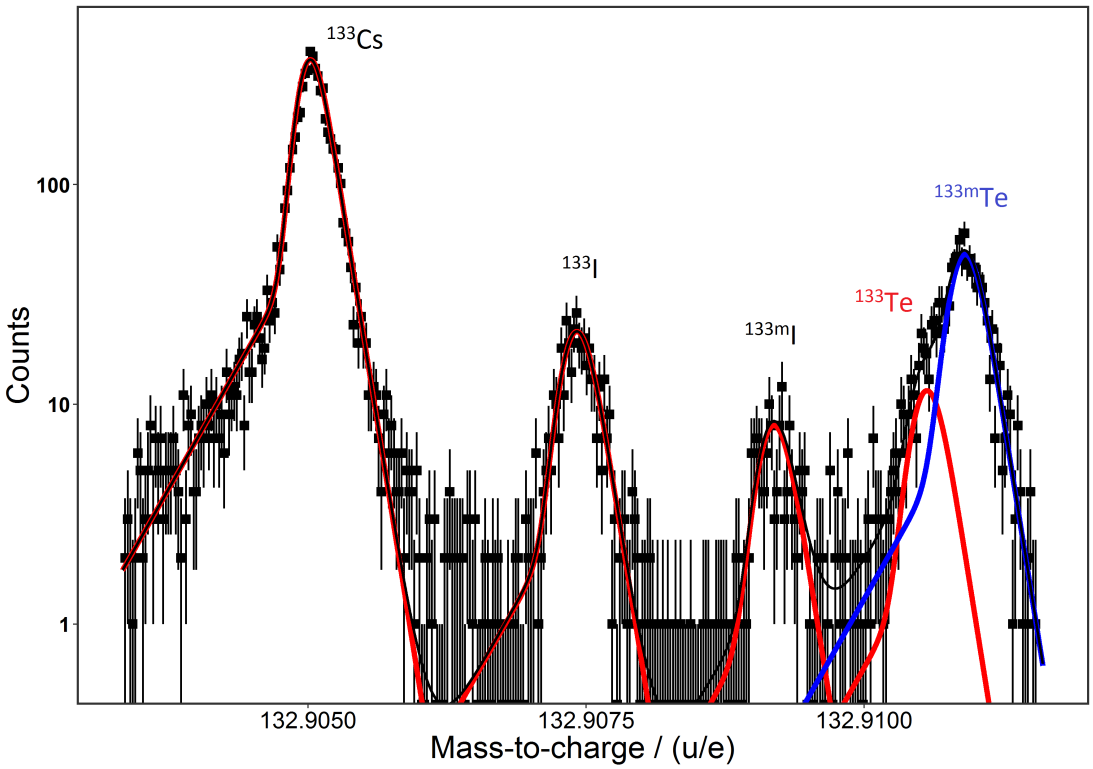

Figure 3.17: Mass spectrum in logarithmic scale taken with the MR-TOF-MS during the experiment in 2014. The binned original data and the fits with the Hyper-EMG(1,1) function are plotted. The spectrum is calibrated with ^{133}Cs. The nuclei ^{133}I, ^{133m}I (with an excitation energy of about 1.6 MeV) and ^{133}Te, ^{133m}Te (with an excitation energy of about 300 keV), were in-flight produced in the FRS via fission, stopped in the CSC and extracted to the MR-TOF-MS. The black line represents the sum of all the fits, in red and blue (double peak fit) the fitted function to the different peaks.

The acquisition time for this measurement was about 2 hours. The excitation energies of the isomers are around 1.6 MeV for the case of the iodine and around 300 keV for the tellurium. The radioactive beam produced in the FRS and stopped in the CSC, was merged in the switchyard with stable ^{133}Cs from the internal thermal ion source of the MR-TOF-MS for calibration purposes. In the case of iodine, the ground state and the

isomeric state can be clearly resolved. In the case of the tellurium (ground state and isomeric state), the peaks are overlapping and only a shoulder on the left side of the isomeric peak corresponding to the ground state can be seen. These conditions present a challenge to extract the mass and areal ratio of the ground state and the isomeric state with a minimal uncertainty. Here, the analysis method described in Section 3.1, which was specially developed for such cases was employed. The obtained masses in the spectrum shown in Fig. 3.17, agree within the error bars with the literature values. In figure 3.18, a zoom to the fit corresponding to the overlapping nuclei ^{133}Te and ^{133m}Te is shown.

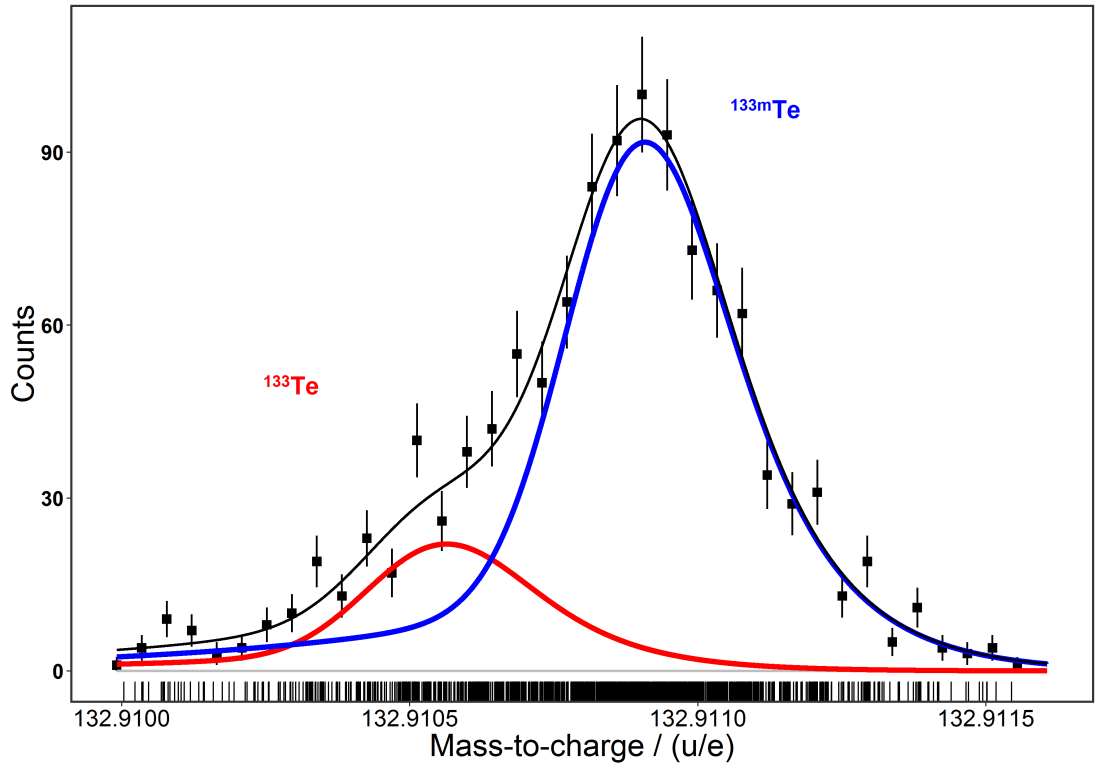

Figure 3.18: Detailed view in linear scale of the fit to the tellurium ground state and isomeric state (excitation energy of about 300 keV) data with two Hyper-EMG(1,1) functions. In black squares, the original data is presented with a bin size corresponding to the Freedman-Diaconis rule: twice the interquartile range of the data, divided by the cube root of the sample size [Freedman and Diaconis, 1981]. In black the sum of both Hyper-EMG functions, ^{133}Te in red and ^{133m}Te in blue. In the lower part, the original unbinned data events used for the fit are shown.

The next presented case consists is overlapping peaks with very low statistics, where the challenges presented for the data evaluation are even stronger. In Fig. 3.19, a spectrum taken with the MR-TOF-MS during the beamtime containing different ions of interest is shown. From this spectrum, the mass values and the uncertainties of ^{134}Te, ^{134}Sb and ^{134m}Sb were obtained.

For the Sb, only 25 counts in total were available and an isomeric state with an excita-

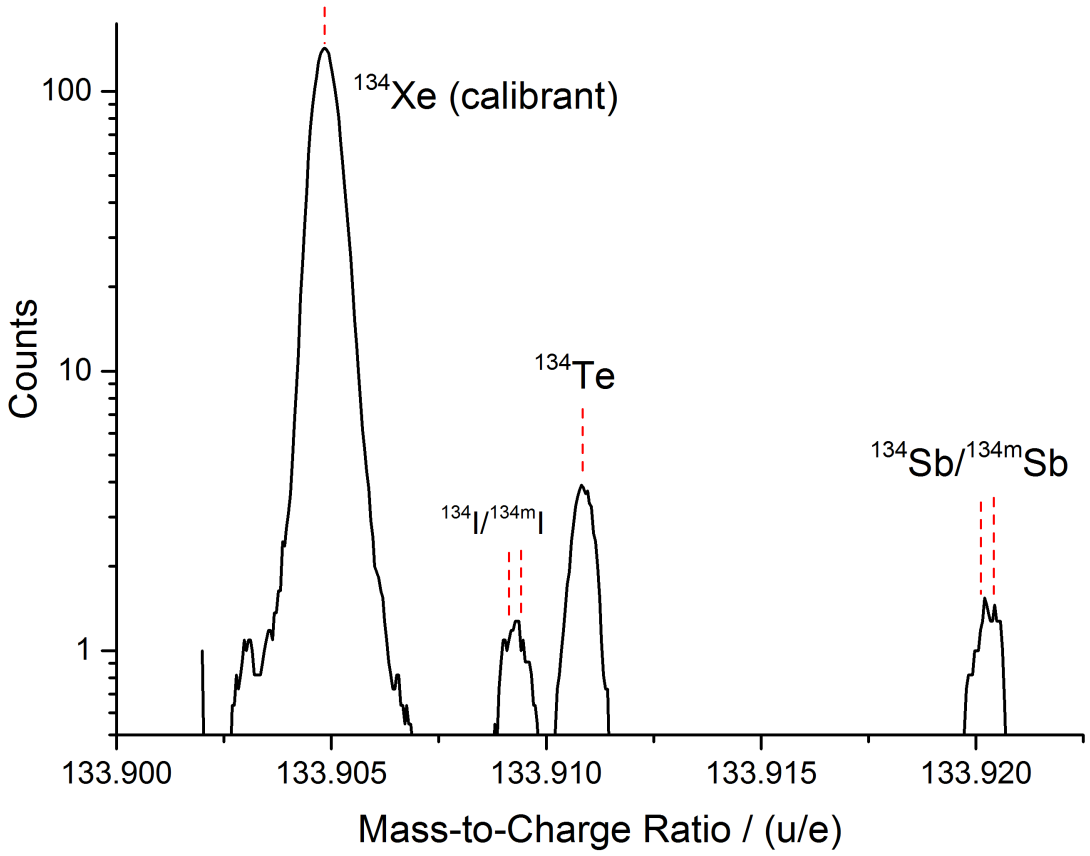

Figure 3.19: Spectrum taken with the MR-TOF-MS during the experiment in 2014. It is calibrated with ^{134}Xe. The isomers ^{134m}I and ^{134m}Sb have both an excitation energy of about 300 keV. In black the smoothed original data. In dashed red line, the approximate mass of the different nuclei.

tion energy of 279 keV is expected. A single peak fit to the data of ^{134}Sb and ^{134m}Sb with the peak shape parameters obtained from the calibrant peak as described in the previous section, revealed a mass value between the isomer and the ground state with a p-value obtained from the KS test of 0.29. In case of performing a double peak fit with two Hyper-EMG functions, a higher p-value of 0.42 and a mass value of the ground state and the isomeric state fitting with the literature mass were obtained, with relative uncertainties below 10^{-6} (see Fig.3.16 and Table 3.1). The result of the double Hyper-EMG fit to the data is shown in Fig. 3.20. This level of uncertainty with such a low number of events is only possible due to the high resolving power of the device and the data evaluation procedure developed to extract the masses and the uncertainties. This result clearly indicates the practical applicability and reliability of the method, which is mature for future experiments.

All the masses listed in the Tab. 3.1 have already been directly measured and the results were published in the AME16 [Huang et al., 2017]. Two nuclei from this table (^{133}I and ^{134}I) were first directly measured by a Penning trap [Van Schelt et al., 2013] only after the the publication of the AME12 [Audi et al., 2012], which contained indirect

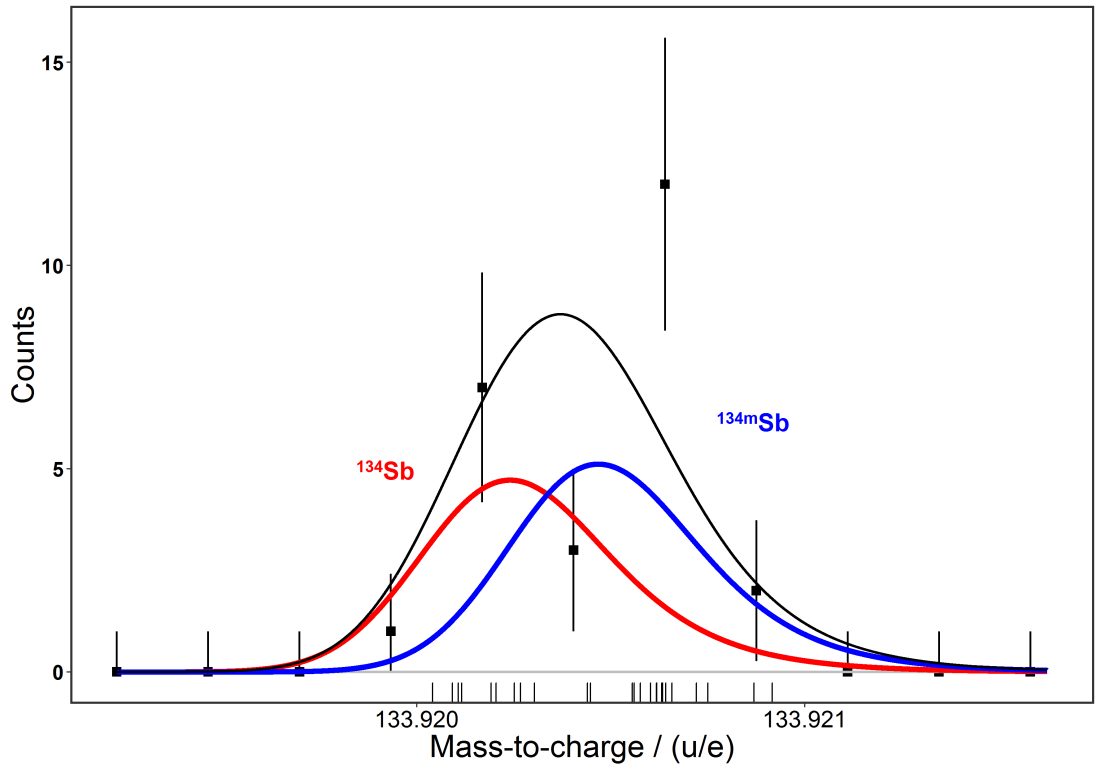

Figure 3.20: Detailed view of the ^{134}Sb (red) and ^{134m}Sb (blue) fits. The black line is the sum of both Hyper-EMG(0,1) functions used for the fit. In the lower part, the unbinned data events used for the fit are shown.

mass measurements of both nuclei.

For the ^{133}I and ^{134}I case, the mass published in AME03 [Wapstra et al., 2003] and AME12 [Audi et al., 2012] was determined by taking as reference ^{133}Cs and ^{134}Xe, respectively, and then extrapolating the mass by adding the total energy of the β reaction chain [Fogelberg et al., 1999]. A direct mass measurement from 2013 of ^{133}I and ^{134}I [Van Schelt et al., 2013] included later in the AME16, resulted in a change of the mass value by a factor of about 6 and 3 times the uncertainty presented from the previous indirect mass measurement [Fogelberg et al., 1999] for ^{133}I and ^{134}I, respectively. In Fig. 3.21 and Fig. 3.22, the mass excess published in the different Atomic Mass Evaluation for ^{133}I and ^{134}I, respectively, is summarized. The mass excess obtained in this work is also included.

The main change in both masses after the publication of the AME16 was due to a direct mass measurement of both nuclei [Van Schelt et al., 2013], setting the previous mass values off by more than the uncertainty of the indirect measurement results. This work presents clear agreement with the mass excess published in the AME16 for ^{134}I and specially for ^{133}I. With these examples, the importance of the direct mass measurements, even of nuclei which are relative close to the valley of stability, is clearly strengthened.

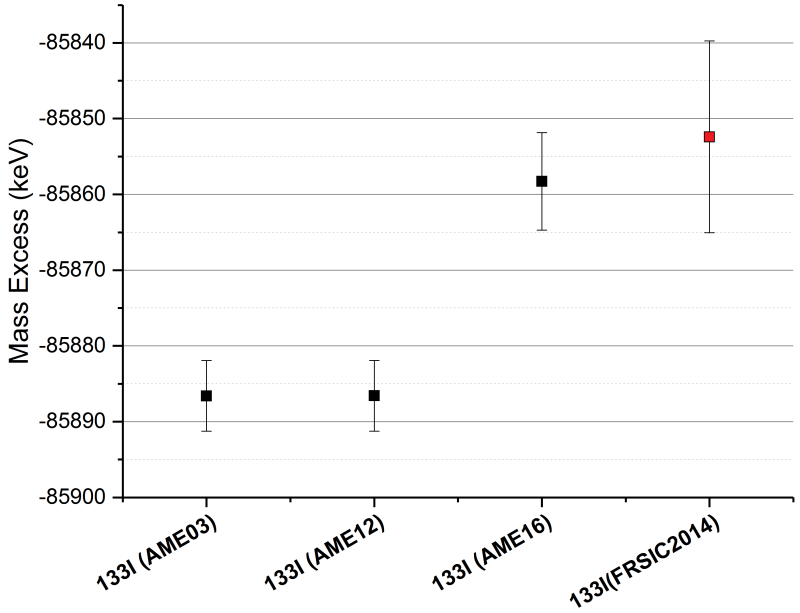

Figure 3.21: Published mass excess of ^{133}I in the AME03, AME12 and AME16 (black squares) and obtained in this work (red square). The first direct mass measurement was published in 2013 [Van Schelt et al., 2013] and included first in the AME16. The deviation between AME03 and AME16 is about 25 keV.

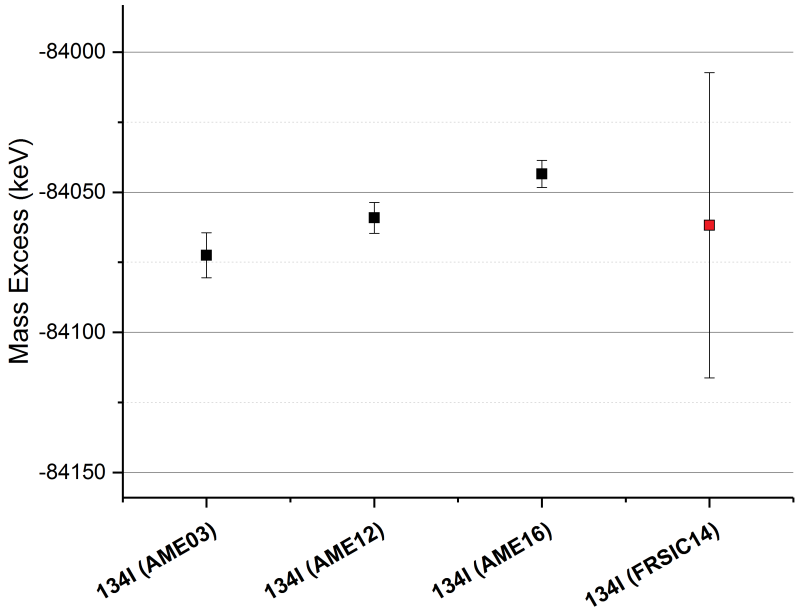

Figure 3.22: Published mass excess of ^{134}I in the AME03, AME12 and AME16 (black squares) and obtained in this work (red square). The data used for AME03 and AME12 is the same but with different weight. In this case the deviation is about 30 keV between AME03 and AME16.

During this experiment, masses of ^{238}U projectile fragments were measured as well with the MR-TOF-MS. The results from this set of data are part of another PhD thesis [Hornung, 2018].

3.1.4 Direct Mass Measurements of ^{238}U and ^{124}Xe Projectile Fragments

During the experiments at GSI in 2016, projectile fragments of ^{238}U at 300 MeV/u and of ^{124}Xe at 600 MeV/u were produced in a beryllium target, range bunched and separated in the FRS, stopped in the CSC and transferred to the MR-TOF-MS for direct mass measurements. The data evaluation process for the determination of the masses and uncertainties was the same as the one used for evaluating the data of the experiment presented in the previous section. In Fig. 3.23 the deviations between the masses obtained in this work and the literature values [Huang et al., 2017] are shown.

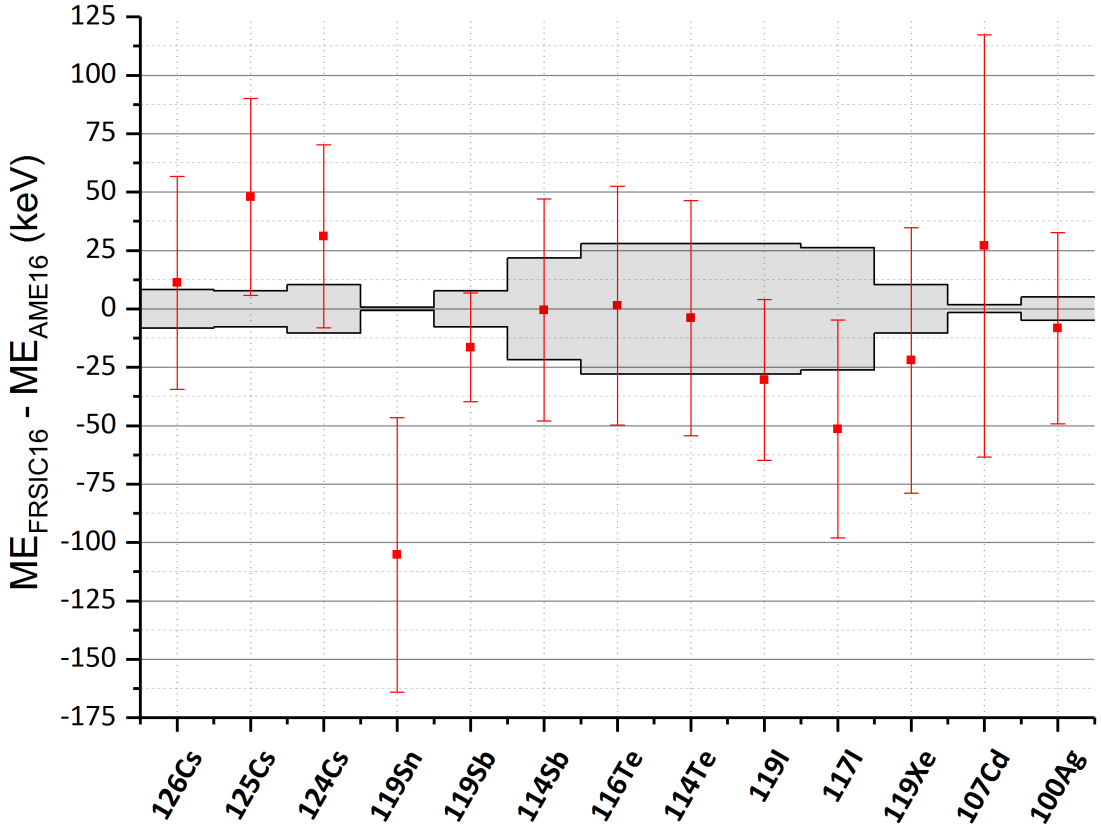

Figure 3.23: The mass excess deviations between the experimental results obtained with the MR-TOF-MS during the experiment in 2016 and the literature values are shown. The error bars shown are the total errors presented in Tab. 3.3. In grey area, the AME16 error is represented.

The improvements presented in Chapter 2 were all ready and implemented in the system for this experiment. A rich variety of projectile fragments were measured during the experiment. The fragments presented in the context of this work are: ^{126}Cs, ^{125}Cs, ^{124}Cs, ^{119}Sn, ^{119m}Sn, ^{119}Sb, ^{114}Sb, ^{116}Te, ^{114}Te, ^{119}I, ^{117}I, ^{119}Xe, ^{107}Cd and ^{100}Ag. All the evaluated fragments from this experiment of which the obtained mass has a relative uncertainty exceeding 10^{-6} are not presented in this thesis. The shortest-lived nuclei presented in this section is ^{126}Cs, with a half-life of 1.64 minutes. Mass resolv-

ing powers of 450000 were routinely obtained, but the data was taken with medium and high turn numbers, resulting in resolving powers ranging from 150000 to 450000. The measured masses agree with the literature values within the uncertainties. In this experiment, calibration with isobars and ions with different turn numbers in the analyzer had to be performed. Different calibration sources, including molecular ions, were used. In particular, ionized fragments of octafluoropropane (C_3F_8) produced in the MR-TOF-MS by the electron impact source, ^{133}Cs ions from a thermal ion source and molecules ionized in the CSC by the incoming beam from the FRS, like $^{84}Kr^{14}N_2$. The amount of ionized molecules in the CSC was reduced in some cases (only for the measurements of ^{107}Cd and ^{100}Ag) by the use of the collision induced dissociation (CID) method for obtaining an optimum rate for the calibrant [Greiner, 2017]. The contributions to the mass uncertainty taken in account for these experiments are, as in the experiment in 2014 (statistical error, peak shape error, bias correction error for overlapping peaks, calibrant error and TRC error), and due to the characteristics of the data obtained in these experiments, other sources of error had to be considered. The non-ideal ejection error was no longer a negligible contribution due to the higher parameter $\Delta_{tNIE} = 0.5$ ns and the shorter flight times of some of the data taken. Moreover, since the calibrant was not always an isobar, the error of the calibration parameter c had to be taken into account in those measurements where the calibration was not performed with an ion within the same turn number as the IOI. Also, the MRS error had to be taken into account where the MRS state was not always the same for the calibrant and the IOI. The unresolved peaks error had also to be taken in account due to the existence of overlapping peaks of class D and background peaks close to the IOI. The higher background was caused by the higher rate of ions injected in the CSC, about 50000 ions per second, of which about 5 % corresponded to the IOI. In addition to the higher background generated in the CSC, the MRS was in most of the cases isolating isobars of several different mass numbers, accentuating the background in the spectrum. In the Tab. 3.3 a summary of the masses obtained during the experiment is shown. The individual contributions to the total uncertainty are presented in Tab. 3.4.

Nuclei	Mass$_{FRSIC16}$ (u)	ME$_{FRSIC16}$ (keV)	Δ_{ME} (keV)	Calibrant
^{124}Cs	123.912291 (42)	-81700 (39)	31 (40)	^{124}Xe
^{125}Cs	124.909779 (45)	-84040 (42)	48 (43)	^{126}Xe
^{126}Cs	125.909458 (49)	-84340 (46)	11 (47)	^{126}Xe
^{119}Sn	118.903198 (63)	-90170 (58)	-105 (58)	$^{12}C_2$ $^{19}F_5$ (A=119)
^{119m}Sn	118.903294 (63)	-90081 (58)	-105 (58)	$^{12}C_2$ $^{19}F_5$ (A=119)
^{119}Sb	118.903928 (25)	-89491 (23)	-16 (25)	$^{12}C_2$ $^{19}F_5$ (A=119)
^{114}Sb	113.909289 (51)	-84497 (47)	1 (52)	$^{12}C_2$ $^{19}F_5$ (A=119)
^{116}Te	115.908462 (55)	-85268 (51)	0 (49)	$^{12}C_2$ $^{19}F_5$ (A=119)
^{114}Te	113.912085 (54)	-81893 (50)	4 (58)	$^{12}C_2$ $^{19}F_5$ (A=119)
^{119}I	118.910041 (37)	-83796 (34)	-30 (44)	$^{12}C_2$ $^{19}F_5$ (A=119)
^{117}I	116.913593 (50)	-80488 (47)	-53 (45)	$^{12}C_2$ $^{19}F_5$ (A=119)
^{119}Xe	118.915387 (61)	-78816 (57)	-22 (58)	$^{12}C_2$ $^{19}F_5$ (A=119)
^{107}Cd	106.906641 (97)	-86963 (90)	27 (90)	^{84}Kr $^{14}N_2$ (A=112)
^{100}Ag	99.916107 (44)	-78146 (41)	-8 (41)	$^{12}C_2$ $^{19}F_4$ (A=100)
^{100m}Ag	99.916123 (44)	-78131 (41)	-8 (41)	$^{12}C_2$ $^{19}F_4$ (A=100)

Table 3.3: Results of the direct mass measurement from the FRS-Ion Catcher experiments in 2016 with ^{238}U and ^{124}Xe projectile fragments, including the atomic mass, mass excess, mass excess deviation (Δ_{ME} = ME$_{FRSIC16}$ - ME$_{lit}$) and the calibrant used. The uncertainties from the table correspond to the total experimental uncertainties.

Nuclei	Statistical ($\cdot 10^{-7}$)	Peak Shape ($\cdot 10^{-7}$)	Bias ($\cdot 10^{-7}$)	Calibrant ($\cdot 10^{-7}$)	MRS ($\cdot 10^{-7}$)	Unresolved Peaks ($\cdot 10^{-7}$)	TRC ($\cdot 10^{-7}$)	Δc ($\cdot 10^{-7}$)	NIE ($\cdot 10^{-7}$)	Total Rel. ($\cdot 10^{-7}$)	Total Abs. (μu)
^{124}Cs	3.1	0.1	0	1.1	0	0	0	0	0.7	3.4	42
^{125}Cs	1.2	0.2	0	1	0	1.4	2	0	2.2	3.6	45
^{126}Cs	3.7	0.1	0	1	0	0	0	0	0.7	3.9	49
^{119}Sn	3.3	0.1	2.1	0.2	0	3.4	0.7	0	0.5	5.3	63
^{119m}Sn	3.3	0.1	2.1	0.2	0	3.4	0.7	0	0.5	5.3	63
^{119}Sb	1.2	0.2	0.1	0.2	0	1.4	0.7	0	0.5	2.1	25
^{114}Sb	1.8	0.8	0	0.9	0	2.6	1	1.7	2.1	4.5	51
^{116}Te (1)	1.8	0.2	0	1.8	0	3.6	1.5	2.6	2.1	5.7	66
^{116}Te (2)	1.5	0.1	0	1.5	0	3.4	1.6	1.6	2.1	5.1	59
^{114}Te	1.8	0.9	0	0.9	0	3	1	1.7	2.1	4.7	54
^{119}I	2.2	0.2	0.1	0.2	0	2	0.7	0	0.5	3.1	37
^{117}I (1)	2.1	0	0	1.8	0	3.6	1.4	1.3	2.2	5.4	63
^{117}I (2)	1.5	0.2	0	1.5	0	2.7	1.5	0.9	2.1	4.4	51
^{119}Xe	3.4	0.2	0	0.2	0	3.8	0.7	0	0.5	5.1	61
^{107}Cd	2.3	0.1	0	0.7	5.2	2.3	3	5.2	2.8	9.1	97
^{100}Ag	3.2	0.1	0	0.2	0	2.9	1.5	0	0.5	4.4	44
^{100m}Ag	3.2	0.1	0	0.2	0	2.9	1.5	0	0.5	4.4	44
AVG.	**2.4**	**0.2**	**0.3**	**0.8**	**0.3**	**2.5**	**1.1**	**0.9**	**1.3**	**4.7**	**54**

Table 3.4: Individual relative contributions to the total uncertainties for the measured fission fragments with the MR-TOF-MS. For the definition of each error contribution see Section 3.1.1.1 and Section 3.1.1.2. Also, the total absolute uncertainty is included. The numbers in brackets in the first column represent different measurements of the same nuclei. The NIE error of ^{107}Cd has an additional contribution due to being close to the mirror during ejection, see. Fig. 3.5.

In average, the main contributions to the total mass uncertainty are the unresolved peaks and the statistical error contributions. The unresolved peaks contribution was high due to the challenging conditions presented during these experiments. In 2016, the background-to-IOI ratio delivered from the FRS was about 1000 times higher than in 2014. In addition, most of the measurements were taken with the MRS including several mass unit at the same time. Only the measurements corresponding to the nuclei ^{124}Cs and ^{126}Cs were with narrow MRS, presenting a total mass uncertainty dominated by the statistical error.

All the presented nuclides with A = 119 were acquired at once in the same measurement and calibrated with a molecular isobar $^{12}C_2$ $^{19}F_5$. A brief description of the mass measurements performed to the different A = 119 isobars is given in the following.

- ^{119}Sb, ^{119}Sn and ^{119m}Sn

The nuclei ^{119}Sb overlaps with the ground state and the isomeric state of ^{119}Sn as shown in Fig. 3.24.

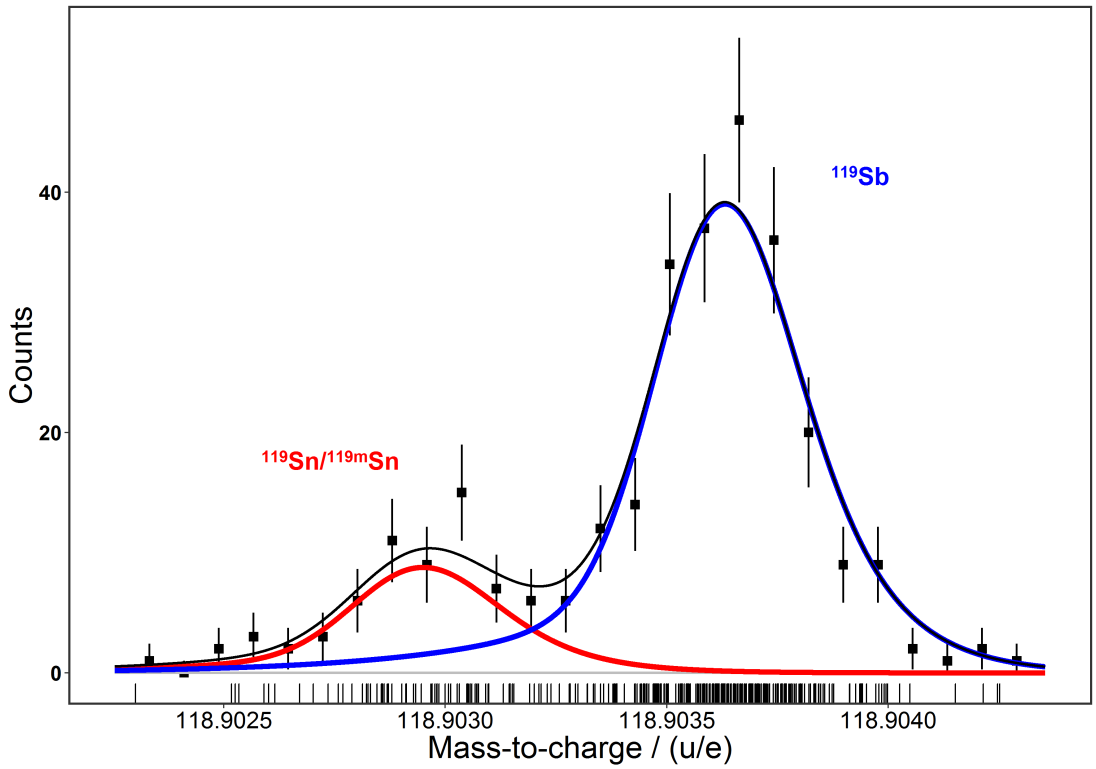

Figure 3.24: Fitted spectrum with the data corresponding to ^{119}Sn, ^{119m}Sn and ^{119}Sb is shown. In red, the fitted Hyper-EMG corresponding to the ^{119}Sn and ^{119m}Sn, considered as a single peak due to the low excitation energy (89.5 keV) compared with the typical peak's FWHM (about 350 keV). In blue, the fitted Hyper-EMG corresponding to the ground state of the Sb. In black, the sum up of both fitted Hyper-EMGs. In black squares, the original data binned and in the lower part of the y-axis, the original unbinned data.

The nuclide ^{119m}Sn is about 500 keV separated from the ^{119}Sb, classificated as a resolved overlapping peak (class B), see Section 3.1.1.2. The data was fitted using a double Hyper-EMG function, where the ^{119}Sn and ^{119m}Sn were considered as a single peak due to the low excitation energy (89.5 keV), much lower than the peak's full width at half maximum (around 350 keV). The mass of ^{119}Sb published by the AME16 was obtained by an indirect mass measurement. In this case, the reaction (^{3}He, d) on ^{118}Sn was used for the determination of the mass value [Ishimatsu et al., 1967]. The presented mass is in agreement with the literature value within the error bars (see Fig. 3.23). The isomeric state, ^{119n}Sb, is estimated to be less than 20 keV above the 2841.7 keV energy level [Audi et al., 2017] and is also seen in the spectrum. It will be analyzed in the context of another work.

- ^{119}I

The nuclide ^{119}I does not overlap strongly with any peak as the previous ones and no isomer is expected. Nevertheless, some resolved but unknown contaminant lies close to it, at a distance of about 600 keV. To avoid any bias on the mass value of ^{119}I by the unidentified peak, a double peak fit was employed to obtain the mass of ^{119}I.

- ^{119}Xe

For this nuclei only 27 counts were available in the spectrum. A single Hyper-EMG function was fitted to the data and a mass uncertainty below $\pm$60 keV was obtained.

The spectrum obtained for the mass measurement of ^{100}Ag is shown in Fig. 3.25. In this case, two molecular isobaric calibrants were available, $^{12}C_2$ $^{19}F_4$ produced in the electron impact ion source of the MR-TOF-MS and ^{84}Kr^{16}O, produced in the CSC by ionization of the buffer gas contaminants. For the ^{100}Ag nuclei, an isomer is expected with a known excitation energy, 15.52$\pm$0.16 keV. This excitation energy is much lower than the peak's full width at half maximum (around 300 keV). A single peak fit was performed and the unresolved peaks method for obtaining the mass value of ^{100}Ag and ^{100m}Ag, explained in the previous section, was applied.

All the masses measured directly with the MR-TOF-MS at the FRS-Ion Catcher presented in this thesis have been previously measured and published with an average uncertainty below 10 keV. Therefore, all the mass measurements performed in 2014 and 2016 and listed in Tab. 3.1 and Tab. 3.3, respectively, can be used as references to test possible systematic shifts and possible unknown systematic mass uncertainties. In addition, other 7 known masses obtained during these experiments with the same procedure as presented here, and published in another thesis [Hornung, 2018], were included to obtain Fig. 3.26, where a compilation of all the difference between the

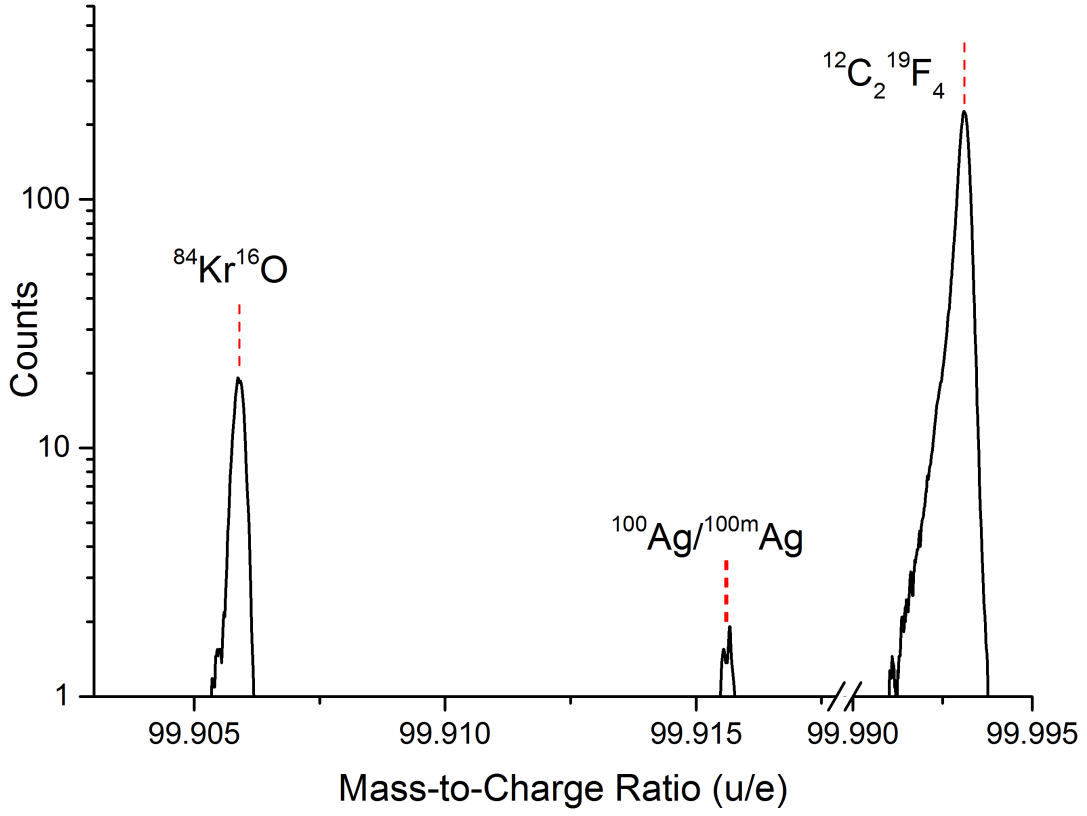

Figure 3.25: Spectrum showing the data obtained for the mass measurement of ^{100}Ag. In black the smoothed original data. The red dashed lines mark the approximate position of the peaks. The isomer ^{100m}Ag has an excitation energy of only 15.52 keV.

masses obtained with the MR-TOF-MS of the FRS-Ion Catcher in this and other thesis and the literature masses is shown. A Gaussian function fitted to the histogram shows no systematic deviation from the literature values, with a center of $\mu = 4.3 \pm 2.5$ keV and a standard deviation $\sigma = 29 \pm 2.5$ keV. The Birge ratio [Birge, 1932] of the mass difference from the literature value for all the known measured masses in the FRS-Ion Catcher presented in this and other thesis [Hornung, 2018] was calculated and a value of 0.885 was obtained. This shows that the different sources of uncertainty here presented (see Fig. 3.12), describe the total uncertainty and no unknown systematic error needs to be added.

A total of 25 masses of unstable nuclei were measured in the FRS-Ion Catcher during three experiments in 2014 and 2016 and presented in this thesis, of which 7 correspond to isomeric states with excitation energies below 300 keV. Nuclides of 8 different elements with half-lives down to 300 ms were measured in this work with an average relative uncertainty of $4.7 \cdot 10^{-7}$. The minimum obtained relative uncertainty with the MR-TOF-MS in this work is of $1.1 \cdot 10^{-7}$ and of about $6 \cdot 10^{-8}$ in another work [Hornung, 2018], demonstrating the competitiveness for measuring the mass of short-

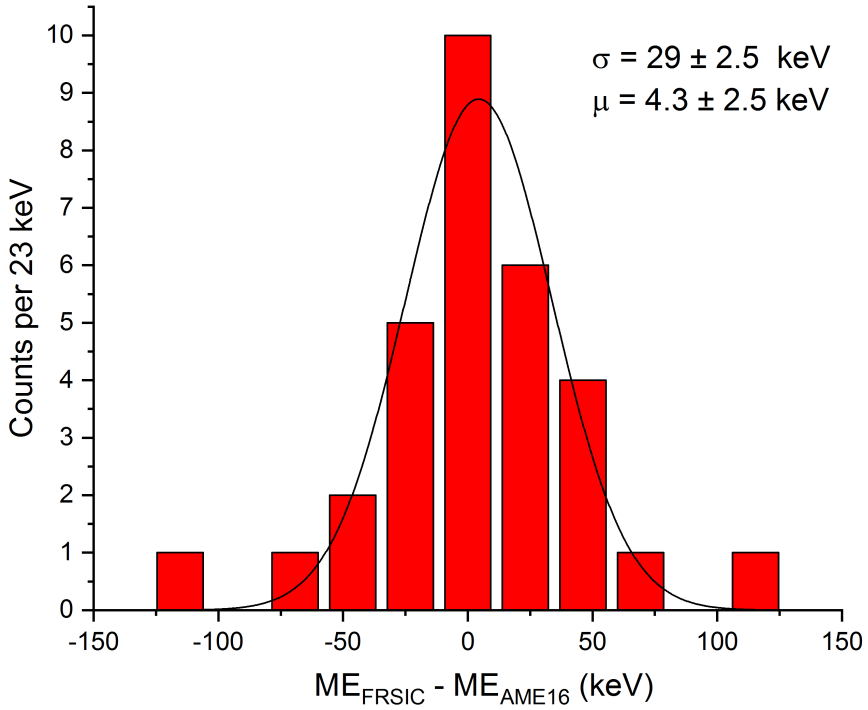

Figure 3.26: Histogram of the difference between the masses measured directly with the MR-TOF-MS of the FRS-Ion Catcher presented in this and other thesis [Hornung, 2018] and the literature values. In black, a fitted Gaussian function with a center of $\mu = 4.3 \pm 2.5$ keV with a standard deviation $\sigma = 29 \pm 2.5$ keV was obtained, showing no systematic shift.

lived nuclei with high accuracy to extract information for the field of nuclear physics and nuclear astrophysics. Identification of uranium molecules and fragments were performed as result of the unique combination of high resolving powers with a broadband mass range. It is the first time these measurements and their precision became possible after the major improvements developed and implemented in the present work: increase in kinetic energy and repetition rate, improved stability and reliability and improvement of the cleanliness of the gas. This opens the door for measurements of so far unknown masses with a precision which was up to now restricted to Penning traps; it is an important result of the present work that this precision can be reached also with the MR-TOF-MS. Furthermore, after the understanding and characterization of the error contributions, a relative uncertainty in the range of few 10^{-8} is within reach with improved conditions during the mass measurement: isobaric continuous calibration provided by a newly designed laser ablation carbon cluster ion (LACCI) source included in the upgraded RFQ beamline between the CSC and the MR-TOF-MS [Hornung et al., 2018], the MRS will isolate the masses minimizing the disturbances [Bergmann et al., 2018], and the resolving power will be further increased by means

of an improved optical tuning as well as improved stability of the voltages supplied to the analyzer.

3.2 Experiment in an ISOL Facility

The achievements of the previous chapter and part of the developments mentioned in Section 2.3.2 were transferred to another MR-TOF-MS developed and built in the Justus-Liebig University in Gießen [Jesch et al., 2015, Jesch, 2016] and installed in TITAN (TRIUMF′S Ion Trap for Atomic and Nuclear Science) at TRIUMF (Canada's National Laboratory for Particle and Nuclear Physics, Canada). With these improvements, direct mass measurements of Gallium isotopes were performed. The data evaluation procedure employed will be introduced as well. This data evaluation procedure is a simplified version of the one presented in the last section. The isotope separation on-line (ISOL) facility (production, separation, transport...) will be first introduced, where special attention will be given to the MR-TOF-MS. A description of the obtained results and the astrophysical impact of the newly measured masses in a light r-process will be discussed in the following.

A high energy proton beam of up to 100 μA with an energy of up to 500 MeV from TRIUMF's main cyclotron is delivered to the Isotope Separator and Accelerator facility (ISAC) [Dombsky et al., 2000], an ISOL type RIB facility (see Fig. 3.27), where it will impinge on a target (UCx, tantalum, ...). The interaction between the high energetic protons and the nucleus from the target generates via nuclear spallation the exotic nuclei, which are then stopped in the target and extracted via diffusion.

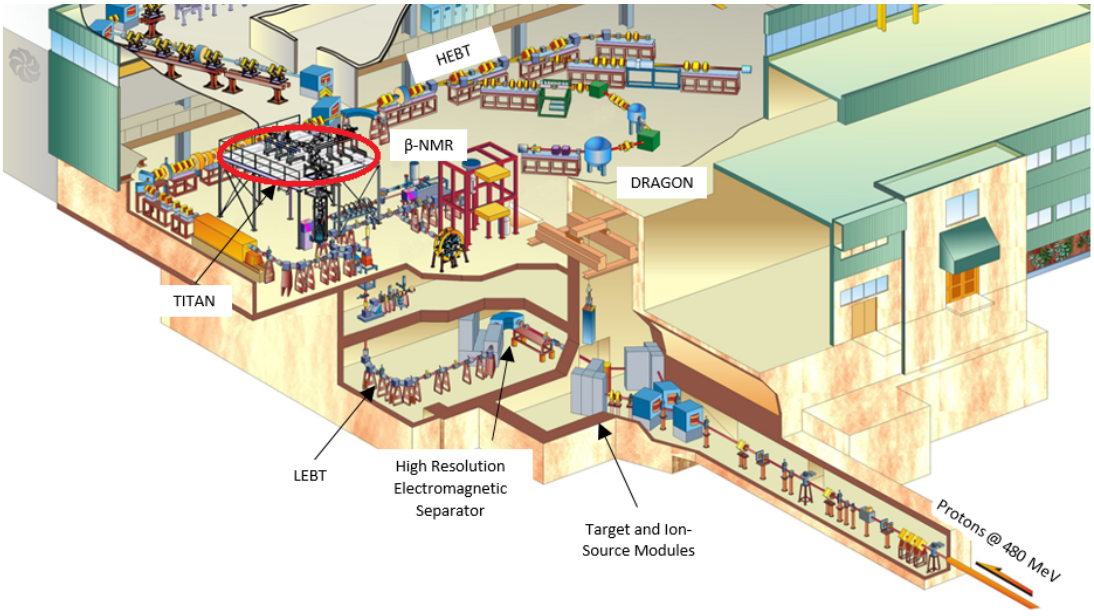

Figure 3.27: Layout of the ISAC facility. The proton beam is delivered by the main cyclotron, not included in the picture [Jesch, 2016]. The TITAN experiment is marked with a red circle.

The ionization method employed as well as the material of the target will be selected depending on the chemical properties of the element of interest. The ionized particles are then extracted at energies of tens of keV towards the ISAC electromagnetic separator [Bricault et al., 2014], which has a resolving power ($\frac{\Delta_m}{m}$) of about 2000. Then, are transported over the low energy beam transport (LEBT) line and delivered to the experiments, such as TITAN [Dilling et al., 2006]. Here, the ions are first cooled and bunched in the TITAN RFQ [Brunner et al., 2012] and ejected towards the systems in the TITAN platform (see Fig. 3.28).

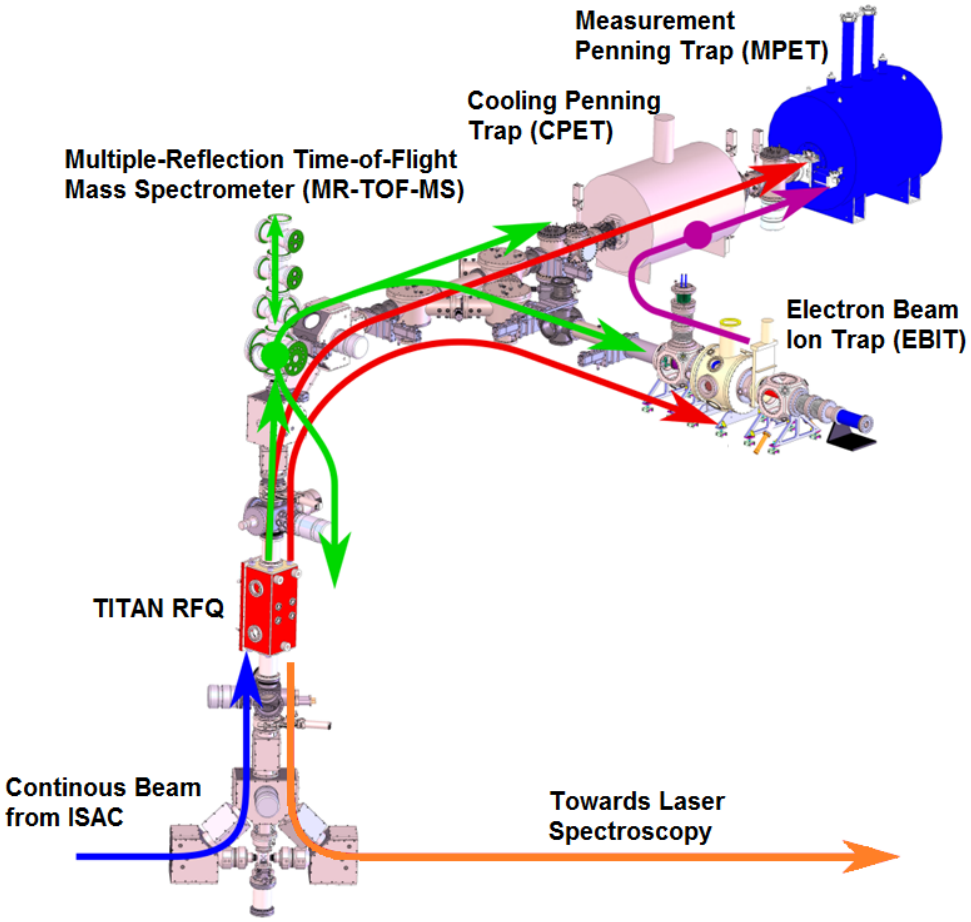

Figure 3.28: Drawing of the TITAN experiment including the recently installed MR-TOF-MS [Jesch, 2016]. The arrows show the possible beam manipulation and transport paths between the experiments. The blue arrow indicates a continuous beam delivered from the ISAC facility. The orange arrow corresponds to the transport of bunched beam to the laser spectroscopy station. The green arrows represent the MR-TOF-MS used as isobar separator, which can forward the isobarically clean beam to the EBIT, CPET, MPET or back to the TITAN RFQ. The red arrows correspond to the direct delivery of cooled and bunched beam to the EBIT or MPET. The purple arrow represents the transport of highly charged ions between EBIT and the penning traps.

The ions are ejected from the TITAN RFQ at a reference potential similar to the one of the source (20 keV) with a kinetic energy of about 1.35 keV. When the ions are inside a pulsed drift tube located after the RFQ, the potential of the drift tube is changed to ground, shifting the reference potential of the ions to ground without changing their kinetic energy. Then the ions can be forwarded to the MR-TOF-MS, which is located in the TITAN platform [Jesch et al., 2015] in straight direction from the RFQ (see Fig. 3.29).

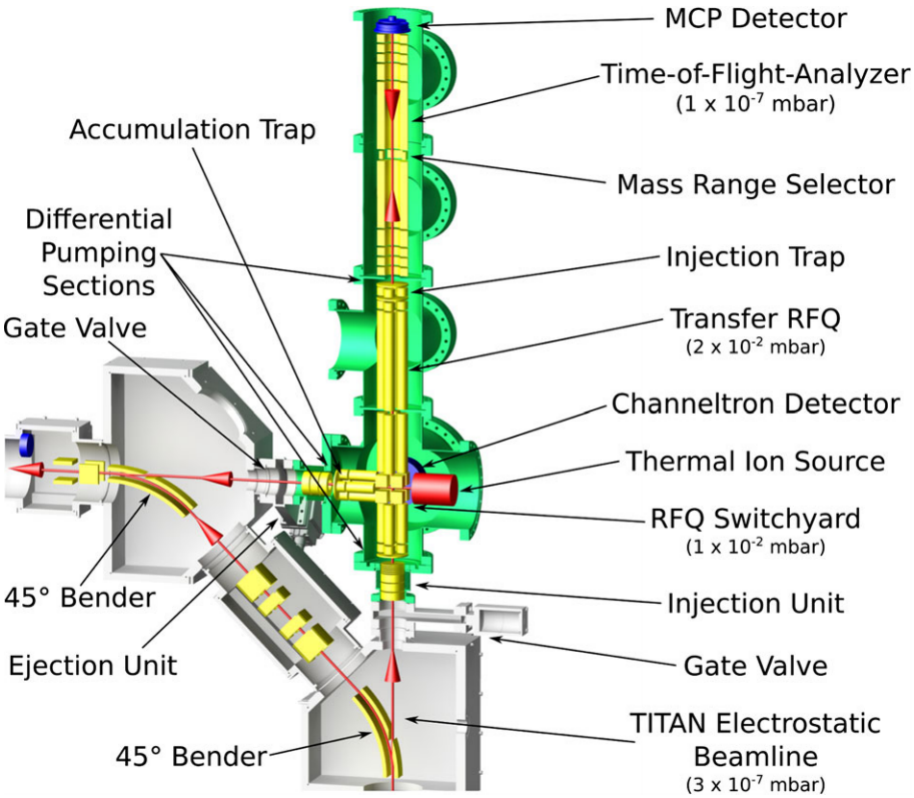

Figure 3.29: Detailed view of the MR-TOF-MS included in the TITAN platform [Jesch, 2016]. Incoming beam from the bottom, cooled and bunched by the TITAN's RFQ. Ions from the TITAN's RFQ are merged with some calibrant ions in the switchyard and transported over the RFQs to the injection trap. Then, the ions are injected into the analyzer for spatial separation to perform a mass measurement or to obtain a isobarically clean beam.

Besides straight direction form the RFQ, the ions can be guided directly towards other TITAN systems in the platform, such as the cooling penning trap (CPET), the measurement penning trap (MPET) and the electron beam ion trap (EBIT). The MR-TOF-MS is a new device included in the TITAN platform since the beginning of the second quarter of 2017. From the developments presented in the last chapter, the improvements for the stability and reliability were included in the MR-TOF-MS: the new stabilization box for the analyzer and new developed pulsers for the beamline. The improved buffer gas cleanliness is in preparation. A first commissioning beam-

time with the Off-Line Ion Source (OLIS) was performed one month after installation [Will, 2017]. The first experiment with radioactive beam was performed on May 2017. In this first experiment, the MR-TOF-MS helped to establish the onset of a shell closure at N = 32 via high precision mass measurements of neutron-rich titanium isotopes [Leistenschneider et al., 2018]. The results presented in the next section correspond to the second experiment with radioactive beam of the MR-TOF-MS in the TITAN platform.

The MR-TOF-MS for TITAN is a spin-off of the one from the FRS-Ion Catcher. It is originally designed for isobar separation but can be used for mass measurements as well. This novel device was integrated in the already existing TITAN experiment. Therefore, it exhibits key differences from the MR-TOF-MS of the FRS-Ion Catcher listed as follows:

- The length of the analyzer is reduced because of space constraints. Also, there is no space for the integration of a time focus shift (TFS) reflector. The TFS of the ions to the detector plane is performed dynamically by changing the mirror voltages for one turn [Dickel et al., 2017b].

- Ions are injected from TITAN's RFQ into the MR-TOF-MS through the injection unit at an energy of about 1.3 keV. Since the ions are already delivered at the desired potential, no potential lift is needed in this system and therefore, the whole beamline of the MR-TOF-MS (from the injection unit to the injection trap) has to be referenced to a potential of 1.3 kV, including the RFQs, switchyard, sources, etc.

- This MR-TOF-MS is designed to provide an isobaric clean beam by retrapping the isobar of interest in the injection trap and deliver it via the accumulation trap to the other systems in the TITAN platform. This is achieved by retrapping the ions in the injection trap after a previous spatial separation [Dickel et al., 2017a]. Then, the retrapped ions are transported towards the accumulation trap by changing the transport direction of the RFQs and the switchyard.

Although designed for isobaric separation, the presented developments allow to increase the resolving power and precision and therefore perform direct mass measurements of very short-lived nuclei.

3.2.1 Direct Mass Measurements of Neutron-Rich Ga Isotopes

In June 2017, the second experiment with the TITAN's MR-TOF-MS at TRIUMF was performed. The masses of neutron-rich gallium isotopes, ^{80}Ga to ^{85}Ga, were

measured. In this experiment, a proton beam of 10 μA with an energy of 480 MeV from TRIUMF's main cyclotron was delivered to the ISAC facility and impinged on a uranium carbide target (UCx). An ion-guide laser ionization source (IG-LIS) [Raeder et al., 2014] was used. Surface ionized ions were suppressed by applying an electrostatic barrier to lower the isobaric contamination. Neutral gallium atoms diffusing out of the hot UCx target were not affected by the electrostatic barrier and were ionized via resonant laser ionization behind the electrostatic barrier inside a radio frequency quadrupole (RFQ), set to a potential reference of 20 kV. The different isotopic chains of mass numbers A = 80 to A = 85, were individually selected by the ISAC electromagnetic separator and transported towards the MR-TOF-MS through the low energy beam transport (LEBT) and TITAN's RFQ cooler and buncher. The first turn (2 reflections) of the ions inside the analyzer was used to perform a dynamic time focus shift (TFS) [Dickel et al., 2017b] of the ions on the detector. Afterwards, a certain number of isochronous turns (IT) were performed to increase the flight path, obtaining mass resolving powers ($\frac{\Delta m}{m}$ FWHM) of about 200000. The TOF between injection of the ions into the analyzer and arrival to the MCP, was recorded with a time-to-digital converter (TDC), model Ortec-9353, controlled by the MAc software. The data analysis for this experiment was the same as for the first experiment of the MR-TOF-MS at TITAN [Leistenschneider et al., 2018]. This is a simplified version of the introduced process to analyze the data from the experiments with the FRS-Ion Catcher. The preparation of the data in MAc was perform as explained in Section 3.1. The reference nuclei were always isobars delivered from the IG-LIS source together with the neutron-rich gallium isotopes. After preparing the data with MAc, fits to the data were done using least-square fits with the Levenberg-Marquardt algorithm as iteration algorithm, using a commercial data analysis software (*OriginPro*). Two independent evaluations of the same data were performed using different peak shapes for the fit: Gaussian (this work) and Lorentzian (performed by M.P. Reiter at TRIUMF, Canada [Reiter, 2018]). The deviation between the mass excess obtained with Gaussian and Lorentzian peak shape and the literature value [Huang et al., 2017] is shown in Fig. 3.30.

The peak shape parameters were obtained from the isobaric calibrants, fixed and used without any scaling for fitting the corresponding gallium isotope of interest. With the fit of the isobaric calibrant, a precision calibration factor of $(\frac{m_{CAL-LIT}}{m_{CAL-Origin}})$ was obtained, where $m_{CAL-LIT}$ is the literature mass of the calibrant published in the AME16 and $m_{CAL-Origin}$ is the mass value obtained by the fit to the isobaric calibrant. The fitted mass value of the gallium isotopes was then multiplied by the corresponding precision calibration factor to obtain the final mass value. The mass uncertainty of the calibrant is the square root of the sum of the squares of the standard error of the fit given by Origin, the statistical uncertainty, $\frac{\sigma}{\sqrt{N_{CAL}}}$ for the Gaussian distribution, where σ is the standard deviation and N the number of events and the literature error [Huang et al., 2017]. In

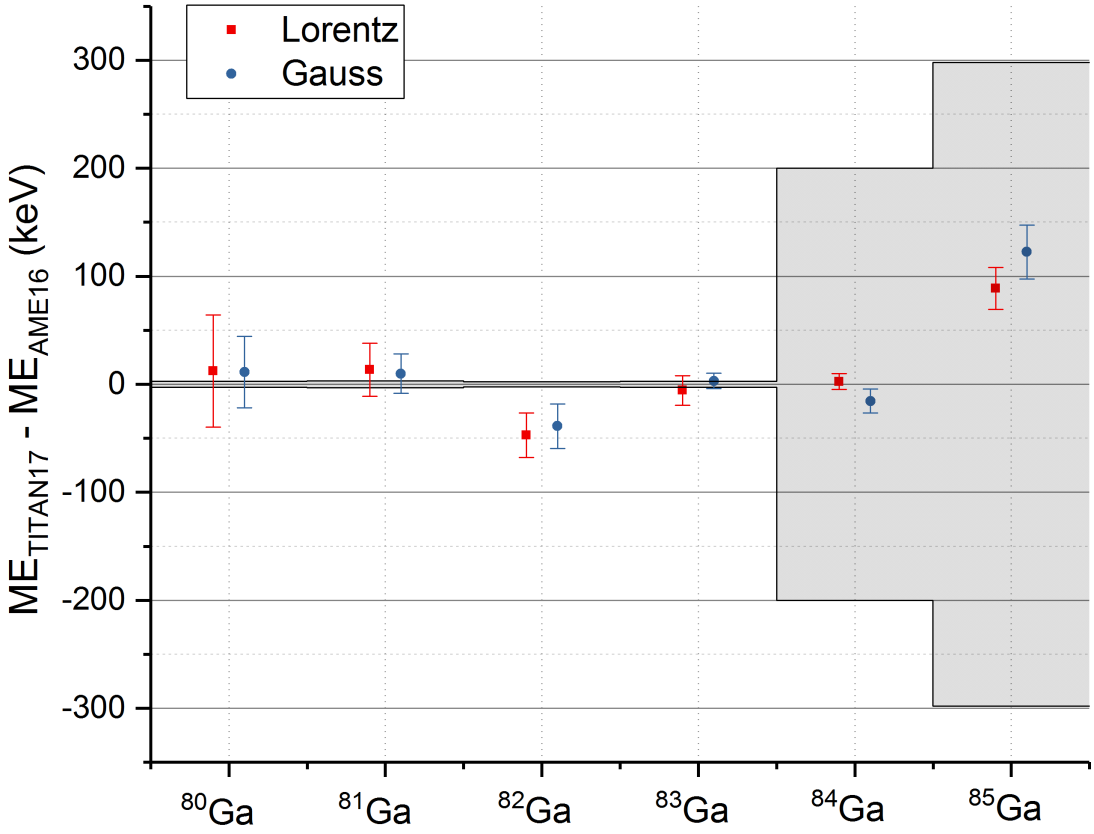

Figure 3.30: In blue circles and red squares, the mass excess deviation of the results obtained by the evaluation performed with Gaussian and Lorentzian [Reiter, 2018] functions, respectively, from the literature values [Huang et al., 2017] is presented. The error bars correspond to the errors listed in Tab. 3.5, which corresponds to the error from the fit obtained in Origin added in quadrature with the statistical error without including the systematic uncertainty. In grey area, the uncertainty of the AME16 is represented.

the uncertainty of the gallium masses, the uncertainty of the calibrant, calculated as mentioned before, was quadratically added to the uncertainty of the gallium mass, obtained also as the uncertainty given by the fit quadratically added to the statistical uncertainty of the gallium peak. An extra relative systematic uncertainty of $3 \cdot 10^{-7}$ was quadratically added after the combination of both evaluations. This systematic contribution was evaluated with off-line [Will, 2017] as well as with on-line measurements [Leistenschneider et al., 2018]. It is dominated by the effect of pulsing the analyzer electrodes when ejecting the ions (non-ideal ejection) and the effect of a non-perfect time resolved calibration. It represents an upper limit of the systematic uncertainty of the instrument. There is excellent agreement between the two independent evaluations, showing no systematic error due to the use of a different peak shape with the data at hand, where no class C overlapping peaks are fitted (see Overlap Classification). Also, there is agreement with previous directly measured masses (^{80}Ga to ^{83}Ga).

The masses of ^{84}Ga and ^{85}Ga, with half-lives of 85 ms and 92 ms, respectively, have only been estimated before. This presents the first mass measurement of these nuclides and a publication is pending [Reiter et al., 2018]. The mass values obtained by both evaluations are shown in Tab. 3.5.

Nuclei	Mass (u)	Mass Excess (keV)	Calibrant	Fit Function
^{80}Ga	79.936434 (56)	-59211 (52)	^{80}Ge	Lorentz
	79.936433 (36)	-59212 (33)	^{80}Ge	Gauss
^{81}Ga	80.938148 (26)	-57615 (24)	^{81}Br	Lorentz
	80.938144 (20)	-57618 (18)	^{81}Br	Gauss
^{82}Ga	81.943126 (22)	-52978 (21)	^{82}Rb	Lorentz
	81.943135 (22)	-52970 (21)	^{82}Rb	Gauss
^{83}Ga	82.947114 (15)	-49263 (14)	^{83}Rb	Lorentz
	82.947124 (8)	-49254 (7)	^{83}Rb	Gauss
^{84}Ga	83.952673 (8)	-44085 (7)	^{84}Rb	Lorentz
	83.952653 (12)	-44103 (11)	^{84}Rb	Gauss
^{85}Ga	84.957315 (21)	-39761 (19)	^{85}Rb	Lorentz
	84.957352 (27)	-39727 (25)	^{85}Rb	Gauss

Table 3.5: Results of direct mass measurements of gallium isotopes obtained with the TITAN's MR-TOF-MS in an experiment in 2017 evaluated with Gaussian and Lorentz [Reiter, 2018] functions. The masses of ^{84}Ga and ^{85}Ga were directly measured for the first time. The errors given in this table do not contain the systematic uncertainty.

Details on the evaluation procedure corresponding to each measured gallium isotope are described in the following.

- ^{80}Ga

The mass of ^{80}Ga was already determined by a Penning trap [Hakala et al., 2008]. ^{80}Ga has an isomer with an excitation energy of 22.4 keV, much lower than the peak's FWHM (380 keV), therefore in this case both peaks are considered to be unresolved peaks. The given mass of the ground state is the fitted mass minus half of the excitation energy. Also, an extra uncertainty due to unresolved peaks was quadratically added (see Unresolved Peaks Error). The number of counts obtained for the calibrant were less than for the ion of interest, making the statistical error of the calibrant a substantial contribution to the final mass uncertainty.

- ^{81}Ga

The mass of ^{81}Ga was also measured previously by a Penning trap [Hakala et al., 2008].

- ^{82}Ga

The mass of ^{82}Ga was also measured in [Hakala et al., 2008]. In this case, the calibration was performed with an unresolved peak consisting of ^{82}Rb and ^{82m}Rb with an excitation energy of only 69 keV, much lower than the peak FWHM (480 keV). Therefore, the procedure for obtaining the mass and the uncertainty for unresolved peaks was applied, see Unresolved Peaks Error.

- ^{83}Ga

The mass of ^{83}Ga was also previously measured in [Hakala et al., 2008].

- ^{84}Ga

Here, the mass of ^{84}Ga was directly measured for the first time. The calculated mass value published in [Huang et al., 2017] is based on mass models. The value obtained in the measurement slightly changes from the literature value (-7 keV), but the uncertainty is strongly reduced. In the measured spectrum, the calibrant used, ^{84}Rb, was clearly resolved from the isomeric state ^{84m}Rb, with an excitation energy of about 463 keV. In Fig. 3.31, the spectrum taken for the measurement of ^{84}Ga is shown.

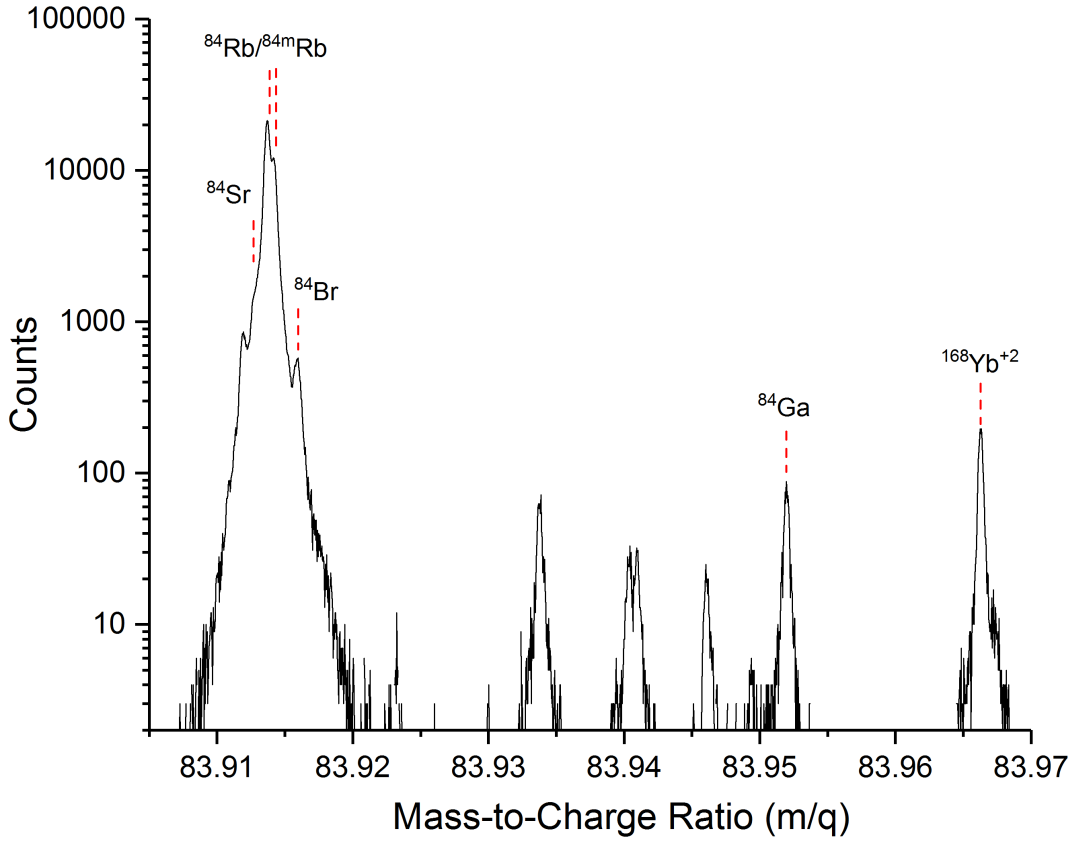

Figure 3.31: Mass spectrum measured with the MR-TOF-MS for the measurement of ^{84}Ga. Unlabelled peaks are species to be still identified.

A secondary identification method of ^{84}Ga and any possible underlying contamination was performed with the resonant laser ionization for gallium switched off. In Fig. 3.32, a zoom to the spectrum obtained by the MR-TOF-MS containing ^{84}Ga and ^{168}Yb doubly charged, with and without resonant laser ionization, is presented.

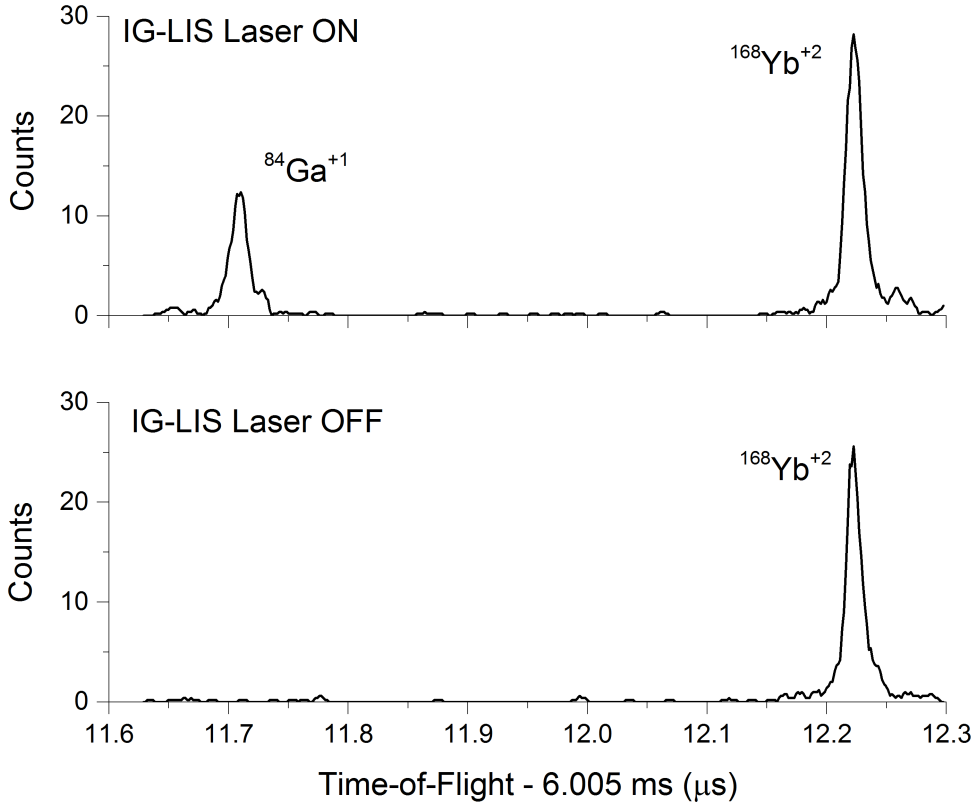

Figure 3.32: Comparison of the time-of-flight spectrum obtained with the MR-TOF-MS with the resonant laser ionization on (top) and off (bottom) at the IG-LIS source. Both spectra are accumulated over the same amount of time, 680 s. When the resonant laser ionization is off, the rate for ^{84}Ga is almost vanished, while for the ytterbium and the other species in the spectrum, which are not ionized by the laser, is almost not affected. The x-axis presented in this figure is the total time-of-flight minus an offset of 6.005 ms.

- ^{85}Ga

The mass of ^{85}Ga was also directly measured for the first time. In this case, the mass obtained deviates 106 keV from the previous published masses based on models [Huang et al., 2017]. In this case the uncertainty is also strongly reduced. The mass spectrum analyzed for the determination of the mass of ^{85}Ga is presented in Fig. 3.33. A secondary identification of ^{85}Ga and possible underlying contamination was also performed with the resonant laser ionization switched off as for the ^{84}Ga.

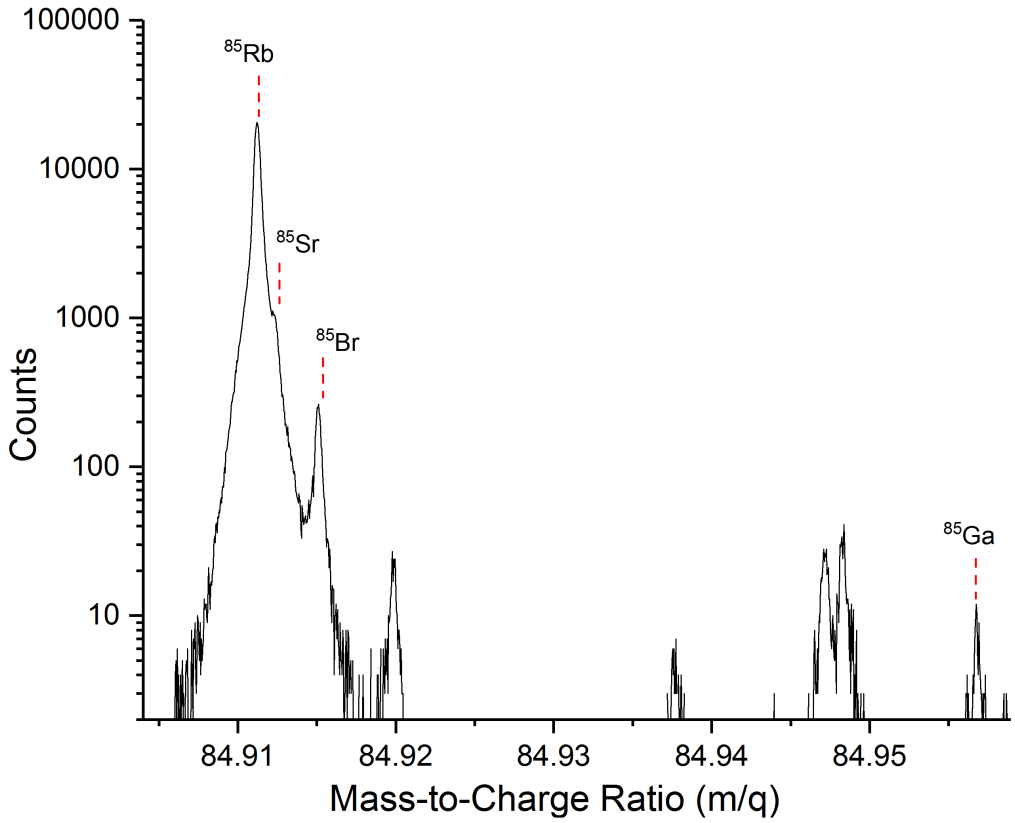

Figure 3.33: Mass spectrum taken with the MR-TOF-MS for the measurement of ^{85}Ga. The peaks unlabeled correspond to unknown species.

To combine the different values obtained in both evaluations (Gaussian and Lorentzian shape [Reiter, 2018]), the arithmetic mean of the two values is calculated, $\frac{m_a+m_b}{2}$ and $\frac{\Delta m_a+\Delta m_b}{2}$, where $m_a \pm \Delta m_a$ and $m_b \pm \Delta m_b$ are the masses and the uncertainties obtained by each evaluation. The weighted average of the difference between both evaluations is of 1.7 $\pm$ 3.7 keV, showing agreement and no systematic shift due to the use of a different analytical function for fitting the data. The combined results are shown in Tab. 3.6 and Fig. 3.34.

Nuclei	Mass (u)	Mass Excess (keV)
^{80}Ga	79.936433 (52)	-59212 (48)
^{81}Ga	80.938146 (33)	-57616 (31)
^{82}Ga	81.943130 (27)	-52974 (31)
^{83}Ga	82.947119 (27)	-49258 (25)
^{84}Ga*	83.952663 (27)	-44094 (25)
^{85}Ga*	84.957333 (35)	-39744 (32)

Table 3.6: Final mass values and uncertainties of the measured gallium isotopes obtained by the combination of the listed values in Tab. 3.5. The uncertainties include a relative systematic uncertainty of $3 \cdot 10^{-7}$ added after the combination. Nuclides marked with an asterisk are measured for the first time.

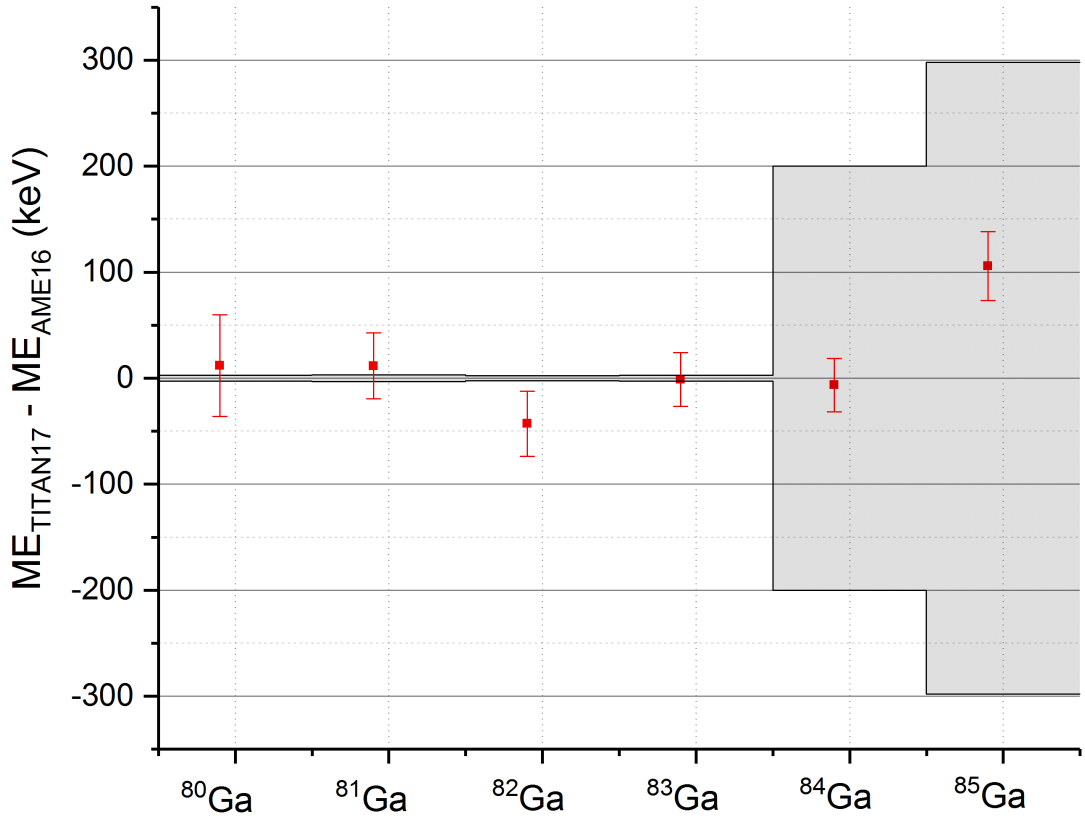

Figure 3.34: The data points show the mass excess difference between the combined evaluation and the AME16. The error bars correspond to the errors of the combined evaluation given in Tab. 3.6, including a systematic relative uncertainty of $3 \cdot 10^{-7}$. The uncertainty of the AME16 is represented in the grey area.

In this subsection of the results, mass measurements of neutron rich gallium isotopes performed with the TITAN's MR-TOF-MS were presented. The mass measurements of other nuclei corresponding to elements different than gallium will be presented elsewhere. The nuclides ^{84}Ga and ^{85}Ga with half-lives of 85 ms and 92 ms respectively, were measured for the first time in the context of this thesis. An average relative uncertainty of $4 \cdot 10^{-7}$ was obtained with a minimum of $3.3 \cdot 10^{-7}$. The impact in the r-process elemental abundances calculations of the mass values and uncertainties presented here is studied in the following.

3.2.2 Impact of Neutron-Rich Ga Masses in the r-Process Model

The masses of neutron-rich nuclei are of high importance for the understanding of the stellar nucleosynthesis. About half of the elements heavier than iron are thought to be produced by the rapid neutron capture process (r-process). During this fast process in a neutron-rich environment involving repetitive nuclear reactions such as neutron

capture, β^--decay, β-delayed neutron emission, photodissociation and others, exotic neutron-rich nuclei heavier than iron are synthesized. The structure of the final elemental abundance pattern produced depends on these nuclear properties, and which nuclei are synthesized during the process strongly depends on the astrophysical conditions [Aprahamian et al., 2014, Mumpower et al., 2016]. The abundances of actinides observed in extra-solar sources, suggest that the high abundance peaks formed around elements with A = 130 and A = 195 are produced during phases with higher neutron fluxes than the abundance peak found around A = 80 [Wasserburg et al., 1996], pointing to separate components of the r-process depending on the neutron density of the environment. The astronomical optical signal acquired in 2017 as the first electromagnetic counterpart [Nicholl et al., 2017] to a gravitational wave generated in a binary neutron star merger [LIGO and Virgo, 2017], revealed a blue component in the visible spectrum. The blue optical component was already predicted in [Metzger et al., 2010]. This blue component, powered by the radioactive decay of the synthesized nuclei in the r-process, is only able to escape if the environment presents a low opacity at these optical wavelengths. This lower opacity involves an environment where only light nuclei are present [Kasen et al., 2013], i.e. an r-process where no lanthanides are synthesized due to the less neutron-rich environment, obtaining a "blue kilonova" observable [Metzger, 2017]. The effect of the first direct mass measurements presented in this work, ^{84}Ga and ^{85}Ga, on the r-process elemental abundances for the conditions corresponding to the blue kilonova (electron fraction $Y_e = 0.35 - 0.38$) were studied [Sieverding and Nikas, 2018, Reiter et al., 2018]. Nuclear reaction network calculations similar to the one described in [Mendoza-Temis et al., 2015], were performed with different sets of (n,γ) reaction cross sections. The sets of cross sections were calculated with the Q-values obtained from two different sets of masses: a) masses of the AME16 and a variation of the masses of ^{84}Ga and ^{85}Ga centred in the literature value following a Gaussian distribution with a standard deviation corresponding to the literature uncertainty and b) masses from the AME16 including the masses and uncertainties presented in this work for ^{84}Ga and ^{85}Ga. In the second case, the uncertainties of the two measured masses do not present any change in the elemental abundances, therefore, only a single set of (n,γ) reactions was calculated with these masses. The results of the solar and calculated mass fractions (X_A) using both sets of masses are shown in Fig. 3.35.

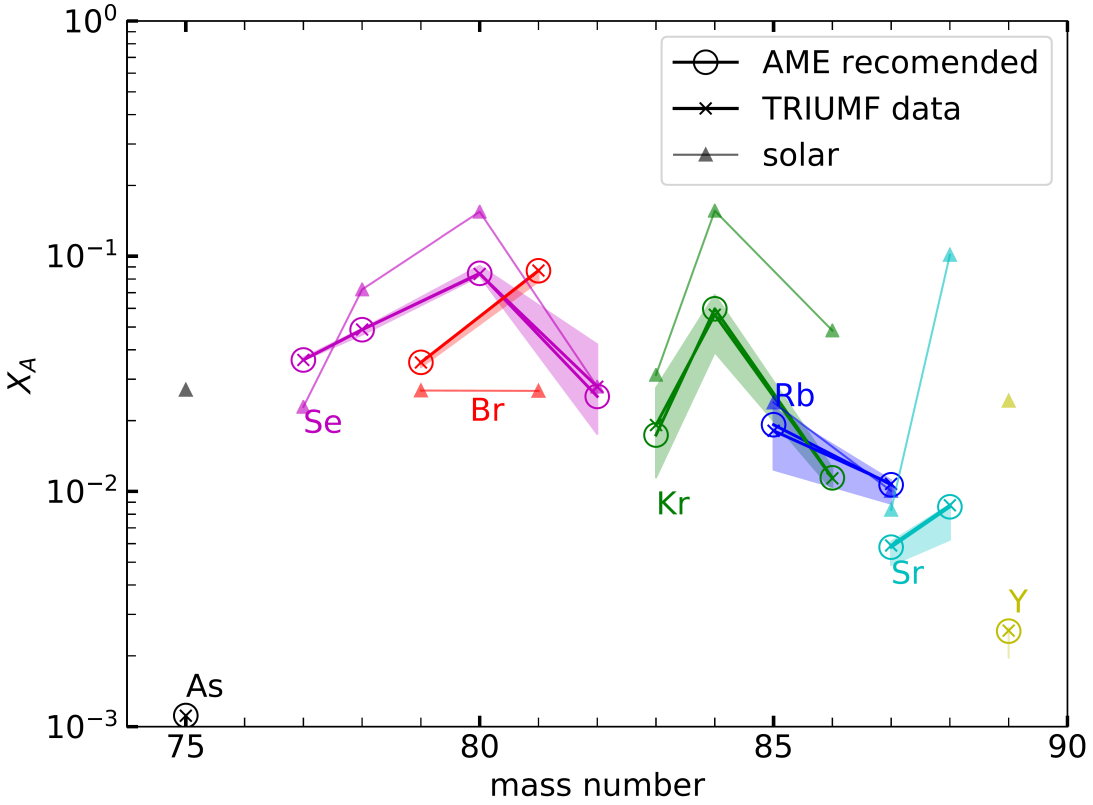

Figure 3.35: Mass fractions calculated for an r-process nucleosynthesis event with conditions corresponding to the blue kilonova. Only the produced isotopes are included. The shown values are normalized with the solar mass fraction of ^{82}Se. In circles with colored area, the calculated mass fractions using only literature mass values, where the colored area reflects the literature mass uncertainty of ^{84}Ga and ^{85}Ga. In crosses, the calculated mass fractions using literature mass values including the first direct mass measurements presented in this work for ^{84}Ga and ^{85}Ga. The low uncertainties of the measurements presented in this work for ^{84}Ga and ^{85}Ga do not contribute to a visible change in the mass fractions. In triangles, the solar mass fractions.

The mass values from the first direct mass measurement of ^{84}Ga and ^{85}Ga presented in this thesis do not differ much in value from the AME16 but the uncertainty is strongly reduced. Therefore, the calculated mass fractions for both sets of masses (circles and crosses in Fig. 3.35) are very similar and the main difference is the cross out of the colored area, which reflects the mass uncertainty of ^{84}Ga and ^{85}Ga in the calculated mass fraction. The mass fractions are normalized with the one of ^{82}Se, a nuclei which can only be produced in an r-process. In most of the cases, the calculated mass fraction is below the solar one, pointing that the observed solar mass fractions have also contributions from other different nucleosynthesis process. The calculations with the new measured masses will help to disentangle the r and s process contributions to the solar elemental abundances. A deeper discussion will be published [Reiter et al., 2018].

The results presented in this section show that the developments and improvements of mass measurement techniques, in this case to the MR-TOF-MS, enable mass measurements of exotic nuclei where no access was possible before, allowing to reach the region of the nuclear chart which is of high importance to better understand the nuclear physics behind the blue kilonova, produced by the merger of two neutron star where a gravitational wave was observed by LIGO/VIRGO detectors.

4 Summary and Outlook

Masses are a key property of atomic nuclei, their accurate measurement helps to understand the nuclear structure and the stellar nucleosynthesis. Driven by the need to access nuclear masses of very exotic nuclei, where production rates are low (few per hour or day) and half-lives are short (few ms), a measurement technique, Multiple-Reflection Time-of-Flight Mass-Spectrometry (MR-TOF-MS), has been developed at different rare isotope beam facilities around the world. In the context of this work, improvements of the system at FRS/GSI have been done, enabling mass measurements of the most exotic and short-lived nuclei with the highest and unprecedented accuracy. The kinetic energy of the ions and the repetition rate of the spectrometer were increased, obtaining resolving powers in excess of 600.000 in less than 20 ms of measurement time and repetition rates exceeding 1000 Hz. In addition, an increase of the reliability and stability of the system, lowering the temperature coefficient of the spectrometer to 8 ppm/°C, has been shown. The system is universal and can measure elements independent of their chemical properties, demonstrated by measuring noble gases and very reactive elements like uranium. Moreover, the data analysis procedure to determine the mass value and the uncertainty was further improved. The method was specially developed to precisely extract the masses of very low statistics peaks and of overlapping peaks when only a change in peak shape can be observed. With this data analysis procedure, the effective mass resolving power is increased by up to a factor of 3 for overlapping peaks, e.g. the resolution of low-lying isomers.

During three experiments at GSI (Germany) in 2014 and 2016, mass measurements of thermalized fission fragments of ^{238}U as well as thermalized projectile fragments of ^{238}U and ^{124}Xe, produced and separated in the FRS, were performed with the MR-TOF-MS of the FRS-Ion Catcher with resolving powers up to 450.000. Following the improved data analysis procedure presented in this work, a total of 25 masses of short-lived nuclei were measured, of which 7 correspond to isomeric states with excitation energies down to about 280 keV. Isotopes of 8 different elements with half-lives of less than 300 ms have been measured. The reported masses obtained in this thesis with the MR-TOF-MS of the FRS-Ion Catcher have a minimum total relative uncertainty of $1.1 \cdot 10^{-7}$, corresponding to an absolute value of 13 keV. The lowest uncertainty of a mass measurement performed with at the FRS-Ion Catcher with the improvements

presented in this thesis is $6 \cdot 10^{-8}$ [Hornung, 2018]. The average deviation from the literature of all the measured masses in the FRS-Ion Catcher is of 4.3 ± 2.5 keV, showing no systematic deviation. Besides direct mass measurements, the broadband capabilities of the system in combination with a high resolving power were used for the identification via mass measurements of uranium ions and molecules in different charge states. This feature was applied to the study of the cleanliness of the system. The FRS-Ion Catcher is now fully operational and offers a superior combination of performance characteristics for measurements with exotic nuclei in unknown territory.

In an experiment at TRIUMF (Canada) in 2017, mass measurements of neutron-rich gallium isotopes from A = 80 to A = 85 were performed with the newly installed TITAN's MR-TOF-MS, developed, built and commissioned at the Justus-Liebig University. Recently the electronics have been improved in the same way as for the MR-TOF-MS at FRS/GSI. The masses of ^{84}Ga and ^{85}Ga, with half-lives of 85 ms and 92 ms, respectively, were measured for the first time in the context of this thesis. A minimum relative uncertainty of $3.3 \cdot 10^{-7}$ was obtained. The mass measurements of ^{84}Ga and ^{85}Ga have a high impact on the understanding of the nucleosynthesis processes in the neutron star merger event observed by LIGO/VIRGO and followed by a blue kilonova transient, as they pin down the nuclear physics input for ^{82}Se which can only be produced in the r-process.

A summary of the nuclides of which the mass of ground, isomer or both states was presented in this thesis is shown in Fig. 4.1.

On the way towards the new rare isotope beam (RIB) facilities such as the low energy branch (LEB) of the Super-FRS at FAIR or the advanced rare isotope laboratory (ARIEL) in TRIUMF, several experiments at GSI and TRIUMF are planed in the short-term horizon for the spectrometers presented in this thesis, where high-accuracy mass measurements of exotic nuclei, enabled by the developments presented in the thesis, will be performed. The near-future experiments are:

- In the FRS-Ion Catcher at GSI, new experiments will be carried out during the beamtime periods allocated in FAIR Phase-0 in 2018 and 2019. The MR-TOF-MS will be used for direct mass measurements of exotic nuclei: around the N = Z region, below ^{100}Sn [Plaß et al., 2018] and around the neutron-rich isotopes below ^{208}Pb with N=126 (between Z = 65 to Z = 75) [Pietri et al., 2018]. The MR-TOF-MS will be used to perform the identification and counting of reaction products of nuclei undergoing a β-delayed neutron emission to obtain the β-delayed neutron emission probabilities [Mardor et al., 2018], which besides masses and half-lives, is the next important nuclear quantity for modelling the

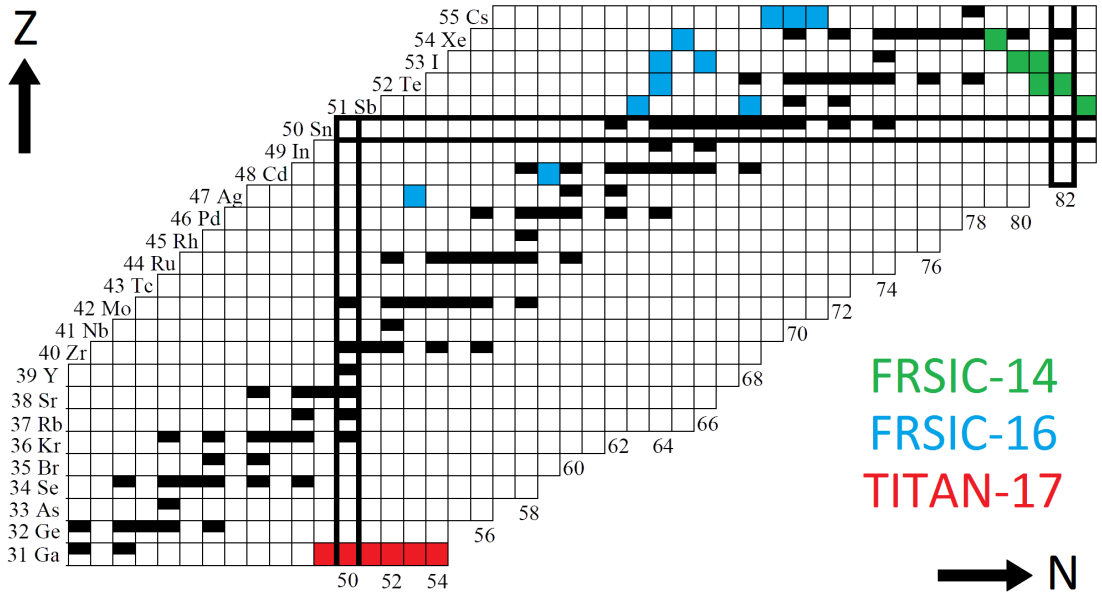

Figure 4.1: Nuclear chart with the presented masses (ground, isomeric or both states) highlighted. In black, stable isotopes. In green and blue, the presented nuclei measured in the FRS-Ion Catcher during the experiments in 2014 and 2016 at GSI, respectively and in red the presented nuclei measured in TITAN at TRIUMF during the experiment in 2017.

r-process abundances. Another experiment aims to perform multi-nucleon transfer (MNT) reaction studies and identify the reaction products via high precision mass measurements [Dickel et al., 2018], filling the need of experimental data for the models describing such reactions.

- In TRIUMF, during the beamtime period of 2018, the MR-TOF-MS has scheduled a beamtime where mass measurements of neutron-deficient lanthanides will be performed. These high precision mass measurements will allow to identify the possible existence of a quenching effect of the N = 82 shell closure in neutron-deficient nuclei.

The combination of the next generation RIB facilities with increased production rates of exotic nuclei, such as the LEB at FAIR, and a further developed MR-TOF-MS as part of the MATS (precision Measurements of very short-lived nuclei using an Advanced Trapping System for highly-charged ions) collaboration, with mass resolving powers exceeding one million and relative mass uncertainties in the low 10^{-8} level routinely achieved, will extend the mass measurements landscape over the neutron-rich area, gaining key information for understanding the structure of the nuclei and the synthesis of heavy elements in the universe.

5 Appendix

A.1 Pulsers

The term pulser used in this thesis, refers to an electronic device capable of switching its output between two different high voltage inputs. This change is controlled by a low voltage signal (TTL for example). Three different versions of pulsers have been developed in the framework of this thesis for the MR-TOF-MS, enabling some of the current capabilities of the device. In Fig. A.1 one of the versions is shown.

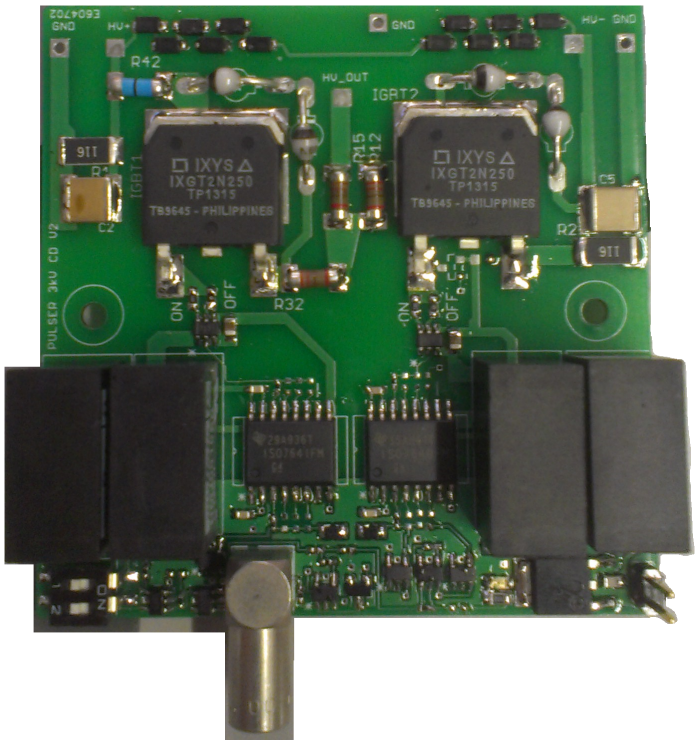

Figure A.1: Picture of a high voltage standard pulser. The TTL input is supplied via a LEMO connector. In the lower left corner, micro switches for selecting 50Ω termination line for the TTL signal and polarity inversion of the high voltage pulsers are included. High voltage inputs (HV+ and HV-) and outputs (HV-OUT) are on the top. The TTL selects if OUT = HV+ or OUT = HV-.

All the three versions are based in an isolated half-bridge push-pull configuration, including an anti-cross conduction circuit for improved efficiency. A basic block diagram

of the pulser is shown in Fig. A.2. This block diagram reflects the functionality used for all the three versions of the pulsers designed for the MR-TOF-MS.

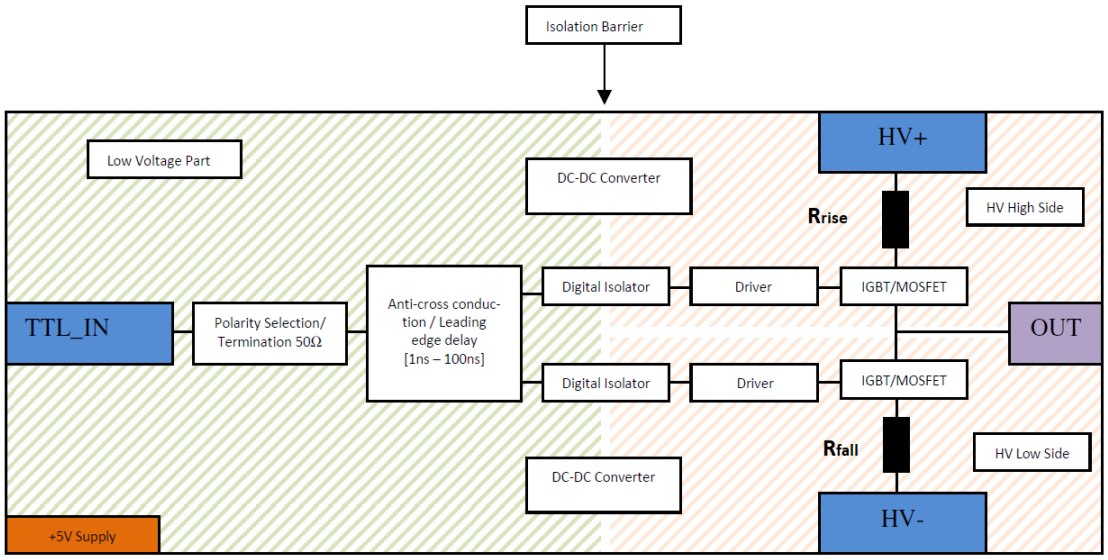

Figure A.2: Basic block diagram of all three designed versions of the pulser. In green, the low voltage side and in orange the high voltage (HV) high and low sides.

In this diagram, the TTL signal is first adapted (polarity selection and termination) and forwarded to the anti-cross conduction delay generator where the asymmetric signals for controlling the identical switching devices are generated. This anti-cross conduction generator is needed since the time to turn on or off the switching devices is not symmetric and if not included, there will be for a short time a low impedance path between the inputs HV+ and HV- every time the output changes its state. The anti-cross conduction concept is based in delaying the rising edge of the switching devices while keeping the falling edge without any delay. The delay can be selected independently for each switching device by selecting two different RC sets. After the generation of the anti-cross conduction delay, the control signals of the switching devices have to be transmitted over an isolation barrier. In this case, the signals are transmitted over a digital isolator to the high voltage part of the schematic independently (HV+ side and HV- side). This signals control a MOSFET driver which will finally drive the state of the MOSFETs or IGBTs. The resistors connected to the switching devices (R_{rise} and R_{fall}) govern the slope of the output voltage. The low voltage supply of the digital isolators and drivers is perform via isolated DC-DC converters. All the three different pulser versions share the same topology but the use of different switching devices involves the use of different gate driving voltages as well as different anti-cross conduction delays. The high power capabilities of the RF Pulsers is achieved by the use of active heat dissipation elements, which is not needed in the other versions. The main differences between the different versions rely in the different switching device used. In the following, a brief description of the different versions is given:

1. **High Voltage Standard Pulsers**: this pulsers use two insulated-gate bipolar transistors (IGBTs) as switching devices (IXGT2N250). The maximum absolute voltage of the inputs is 3 kV and the maximum difference between HV+ and HV- to be pulsed is 2.2 kV. The typical rise and fall times of the output, with a typical capacity of 100 pF and resistors (R_{rise} and R_{fall}) of about 200Ω, are around 200 ns. The falling and rising slew rate can be set independently. This version is used in both MR-TOF-MS presented in this work. Between others, they are used for pulsing the potential of the analyzer electrodes in order to trap or release the ions or perform the time-focus-shift reflections.

2. **High Voltage Current Pulsers**: the speciality of this pulsers is the ability to switch the output potential while delivering hundreds of mA of current with high efficiency. This is achieved by the use of two silicon carbide (SiC) metal-oxide-semiconductor field-effect transistor (MOSFET) as switching devices (C2M1000170D). The SiC technology provides a very low tail current compared with silicon based IGBTs or MOSFETs. The driving levels for the gates as well as the anti-cross conduction delays were adapted to the needs of the SiC technology. The maximum absolute voltage of the inputs is also 3 kV but the maximum difference between HV+ and HV- is 1.7 kV. The typical rise and fall times, with a capacity of around 100 pF, are around 25 to 50 ns. The R_{rise} and R_{fall} values are less than 10Ω in order to not have a voltage drop due to the high current flow (hundreds of mA). This version is only used for the potential lift of the ions in the FRS-Ion Catcher MR-TOF-MS and is the one enabling the high repetition rate of the system (> 1000 Hz). See Fig. 2.9.

3. **RF Pulsers**: this pulsers have the special feature of being able to pulse signals in a multi-MHz frequency. The switching devices used here are two power MOSFETs (SIHD3N50D). The anti-cross conduction delays where minimized to reach a maximum frequency of around 5 MHz. The maximum absolute voltage allowed at the inputs is 3 kV but the maximum difference to be pulsed is 500 V. There is a trade-off between the maximum frequency and the maximum pulsing voltage, limited by the maximum dissipated power allowed of about 50 W. The typical rise and fall times with a capacity of around 100 pF and are around 15 to 30 ns. This version is used in the generation of the RF signals that are applied to the trap system. See Fig. 2.9.

Acknowledgments

I would like to thank everybody who helped and supported me during this work. I have learnt from all of you, scientifically and personally. Many thanks to Prof. Dr. Christoph Scheidenberger and Prof. Dr. Dr. h.c. Hans Geissel for giving me the opportunity of taking such an exciting adventure in the world of physics.

Special thanks to Dr. Timo Dickel, who introduced me to the world of experimental physics, supported me during this work until the last correction of the thesis and showed me how to be a pragmatic experimentalist while sharing smiles all around. Many thanks also to Dr. Wolfgang R. Plaß for showing me how to precisely and clearly communicate scientific results.

Many thanks to all the IONAS Group from the Justus-Liebig University who were my lab-mates at GSI, with whom I shared most of my time during this work: Dr. Jens Ebert, Christine Hornung, Sönke Beck, Dr. Pascal Reiter, Dr. Ann-Kathrin Rink and Ivan Miskun. Also to those members of the IONAS group who were not directly involved in my daily work but made a great pleasure to spend time with them in conferences, barbecues, etc.: Dr. Marcel Diwisch (FCB auf geht's!), Dr. Wayne Lippert, Florian Greiner, Julian Bergmann, Dr. Christian Jesch, Dr. Johannes Lang, Daler Amanbayev and Dr. Natalia Kuzminchuk. Thanks to Alexander Buers for building part of the electronics developed in the context of this thesis. Many thanks to all the other IONAS group members that I've met during this work.

Many thanks to all the FRS-Ion Catcher collaboration who made possible the results obtained during the experiments at GSI presented in this thesis. Special thanks to Dr. Emma Haettner and Dr. Sivaji Purushotaman.

Also many thanks to the TITAN group at TRIUMF, who made possible a part of the results presented in this thesis and made my stay during the first MR-TOF-MS experiment a very enriching experience.

Thanks to the Experimental Electronics group from GSI where I was taking part actively and shared the time while doing this work, specially to Dr. Eugen Badura and Dr. Karsten Koch.

To all my friends I met at GSI during this period of my life, specially to my soccer mates: Alexander Helm, Samuel Giuliani (# 2.0), Cahit Ugur, Jorge Ceballos, Marco

Cassinelli, Tomas Rodriguez, Almudena Montiel and all the other UFH team mates: thank you, I enjoyed a lot the time with you.

I would like to send many thanks to all my friends from Valencia: Nelo, David, Pau, Marky, Alex... with a very big ETC to all the others, including the former colleagues from the university. You always made me feel back home when I was in Valencia, I really appreciate your friendship.

To my parents, Amparo and Manuel, many thanks for your support in all the decisions I have taken in my life, including this "crazy" one as you said. I have learned many things from you, also from the distance. To my sister Clara, who contributed not only during this period to develop my human and social part enormously and complemented my scientific and engineering side, huge thanks for listen, support and advice me whenever I was lost.

I have reserved the last words for Katja. Many thanks for all your support during this adventure, where you had first-row tickets to see my highs and lows. Sharing this period with you made it even more special. I'm very lucky that you are part of my life.

References

[Alikhanov, 1957] Alikhanov, S. (1957). A New Impulse Technique for Ion Mass Measurements. *Soviet Phys. JETP*, 4.

[Anicich, 2003] Anicich, V. G. (2003). An index of the Literature for Bimolecular Gas Phase Cation-Molecule Reaction Kinetics. *JPL-Publication-03-19*.

[Aprahamian et al., 2014] Aprahamian, A., Bentley, I., Mumpower, M., and Surman, R. (2014). Sensitivity studies for the main r process: nuclear masses. *AIP Advances*, 4(4):041101.

[Aston, 1920] Aston, F. W. (1920). Isotopes and atomic weights. *Nature*, 105(2646):617–619.

[Aston, 1927] Aston, F. W. (1927). Bakerian lecture: A new mass-spectrograph and the whole number rule. *Proceedings of the Royal Society of London A: Mathematical, Physical and Engineering Sciences*, 115(772):487–514.

[Atasanov, 2016] Atasanov, D. (2016). *Precision Mass Measurements for Studies of Nucleosynthesis via the Rapid Neutron-Capture Process*. PhD thesis, Ruprecht-Karls-Universität, Heidelberg.

[Audi et al., 2017] Audi, G., Kondev, F., Wang, M., Huang, W., and Naimi, S. (2017). The nubase2016 evaluation of nuclear properties. *Chinese Physics C*, 41(3):030001.

[Audi et al., 2012] Audi, G., Wang, M., Wapstra, A., Kondev, F., MacCormick, M., Xu, X., and Pfeiffer, B. (2012). The ame2012 atomic mass evaluation. *Chinese Physics C*, 36(12):1287.

[Ayet San Andrés, 2018] Ayet San Andrés, S. (2018). *Developments for Multiple-Reflection Time-of-Flight Mass Spectrometers and their Application to High Resolution Accurate Mass Measurements of Short-Lived Exotic Nuclei*. PhD thesis, Justus-Liebig-Universität.

[Bergmann, 2018a] Bergmann, J. (2018a). *Manuscript in Preparation*. PhD thesis, Justus-Liebig-Universität, Gießen.

[Bergmann, 2018b] Bergmann, J. (2018b). Private comunication.

[Bergmann et al., 2018] Bergmann, J., Ayet, S., Beck, S., and Dickel, T. (2018). *Internal Report*.

[Birge, 1932] Birge, R. T. (1932). The calculation of errors by the method of least squares. *Phys. Rev.*, 40:207–227.

[Blaum, 2006] Blaum, K. (2006). High-accuracy mass spectrometry with stored ions. *Physics Reports*, 425(1):1 – 78.

[Blaum et al., 2013] Blaum, K., Dilling, J., and Nörtershäuser, W. (2013). Precision atomic physics techniques for nuclear physics with radioactive beams. *Physica Scripta*, 2013(T152):014017.

[Bricault et al., 2014] Bricault, P. G., Ames, F., Dombsky, M., Kunz, P., and Lassen, J. (2014). Rare isotope beams at isac—target and ion source systems. *Hyperfine Interactions*, 225:25.

[Brunner et al., 2012] Brunner, T., Smith, M., Brodeur, M., Ettenauer, S., Gallant, A., Simon, V., Chaudhuri, A., Lapierre, A., Mané, E., Ringle, R., Simon, M., Vaz, J., Delheij, P., Good, M., Pearson, M., and Dilling, J. (2012). Titan's digital rfq ion beam cooler and buncher, operation and performance. *Nuclear Instruments and Methods in Physics Research Section A: Accelerators, Spectrometers, Detectors and Associated Equipment*, 676(Supplement C):32 – 43.

[Burbidge et al., 1957] Burbidge, E. M., Burbidge, G. R., Fowler, W. A., and Hoyle, F. (1957). Synthesis of the elements in stars. *Rev. Mod. Phys.*, 29:547–650.

[Cameron, 1957] Cameron, A. G. W. (1957). Nuclear reactions in stars and nucleogenesis. *Publications of the Astronomical Society of the Pacific*, 69(408):201.

[Chen et al., 2010] Chen, L., Plaß, W., Geissel, H., Knöbel, R., Kozhuharov, C., Litvinov, Y., Patyk, Z., Scheidenberger, C., Siegień-Iwaniuk, K., Sun, B., Weick, H., Beckert, K., Beller, P., Bosch, F., Boutin, D., Caceres, L., Carroll, J., Cullen, D., Cullen, I., Franzke, B., Gerl, J., Górska, M., Jones, G., Kishada, A., Kurcewicz, J., Litvinov, S., Liu, Z., Mandal, S., Montes, F., Münzenberg, G., Nolden, F., Ohtsubo, T., Podolyák, Z., Propri, R., Rigby, S., Saito, N., Saito, T., Shindo, M., Steck, M., Ugorowski, P., Walker, P., Williams, S., Winkler, M., Wollersheim, H.-J., and Yamaguchi, T. (2010). Discovery and investigation of heavy neutron-rich isotopes with time-resolved schottky spectrometry in the element range from thallium to actinium. *Physics Letters B*, 691(5):234 – 237.

[Czok, 2010] Czok, U. (2010). Private comunication.

[Dickel, 2010] Dickel, T. (2010). *Design and Comissioning of an Ultra-High-Resolution Time-of-Flight Based Isobar Separator and Mass Spectrometer*. PhD thesis, Justus-Liebig-Universität.

[Dickel et al., 2018] Dickel, T., Constantin, P., Winfield, J., Ayet San Andres, S., Bagchi, S., Balbanski, D., Beck, S., Geissel, H., Greiner, F., Haettner, E., Hornung, C., Heinz, S., Kankainen, A., Karpov, A., Kostyleva, D., Kuzminchuk, N., Kindler, B., Lommel, B., Mardor, I., Martinez Pinedo, G., Miskun, I., Mukha, I., Münzenberg, G., Patyk, Z., Piasetzky, E., Pietri, S., Plaß, W., Pomerantz, I., Prochazka, A., Purushotaman, S., Rappold, C., Saito, T., Saiko, V., Scheidenberger, C., and Weick, H. (2018). Reaction studies with the FRS Ion Catcher: A novel approach and universal method for the production, identification of and experiments with unstable isotopes produced in multi-nucleon transfer reactions with stable and unstable beams. *GSI Scientific Report*, 2018-1.

[Dickel et al., 2015] Dickel, T., Plaß, W., Ayet San Andres, S., Ebert, J., Geissel, H., Haettner, E., Hornung, C., Miskun, I., Pietri, S., Purushothaman, S., Reiter, M., Rink, A.-K., Scheidenberger, C., Weick, H., Dendooven, P., Diwisch, M., Greiner, F., Heiße, F., Knöbel, R., Lippert, W., Moore, I., Pohjalainen, I., Prochazka, A., Ranjan, M., Takechi, M., Winfield, J., and Xu, X. (2015). First spatial separation of a heavy ion isomeric beam with a multiple-reflection time-of-flight mass spectrometer. *Physics Letters B*, 744(Supplement C):137 – 141.

[Dickel et al., 2017a] Dickel, T., Plaß, W. R., Lippert, W., Lang, J., Yavor, M. I., Geissel, H., and Scheidenberger, C. (2017a). Isobar separation in a multiple-reflection time-of-flight mass spectrometer by mass-selective re-trapping. *Journal of The American Society for Mass Spectrometry*, 28(6):1079–1090.

[Dickel et al., 2017b] Dickel, T., Yavor, M. I., Lang, J., Plaß, W. R., Lippert, W., Geissel, H., and Scheidenberger, C. (2017b). Dynamical time focus shift in multiple-reflection time-of-flight mass spectrometers. *International Journal of Mass Spectrometry*, 412(Supplement C):1 – 7.

[Dilling et al., 2006] Dilling, J., Baartman, R., Bricault, P., Brodeur, M., Blomeley, L., Buchinger, F., Crawford, J., López-Urrutia, J. C., Delheij, P., Froese, M., Gwinner, G., Ke, Z., Lee, J., Moore, R., Ryjkov, V., Sikler, G., Smith, M., Ullrich, J., and Vaz, J. (2006). Mass measurements on highly charged radioactive ions, a new approach to high precision with titan. *International Journal of Mass Spectrometry*, 251(2):198 – 203.

[Dombsky et al., 2000] Dombsky, M., Bishop, D., Bricault, P., Dale, D., Hurst, A., Jayamanna, K., Keitel, R., Olivo, M., Schmor, P., , and Stanford, G. (2000). Com-

missioning and initial operation of a radioactive beam ion source at isac. *Review of Scientific Instruments*, 71:978.

[Ebert, 2016] Ebert, J. (2016). *Mass measurements of 238U-projectile fragments for the first time with a Multiple-Reflection Time-Of-Flight Mass Spectrometer*. PhD thesis, Justus-Liebig-Universität.

[Eddington, 1920] Eddington, A. S. (1920). The internal constitution of the stars. *Nature*, 106(2653):14–20.

[Eliseev et al., 2013] Eliseev, S., Blaum, K., Block, M., Droese, C., Goncharov, M., Minaya Ramirez, E., Nesterenko, D. A., Novikov, Y. N., and Schweikhard, L. (2013). Phase-imaging ion-cyclotron-resonance measurements for short-lived nuclides. *Phys. Rev. Lett.*, 110:082501.

[Farinon, 2011] Farinon, F. (2011). *Unambiguous identification and investigation of uranium projectile fragments and the discovery of 63 new neutron-rich isotopes in the element range 61 less-than or equal to Z less-than or equal to 78 at the FRS*. PhD thesis, Justus-Liebig-Universität.

[Fogelberg et al., 1999] Fogelberg, B., Mezilev, K. A., Mach, H., Isakov, V. I., and Slivova, J. (1999). Precise atomic mass values near 132Sn: The resolution of a puzzle. *Phys. Rev. Lett.*, 82:1823–1826.

[Franzke, 1987] Franzke, B. (1987). The heavy ion storage and cooler ring project esr at gsi. *Nuclear Instruments and Methods in Physics Research Section B: Beam Interactions with Materials and Atoms*, 24(Part 1):18 – 25.

[Freedman and Diaconis, 1981] Freedman, D. and Diaconis, P. (1981). On the histogram as a density estimator:l2 theory. *Zeitschrift für Wahrscheinlichkeitstheorie und Verwandte Gebiete*, 57(4):453–476.

[Gabrielse, 2009] Gabrielse, G. (2009). Why is sideband mass spectrometry possible with ions in a penning trap? *Phys. Rev. Lett.*, 102:172501.

[Geissel, 2018] Geissel, H. (2018). Private comunication.

[Geissel et al., 1992a] Geissel, H., Armbruster, P., Behr, K., Brünle, A., Burkard, K., Chen, M., Folger, H., Franczak, B., Keller, H., Klepper, O., Langenbeck, B., Nickel, F., Pfeng, E., Pfützner, M., Roeckl, E., Rykaczewski, K., Schall, I., Schardt, D., Scheidenberger, C., Schmidt, K.-H., Schröter, A., Schwab, T., Sümmerer, K., Weber, M., Münzenberg, G., Brohm, T., Clerc, H.-G., Fauerbach, M., Gaimard, J.-J., Grewe, A., Hanelt, E., Knödler, B., Steiner, M., Voss, B., Weckenmann, J., Ziegler, C., Magel, A., Wollnik, H., Dufour, J., Fujita, Y., Vieira, D., and Sherrill, B. (1992a).

The GSI projectile fragment separator (FRS): a versatile magnetic system for relativistic heavy ions. *Nuclear Instruments and Methods in Physics Research Section B: Beam Interactions with Materials and Atoms*, 70(1):286 – 297.

[Geissel et al., 1992b] Geissel, H., Beckert, K., Bosch, F., Eickhoff, H., Franczak, B., Franzke, B., Jung, M., Klepper, O., Moshammer, R., Münzenberg, G., Nickel, F., Nolden, F., Schaaf, U., Scheidenberger, C., Spädtke, P., Steck, M., Sümmerer, K., and Magel, A. (1992b). First storage and cooling of secondary heavy-ion beams at relativistic energies. *Phys. Rev. Lett.*, 68:3412–3415.

[Geissel et al., 2014] Geissel, H., Huyse, M., Münzenberg, G., and Van Duppen, P. (2014). Exotic nuclear beam facilities. *Digital Encyclopedia of Applied Physics*.

[Geissel et al., 1995] Geissel, H., Munzenberg, G., and Riisager, K. (1995). Secondary exotic nuclear beams. *Annual Review of Nuclear and Particle Science*, 45(1):163–203.

[Greiner, 2013] Greiner, F. (2013). Aufbau und erprobung einer elektrischen rfq-strahlweiche. *Bachelor Thesis - Justus-Liebig-Universität, Gießen*.

[Greiner, 2017] Greiner, F. (2017). Aufbrechen von edelgasmolekülen unter kollisionsinduzierte dissoziation mit hilfe von radiofrequenzquadrupolen. *Master Thesis - Justus-Liebig-Universität, Gießen*.

[Haettner, 2014] Haettner, E. (2014). Private comunication.

[Hakala et al., 2008] Hakala, J., Rahaman, S., Elomaa, V.-V., Eronen, T., Hager, U., Jokinen, A., Kankainen, A., Moore, I. D., Penttilä, H., Rinta-Antila, S., Rissanen, J., Saastamoinen, A., Sonoda, T., Weber, C., and Äystö, J. (2008). Evolution of the $n = 50$ shell gap energy towards ^{78}Ni. *Phys. Rev. Lett.*, 101:052502.

[Hornung, 2018] Hornung, C. (2018). *High-Resolution Experiments with the MR-TOF-MS at the FRS*. PhD thesis, Justus-Liebig-Universität, Gießen.

[Hornung et al., 2018] Hornung, C., Amanbayev, D., Ayet, S., bergmann, J., Dickel, T., Geissel, H., Greiner, F., Groef, L., Plaß, W., Rink, A.-K., and Scheidenberger, C. (2018). An upgrade to the RFQ beam line of the FRS Ion Catcher. *GSI Scientific Report*, 2018-1.

[Huang et al., 2017] Huang, W., Audi, G., Wang, M., Kondev, F., Naimi, S., and Xu, X. (2017). The ame2016 atomic mass evaluation (i). evaluation of input data; and adjustment procedures. *Chinese Physics C*, 41(3):030002.

[Ishimatsu et al., 1967] Ishimatsu, T., Yagi, K., Ohmura, H., Nakajima, Y., Nakagawa, T., and Orihara, H. (1967). The (3He, d) reaction on 116Sn, 118Sn and 120Sn. *Nuclear Physics A*, 104(3):481 – 496.

[Jesch, 2009] Jesch, C. (2009). Injektions-ionenfallensystem für ein multireflexions-flugzeitmassenspektrometer. *Master Thesis - Justus-Liebig-Universität, Gießen*.

[Jesch, 2016] Jesch, C. (2016). *The multiple-reflection time-of-flight isobar separator for TITAN and direct mass measurements at the FRS Ion Catcher*. PhD thesis, Justus-Liebig-Universität.

[Jesch et al., 2015] Jesch, C., Dickel, T., Plaß, W. R., Short, D., Ayet San Andres, S., Dilling, J., Geissel, H., Greiner, F., Lang, J., Leach, K. G., Lippert, W., Scheidenberger, C., and Yavor, M. I. (2015). The mr-tof-ms isobar separator for the titan facility at triumf. *Hyperfine Interactions*, 235(1):97–106.

[Kasen et al., 2013] Kasen, D., Badnell, N. R., and Barnes, J. (2013). Opacities and spectra of the r-process ejecta from neutron star mergers. *The Astrophysical Journal*, 774(1):25.

[Kern et al., 1992] Kern, J., Engel, T., Hagena, D., and Werth, G. (1992). Mass determination of light ions in a penning trap by time-of-flight detection of ion resonances. *Physica Scripta*, 46(6):575.

[Knöbel et al., 2016] Knöbel, R., Diwisch, M., Bosch, F., Boutin, D., Chen, L., Dimopoulou, C., Dolinskii, A., Franczak, B., Franzke, B., Geissel, H., Hausmann, M., Kozhuharov, C., Kurcewicz, J., Litvinov, S., Martinez-Pinedo, G., Matoš, M., Mazzocco, M., Münzenberg, G., Nakajima, S., Nociforo, C., Nolden, F., Ohtsubo, T., Ozawa, A., Patyk, Z., Plaß, W., Scheidenberger, C., Stadlmann, J., Steck, M., Sun, B., Suzuki, T., Walker, P., Weick, H., Wu, M.-R., Winkler, M., and Yamaguchi, T. (2016). First direct mass measurements of stored neutron-rich 129,130,131cd isotopes with frs-esr. *Physics Letters B*, 754:288 – 293.

[König et al., 1995] König, M., Bollen, G., Kluge, H.-J., Otto, T., and Szerypo, J. (1995). Quadrupole excitation of stored ion motion at the true cyclotron frequency. *International Journal of Mass Spectrometry and Ion Processes*, 142(1):95 – 116.

[Lang, 2016] Lang, J. S. (2016). *Development of a mobile high-resolution Multiple-Reflection Time-of-Flight Mass Spectrometer for in-situ life science application*. PhD thesis, Justus-Liebig-Universität.

[Leistenschneider et al., 2018] Leistenschneider, E., Reiter, M. P., Ayet San Andrés, S., Kootte, B., Holt, J. D., Navrátil, P., Babcock, C., Barbieri, C., Barquest, B. R., Bergmann, J., Bollig, J., Brunner, T., Dunling, E., Finlay, A., Geissel, H., Graham,

L., Greiner, F., Hergert, H., Hornung, C., Jesch, C., Klawitter, R., Lan, Y., Lascar, D., Leach, K. G., Lippert, W., McKay, J. E., Paul, S. F., Schwenk, A., Short, D., Simonis, J., Somà, V., Steinbrügge, R., Stroberg, S. R., Thompson, R., Wieser, M. E., Will, C., Yavor, M., Andreoiu, C., Dickel, T., Dillmann, I., Gwinner, G., Plaß, W. R., Scheidenberger, C., Kwiatkowski, A. A., and Dilling, J. (2018). Dawning of the $N = 32$ shell closure seen through precision mass measurements of neutron-rich titanium isotopes. *Phys. Rev. Lett.*, 120:062503.

[LIGO and Virgo, 2017] LIGO and Virgo (2017). Gw170817: Observation of gravitational waves from a binary neutron star inspiral. *Phys. Rev. Lett.*, 119:161101.

[Lippert, 2016] Lippert, W. (2016). *Further development and application of a mobile multiple-reflection time-of-flight mass spectrometer for analytical high-resolution tandem mass spectrometry*. PhD thesis, Justus-Liebig-Universität.

[Litvinov et al., 2010] Litvinov, Y., Geissel, H., Knobel, R., Sun, B., and Xu, H. (2010). Direct mass measurements of exotic nuclei in storage rings. *Acta Physica Polonica B*, 41(2):511 – 523.

[Litvinov et al., 2005] Litvinov, Y., Geissel, H., Radon, T., Attallah, F., Audi, G., Beckert, K., Bosch, F., Falch, M., Franzke, B., Hausmann, M., Hellström, M., Kerscher, T., Klepper, O., Kluge, H.-J., Kozhuharov, C., Löbner, K., Münzenberg, G., Nolden, F., Novikov, Y., Quint, W., Patyk, Z., Reich, H., Scheidenberger, C., Schlitt, B., Steck, M., Sümmerer, K., Vermeeren, L., Winkler, M., Winkler, T., and Wollnik, H. (2005). Mass measurement of cooled neutron-deficient bismuth projectile fragments with time-resolved schottky mass spectrometry at the frs-esr facility. *Nuclear Physics A*, 756(1):3 – 38.

[Lodders, 2003] Lodders, K. (2003). Solar system abundances and condensation temperatures of the elements. *The Astrophysical Journal*, 591(2):1220.

[Mamyrin, 1966] Mamyrin, B. A. (1966). *Investigations in the Field of Ion Separation by Time of Flight*. PhD thesis, Ioffe Physico-Technical Institute of the Russian Academy of Sciences.

[Mardor et al., 2018] Mardor, I., Dickel, T., Ayet San Andres, S., Bagchi, S., Beck, S., Geissel, H., Greiner, F., Haettner, E., Hornung, C., Kostyleva, D., Kuzminchuk, N., Kindler, B., Lommel, B., Martinez Pinedo, G., Miskun, I., Mukha, I., Piasetzky, E., Pietri, S., Plaß, W., Pomerantz, I., Prochazka, A., Purushotaman, S., Rappold, C., Saito, T., Scheidenberger, C., Tanaka, Y., Weick, H., and Winfield, J. (2018). A Novel Method for Measuring ß-Delayed Neutron Emission. *GSI Scientific Report*, 2018-1.

[Mendoza-Temis et al., 2015] Mendoza-Temis, J. d. J., Wu, M.-R., Langanke, K., Martínez-Pinedo, G., Bauswein, A., and Janka, H.-T. (2015). Nuclear robustness of the *r* process in neutron-star mergers. *Phys. Rev. C*, 92:055805.

[Metzger, 2017] Metzger, B. D. (2017). Kilonovae. *Living Reviews in Relativity*, 20(1):3.

[Metzger et al., 2010] Metzger, B. D., Martínez-Pinedo, G., Darbha, S., Quataert, E., Arcones, A., Kasen, D., Thomas, R., Nugent, P., Panov, I. V., and Zinner, N. T. (2010). Electromagnetic counterparts of compact object mergers powered by the radioactive decay of r-process nuclei. *Monthly Notices of the Royal Astronomical Society*, 406(4):2650–2662.

[Miskun et al., 2015] Miskun, I., Reiter, M. P., Rink, A., Dickel, T., Ayet, S., Ebert, J., Geissel, H., Greiner, F., Haettner, E., Hornung, C., Plaß, W., Purushothaman, S., and Scheidenberger, C. (2015). An RFQ based beam line and mass filter to improve identification capabilities at the diagnostics unit of the prototype CSC for the LEB. *GSI Scientific Report 2014*, 2015-1:146 p.

[Mumpower et al., 2016] Mumpower, M., Surman, R., McLaughlin, G., and Aprahamian, A. (2016). The impact of individual nuclear properties on r-process nucleosynthesis. *Progress in Particle and Nuclear Physics*, 86:86 – 126.

[Nicholl et al., 2017] Nicholl, M., Berger, E., Kasen, D., Metzger, B. D., Elias, J., Briceño, C., Alexander, K. D., Blanchard, P. K., Chornock, R., Cowperthwaite, P. S., Eftekhari, T., Fong, W., Margutti, R., Villar, V. A., Williams, P. K. G., Brown, W., Annis, J., Bahramian, A., Brout, D., Brown, D. A., Chen, H.-Y., Clemens, J. C., Dennihy, E., Dunlap, B., Holz, D. E., Marchesini, E., Massaro, F., Moskowitz, N., Pelisoli, I., Rest, A., Ricci, F., Sako, M., Soares-Santos, M., and Strader, J. (2017). The electromagnetic counterpart of the binary neutron star merger LIGO/Virgo GW170817. III. optical and UV spectra of a blue kilonova from fast polar ejecta. *The Astrophysical Journal Letters*, 848(2):L18.

[Orford et al., 2017] Orford, R., Clark, J. A., Nystrom, A., Savard, G., Aprahamian, A., Brodeur, M., Buchinger, F., Burdette, D., Burkey, M. T., Hirsh, T. Y., Kelly, J., Lascar, D., Ling-Ying, L., Morgan, G. E., Sharma, K. S., and Siegl, K. (2017). *Phase-imaging Mass Measurements with the Canadian Penning Trap Mass Spectrometer*.

[Pietri et al., 2018] Pietri, S., Bruce, A., Grahn, T., Plass, W., Scheidenberger, C., Dickel, T., Kelić-Heil, A., Geissel, H., Weick, H., Ameil, F., Arici, T., Audouin, L., Ayet, S., Aysto, J., Bagchi, S., Bai, M., Benlliure, S. B. J., Benzoni, G., Bruno, C., Cortina, D., Davisson, T., Gerl, J., Gorska, M., Greiner, F., Haettner, E., Hall,

O., Brennan, L. H., Heinz, A., Helert, A., Hornung, C., Hucka, J., Jokinen, A., Kankainen, A., Kahl, D., Kindler, B., Kojuharov, I., Kostyleva, D., Kuzminchuk, N., Labiche, M., Woods, C. L., Lomme, B., Pinedo, G. M., Miskun, I., Münzenberg, G., Mukha, I., Page, R., Pfutzner, M., Podolyak, Z., Prochazka, A., Purushotaman, S., Rappold, C., Regan, P., Ricciardi, M., Antila, S. R., Saha, S., Saito, T., Schaffner, H., Schirru, F., Simpson, J., Simon, H., Spiller, P., Stadlmann, J., Taieb, J., Tanaka, Y., Tanihata, I., Vesic, J., Voss, B., Walker, P., Woods, P., Winfield, J., and Winkler, M. (2018). Search for new neutron-rich isotopes and exploratory studies in the element range from Terbium to Rhenium. *GSI Scientific Report*, 2018-1.

[Plaß et al., 2018] Plaß, W., Dickel, T., Ayet San Andres, S., Bagchi, S., Balbanski, D., Beck, S., Constantin, P., Eronen, T., Geissel, H., Greiner, F., Haettner, E., Hornung, C., Jokinen, A., Kankainen, A., Kostyleva, D., Kuzminchuk, N., Kindler, B., Lommel, B., Mardor, I., Moore, I., Miskun, I., Mukha, I., Münzenberg, G., Patyk, Z., Piasetzky, E., Pietri, S., Pomerantz, I., Prochazka, A., Purushotaman, S., Rappold, C., Sami, R., Saito, T., Scheidenberger, C., Weick, H., Winfield, J., and Äystö, J. (2018). Detector tests with the prototype CSC for the Super-FRS and direct mass measurements of neutron-deficient nuclides below 100-Sn. *GSI Scientific Report*, 2018-1.

[Plaß et al., 2013a] Plaß, W., Dickel, T., Purushothaman, S., Dendooven, P., Geissel, H., Ebert, J., Haettner, E., Jesch, C., Ranjan, M., Reiter, M., Weick, H., Amjad, F., Ayet, S., Diwisch, M., Estrade, A., Farinon, F., Greiner, F., Kalantar-Nayestanaki, N., Knöbel, R., Kurcewicz, J., Lang, J., Moore, I., Mukha, I., Nociforo, C., Petrick, M., Pfützner, M., Pietri, S., Prochazka, A., Rink, A.-K., Rinta-Antila, S., Schäfer, D., Scheidenberger, C., Takechi, M., Tanaka, Y., Winfield, J., and Yavor, M. (2013a). The FRS Ion Catcher – A facility for high-precision experiments with stopped projectile and fission fragments. *Nuclear Instruments and Methods in Physics Research Section B: Beam Interactions with Materials and Atoms*, 317(Part B):457 – 462. XVIth International Conference on ElectroMagnetic Isotope Separators and Techniques Related to their Applications, December 2–7, 2012 at Matsue, Japan.

[Plaß, 1997] Plaß, W. R. (1997). Aufbau eines flugzeitmassenspektrometers zur analyse von flüchtigen organischen verbindungen bei geringem partialdruck. *Diplomarbeite - Justus-Liebig-Universität, Gießen*.

[Plaß et al., 2015] Plaß, W. R., Dickel, T., Ayet San Andres, S., Ebert, J., Greiner, F., Hornung, C., Jesch, C., Lang, J., Lippert, W., Majoros, T., Short, D., Geissel, H., Haettner, E., Reiter, M. P., Rink, A.-K., Scheidenberger, C., and Yavor, M. I. (2015). High-performance multiple-reflection time-of-flight mass spectrometers for

research with exotic nuclei and for analytical mass spectrometry. *Physica Scripta*, 2015(T166):014069.

[Plaß et al., 2008] Plaß, W. R., Dickel, T., Czok, U., Geissel, H., Petrick, M., Reinheimer, K., Scheidenberger, C., and I.Yavor, M. (2008). Isobar separation by time-of-flight mass spectrometry for low-energy radioactive ion beam facilities. *Nuclear Instruments and Methods in Physics Research Section B: Beam Interactions with Materials and Atoms*, 266(19):4560 – 4564. Proceedings of the XVth International Conference on Electromagnetic Isotope Separators and Techniques Related to their Applications.

[Plaß et al., 2013b] Plaß, W. R., Dickel, T., and Scheidenberger, C. (2013b). Multiple-reflection time-of-flight mass spectrometry. *International Journal of Mass Spectrometry*, 349-350:134 – 144. 100 years of Mass Spectrometry.

[Purushothaman et al., 2017] Purushothaman, S., Ayet San Andrés, S., Bergmann, J., Dickel, T., Ebert, J., Geissel, H., Hornung, C., Plaß, W., Rappold, C., Scheidenberger, C., Tanaka, Y., and Yavor, M. (2017). Hyper-emg: A new probability distribution function composed of exponentially modified gaussian distributions to analyze asymmetric peak shapes in high-resolution time-of-flight mass spectrometry. *International Journal of Mass Spectrometry*, 421(Supplement C):245 – 254.

[R Core Team, 2017] R Core Team (2017). *R: A Language and Environment for Statistical Computing*. R Foundation for Statistical Computing, Vienna, Austria.

[Raeder et al., 2014] Raeder, S., Heggen, H., Lassen, J., Ames, F., Bishop, D., Bricault, P., Kunz, P., Mjøs, A., and Teigelhöfer, A. (2014). An ion guide laser ion source for isobar-suppressed rare isotope beams. *Review of Scientific Instruments*, 85:033309.

[Ranjan et al., 2015] Ranjan, M., Dendooven, P., Purushothaman, S., Dickel, T., Reiter, M., Ayet, S., Haettner, E., Moore, I., Kalantar-Nayestanaki, N., Geissel, H., Plaß, W., Schäfer, D., Scheidenberger, C., Schreuder, F., Timersma, H., de Walle, J. V., and Weick, H. (2015). Design, construction and cooling system performance of a prototype cryogenic stopping cell for the Super-FRS at FAIR. *Nuclear Instruments and Methods in Physics Research Section A: Accelerators, Spectrometers, Detectors and Associated Equipment*, 770(Supplement C):87 – 97.

[Ranjan et al., 2011] Ranjan, M., Purushotaman, S., Geissel, H., Plaß, W., Schaefer, D., Scheidenberger, C., Van De Walle, J., Weick, H., and Dendooven, P. (2011). New stopping cell capabilities: RF carpet performance at high gas density and cryogenic operation. *Europhysics Letter*, 96(5):52001.

[Reiter, 2015] Reiter, M. P. (2015). *Pilot experiments with relativistic uranium projectile and fission fragments thermalized in a cryogenic gas-filled stopping cell*. PhD thesis, Justus-Liebig-Universität.

[Reiter, 2018] Reiter, M. P. (2018). Private comunication.

[Reiter et al., 2018] Reiter, M. P., Sieverding, A., Ayet San Andrés, S., Nikas, S., Dickel, T., Plaß, W. R., Martínez-Pinedo, G., and Scheidenberger, C. (2018). Mass measurements of neutron-rich gallium isotopes towards the weak r-process path. *Manuscript pending submission*.

[Rink, 2017] Rink, A.-K. (2017). *Mass and life-time measurement of the 1.7ms 215-Po isotope : a crucial test of the novel concept of the cryogenic ion catcher for the Super-FRS at GSI-FAIR*. PhD thesis, Justus-Liebig-Universität.

[Scheidenberger et al., 2001] Scheidenberger, C., Attallah, F., Casares, A., Czok, U., Dodonov, A., Eliseev, S. A., Geissel, H., Hausmann, M., Kholomeev, A., Kozlovski, V., Litvinov, Y. A., Maier, M., Münzenberg, G., Nankov, N., Novikov, Y. N., Radon, T., Stadlmann, J., Weick, H., Weidenmüller, M., Wollnik, H., and Zhou, Z. (2001). A new concept for time-of-flight mass spectrometry with slowed-down short-lived isotopes. pages 531–534.

[Schäfer, 2010] Schäfer, D. (2010). *Design and simulation of a cryogenic stopping cell for the lowenergy branch of the Super-FRS at FAIR*. PhD thesis, Justus-Liebig-Universität.

[Schlitt et al., 1997] Schlitt, B., Beckert, K., Bosch, F., Eickhoff, H., Franzke, B., Fujita, Y., Geissel, H., Hausmann, M., Irnich, H., Klepper, O., Kluge, H.-J., Kozhuharov, C., Kraus, G., Münzenberg, G., Nickel, F., Nolden, F., Patyk, Z., Radon, T., Reich, H., Scheidenberger, C., Schwab, W., Steck, M., Sümmerer, K., Winkler, T., Beha, T., Falch, M., Kerscher, T., Löbner, K., Jung, H., Wollnik, H., and Novikov, Y. (1997). Schottky mass spectrometry at the esr: a novel tool for precise direct mass measurements of exotic nuclei. *Nuclear Physics A*, 626(1):315 – 325. Proceedings of the Third International Conference on Nuclear Physics at Storage Rings.

[Sieverding and Nikas, 2018] Sieverding, A. and Nikas, S. (2018). Private comunication.

[Smorra et al., 2015] Smorra, C., Blaum, K., Bojtar, L., Borchert, M., Franke, K., Higuchi, T., Leefer, N., Nagahama, H., Matsuda, Y., Mooser, A., Niemann, M., Ospelkaus, C., Quint, W., Schneider, G., Sellner, S., Tanaka, T., Van Gorp, S., Walz, J., Yamazaki, Y., and Ulmer, S. (2015). Base – the baryon antibaryon symmetry experiment. *The European Physical Journal Special Topics*, 224(16):3055–3108.

[Stock, 2013] Stock, R. (2013). *Encyclopedia of Nuclear Physics and its Applications*. Wiley-VCH.

[Thomson, 1913] Thomson, J. J. (1913). Bakerian lecture: Rays of positive electricity. *Proceedings of the Royal Society of London A: Mathematical, Physical and Engineering Sciences*, 89(607):1–20.

[Van Schelt et al., 2013] Van Schelt, J., Lascar, D., Savard, G., Clark, J. A., Bertone, P. F., Caldwell, S., Chaudhuri, A., Levand, A. F., Li, G., Morgan, G. E., Orford, R., Segel, R. E., Sharma, K. S., and Sternberg, M. G. (2013). First results from the caribu facility: Mass measurements on the r-process path. *Phys.Rev.Lett.*, 111:061102.

[Wapstra et al., 2003] Wapstra, A., Audi, G., and Thibault, C. (2003). The AME2003 atomic mass evaluation: (I). Evaluation of input data, adjustment procedures. *Nuclear Physics A*, 729(1):129 – 336. The 2003 NUBASE and Atomic Mass Evaluations.

[Wasserburg et al., 1996] Wasserburg, G. J., Busso, M., and Gallino, R. (1996). Abundances of actinides and short-lived nonactinides in the interstellar medium: Diverse supernova sources for the r-processes. *The Astrophysical Journal Letters*, 466(2):L109.

[Weick et al., 2000] Weick, H., Geissel, H., Scheidenberger, C., Attallah, F., Baumann, T., Cortina, D., Hausmann, M., Lommel, B., Münzenberg, G., Nankov, N., Nickel, F., Radon, T., Schatz, H., Schmidt, K., Stadlmann, J., Sümmerer, K., Winkler, M., and Wollnik, H. (2000). Slowing down of relativistic few-electron heavy ions. *Nuclear Instruments and Methods in Physics Research Section B: Beam Interactions with Materials and Atoms*, 164-165(Supplement C):168 – 179.

[Weizsäcker, 1935] Weizsäcker, C. F. v. (1935). Zur theorie der kernmassen. *Zeitschrift für Physik*, 96(7):431–458.

[Wien, 1902] Wien, W. (1902). Untersuchungen über die elektrische entladung in verdünnten gasen. *Annalen der Physik*, 313(6):244–266.

[Wikipedia, 2018a] Wikipedia (2018a). Wikipedia median article. *https://en.wikipedia.org/wiki/Median*.

[Wikipedia, 2018b] Wikipedia (2018b). Wikipedia reflectron article. *https://en.wikipedia.org/wiki/Reflectron*.

[Wiley and McLaren, 1955] Wiley, W. C. and McLaren, I. H. (1955). Time-of-flight mass spectrometer with improved resolution. *Review of Scientific Instruments*, 26(12):1150–1157.

[Will, 2017] Will, C. (2017). *TITAN's Multiple-Reflection Time-of-Flight Mass Spectrometer and Isobar Separator Characterization and First Experiments*. PhD thesis.

[Wolf et al., 2012] Wolf, R. N., Marx, G., Rosenbusch, M., and Schweikhard, L. (2012). Static-mirror ion capture and time focusing for electrostatic ion-beam traps and multi-reflection time-of-flight mass analyzers by use of an in-trap potential lift. *International Journal of Mass Spectrometry*, 313:8 – 14.

[Wollersheim, 2018] Wollersheim, H.-J. (2018). Personal web gsi. *https://web-docs.gsi.de/wolle*.

[Wollnik and Przewloka, 1990] Wollnik, H. and Przewloka, M. (1990). Time-of-flight mass spectrometers with multiply reflected ion trajectories. *International Journal of Mass Spectrometry and Ion Processes*, 96(3):267 – 274.